The Origin of Charged Lepton Mass with the ATLAS Experiment

Laurence Spiller

Supervised by

Prof. Elisabetta Barberio

Submitted in total fullfilment of the degree of the

Doctor of Philosophy

School of Physics

University of Melbourne
January 17, 2018

ORCID: 0000-0002-5650-7586

Produced on archival quality paper

Declaration

This is to certify that

1. This thesis comprises only my original work towards the PhD except where indicated in the introduction,
2. Due acknowledgement has been made in the text to all other material used,
3. The thesis is less than 100,000 words in length, exclusive of tables, bibliographies and appendices.

Laurence Spiller

Acknowledgements

Firstly I'd like to thank my supervisor Elisabetta Barberio without whom I, almost certainly, would have not been able to finish this thesis. I suspect most supervisors would have given up on me. I would also like to thank those with whom I have worked. Namely: Daniele, Gui, Noel and Rustem. I am also grateful to Sean Crosby for his invaluable assistance.

To my fellow students and office mates for the engaging and interesting atmosphere over the past few years including Josh, Tomasz, Pere, Isaac, David, KG, Marco, Brian, Steven, Eisha, John, Chia-Lin, Leon, Rebecca and many more!

No acknowledgements section would be complete without finally thanking my parents and close family, namely Luisa, Philip and George. It goes without saying, that I owe much of what I am to them.

Abstract

Using high energy proton-proton collisions from the Large Hadron Collider (LHC), the ATLAS experiment is able to probe the decays of the recently discovered Higgs boson. Despite large and complex backgrounds, a significant excess corresponding to the decay of the Higgs boson to charged leptons was observed with the first 25 fb^{-1} of data at a collision energy of 7-8 TeV. The LHC has now entered its second phase having collected 13.2 fb^{-1} of data at a collision energy of 13 TeV with the intention to accumulate approximately 3000 fb^{-1} of data over its operating life. This dataset, or even a fraction thereof, will allow the ATLAS experiment to test the veracity of the Higgs theory of charged lepton mass and to perform precision measurement into the nature of Electroweak symmetry breaking in the Standard Model. A preliminary measurement is presented containing the two most effective decays for probing the origin of charged lepton mass in the Standard Model: H$\rightarrow \tau\tau$ and H$\rightarrow \mu\mu$. Preliminary limits are placed on the Higgs–muon coupling at seven times the Standard Model value and a 2σ excess of the di-tau events is observed which is consistent with the Standard Model.

Contents

List of Figures

List of Tables

Chapter 1

Introduction

The current generation of collider experiments have reached energies and luminosities that allow for the production and study of the Higgs boson. This new phase of particle physics began with the joint discovery of the Higgs boson by the ATLAS[1] and CMS[2] experiments. The mass of this new particle has been measured to be 125.09 ± 0.21 (stat) ± 0.11 (syst) GeV[3]. In the context of the Standard Model (SM) of Particle Physics, this mass occurs at the value where a large subset of the Higgs boson's couplings can be directly measured.

The discovery of the Higgs boson occurred through the observation of its decays into di-bosons, namely photons and the W and Z boson. The focus of this thesis is the measurements of the couplings of the Higgs boson to the charged leptons. These couplings, although less experimentally accessible, provide a direct probe of the origin of lepton mass as well as precision tests of lepton universality and flavour physics. This thesis presents the Higgs–lepton coupling measurements performed using data collected by the ATLAS detector. This measurement is performed using Higgs boson decays to $H \to \tau\tau$ and $H \to \mu\mu$.

The structure of this thesis is as follows. Chapter 2 provides an original overview of the Standard Model of Particle Physics. A brief and original overview of the ATLAS experiment is provided in Chapter 3. Chapter 4 describes the reconstruction of muons within the ATLAS experiment. Chapter 5 describes tau lepton reconstruction within ATLAS. The subsection on tau identification and performance was performed by this author in collaboration with Guilherme Hanninger and formed part of the body of work required for the author to qualify as a full member of the ATLAS collaboration. The subsection on the L1Topo trigger commissioning described in 5.3.1 is also based on work performed by this author in collaraboation with Daniele Zanzi. Chapter 6 is based on a

paper by this author regarding a novel technique for extracting topological information from hadron collisions. This technique is then applied in Chapter 7 which describes the measurement of the Higgs–tau coupling which is a continuation of the work begun in Reference [4]. This measurement was performed by this author but utilises the work of many people within the ATLAS collaboration. Finally, Chapter 8 provides the current limits and prospects for a similar measurement of the Higgs–muon coupling. This chapter is based on work done by the ATLAS collaboration to which this author contributed to the statistical process of fitting and limit setting.

Chapter 2

The Standard Model of Particle Physics

The Standard Model with neutrino masses provides a seemingly complete description of all observed phenomena in high energy physics. As yet, collider experiments have uncovered no unambiguous evidence of new structure despite being able to probe energies at the TeV scale. The weight of experimental evidence suggests that the Standard Model seems to provide a complete description of the behaviour of elementary particles at the Electroweak scale. Furthermore, the proof that the Standard Model is renormalisable implies that this behaviour can be extended to arbritrarily high energies[5]. The only unambiguously necessary extension is that of Gravity which, at present, cannot be incorporated in the gauge structure of the Standard Model in a straightforward manner. The energy at which Gravity is thought to meaningfully affect collider experiments, estimated to be the Reduced Planck Scale, is many orders of magnitude greater than the current generation of colliders.

What follows is a brief overview of the relevant theoretical and experimental topics in the Standard Model. The notation and conventions for the theoretical topics are the same as those used in Martin[6] and Cheng and Li[7].

2.1 Gauge Theory of Particle Interactions

Gauge Theories arise from the need to create quantum field theories which are both renormalisable and obey unitarity. The motivation for gauge theories is also supported by their link with geometry in the study of fibre bundles and the concept of 'parallel

transport' in an abstract space described by curvature tensor, $F_{\mu\nu}$. Note that this (and all equations in this section) exclude the terms which are Hermitian conjugate to the terms shown.

A field theory which is locally gauge invariant for a given group, G, must be invariant under the following gauge transformation:

$$\psi \rightarrow \mathrm{e}^{-\left(\frac{\mathrm{i}}{2}\boldsymbol{\tau}\cdot\boldsymbol{\theta}(\boldsymbol{x})\right)}\psi, \tag{2.1}$$

where $\boldsymbol{\tau}$ form a representation of the group G, and $\boldsymbol{\theta}$ are the set of transformation parameters. The requirement that this be local allows $\boldsymbol{\theta}$ to be space-time dependent. To construct this gauge invariant theory, a new vector field, $\mathrm{A}_{\boldsymbol{\mu}}$, is incorporated which allows for the construction of a gauge-covariant derivative:

$$\mathrm{D}_\mu\psi = \left(\partial_\mu - \frac{ig}{2}\boldsymbol{\tau}\cdot\mathrm{A}_\mu\right) \tag{2.2}$$

where g is the coupling strength or quantum number of the field, ψ. It can be shown that this new vector field, $\mathrm{A}_{\boldsymbol{\mu}}$, transforms under the gauge transformation as:

$$A^i_\mu \rightarrow A^i_\mu + \mathrm{T}^{ijk}\theta^j A^k_\mu - \frac{1}{\mathrm{g}}\delta_\mu\theta^i, \tag{2.3}$$

which corresponds to the adjoint representation of the above gauge group. This can then be used to construct dynamic terms for fermions (ψ), scalar bosons (ϕ) and vector bosons (A) of the form:

$$\overline{\psi}\gamma^\mu\mathrm{D}_\mu\psi, \quad \mathrm{D}^\mu\overline{\phi}\mathrm{D}_\mu\phi, \quad \mathrm{F}^i_{\mu\nu}\mathrm{F}^{i\mu\nu}, \tag{2.4}$$

where

$$\mathrm{F}^i_{\mu\nu} = \delta_\mu\mathrm{A}^i_\nu - \delta_\nu\mathrm{A}^i_\mu + g\mathrm{T}^{ijk}A^j_\mu A^k_\nu, \tag{2.5}$$

and γ^μ refers to the Clifford Algebra. The Lagrangian for a locally gauge invariant field can then be written as:

$$\mathscr{L} = \Sigma_i\overline{\psi_i}\gamma^\mu\mathrm{D}_\mu\psi_i \ + \Sigma_j\mathrm{D}_\mu\overline{\phi}_j\mathrm{D}^\mu\phi_j \ + \frac{1}{2}\Sigma_k\mathrm{F}^{\mu\nu}\mathrm{F}_{\mu\nu} \ + \mathrm{f}\left(\overline{\psi},\psi,\overline{\phi},\phi\right) \tag{2.6}$$

where f is any locally gauge invariant, renormalisable function of the chiral fields.

2.1.1 Electroweak Symmetry Breaking

The above description of a locally invariant gauge theory has the property that for any non-abelian group the mass terms of the form $\mathrm{m}\overline{\psi}\psi$ or $\mathrm{m}^2\mathrm{A}_\mu\mathrm{A}^\mu$ are not locally gauge invariant nor are they renormalisable. The observations of self-interactions within gauge fields (such as that between gluons) and of massive fermion and vector bosons require any realistic Lagrangian to contain non-abelian gauge bosons as well as massive fermions and gauge bosons. The method in which these are introduced into the Lagrangian is called spontaneous symmetry breaking (SSB).

SSB can be achieved by introducing a new scalar boson with both a mass and quartic interaction:

$$\mathscr{L}_{\mathrm{new}} = \mathrm{D}_\mu\overline{\phi}\mathrm{D}^\mu\phi + m^2\overline{\phi}\phi + \lambda\left|\phi\right|^4. \tag{2.7}$$

This forms a valid, gauge invariant addition to the Lagrangian. The SSB is induced becase the vacuum expectation value (VEV) of this field will not occur at $<\phi>=0$ but will occur at

$$<\phi>=\sqrt{\frac{m^2}{\lambda}}=\frac{1}{\sqrt{2}}v. \tag{2.8}$$

The effect of this change to the vacuum state is made manifest by the replacement of ϕ by $\phi-<\phi>$. In this form, the gauge bosons which couple to this field acquire mass through the dynamic terms for ϕ. The mass terms generated for the gauge bosons is equal to the VEV multiplied by the coupling strength and charge of this scalar boson to the gauge field, $\frac{vg}{2}$.

This field can also induce a mass in the fermions through the addition of interaction terms to the Lagrangian of the form:

$$\mathscr{L}_{\mathrm{int}} = \mathrm{Y}_{ij}\overline{\psi}_i\phi\psi_j \tag{2.9}$$

where Y is the coupling strength. Terms of this form are referred to as Yukawa couplings. By a similar transformation of $\phi\rightarrow\phi-<\phi>$ as above, mass terms are generated with fermion mass: $\mathrm{Y}_{ii}v$.

The VEV specified above may not be a single value but can take any value satisfying $\left|<\overline{\phi}\phi>\right|=\frac{v^2}{2}$. These degrees of freedom cause the formation of one or more massless

bosons, referred to as the Nambu-Goldstone Bosons. This is in addition to the standard massive boson.

2.2 Structure of the Standard Model

The Standard Model of Particle Physics consists of two families of fermions each with three generations, the leptons and quarks. These form the main consistuents of matter. The interactions between these particles are described by the gauge group:

$$\mathrm{SU}(3)_c \times \mathrm{SU}(2)_L \times \mathrm{U}(1)_Y \,. \tag{2.10}$$

The three groups correspond to Colour charge, Isospin, and Hypercharge. The colour force describes Quantum Chromodynamics (QCD) and is mediated by the gluons. Only the quarks and gluons carry colour charge. The Isospin and Hypercharge describe the Electroweak force. The Isospin, which is responsible for parity violation, is carried by the W boson while Hypercharge is carried by the B. The Lagrangian describing the SM can be written as:

$$\begin{aligned}
\mathscr{L}_{\mathrm{SM}} = & -\frac{1}{4}\left(B_{\mu\nu}B^{\mu\nu} + \Sigma_{a=1}^{3} W_a^{\mu\nu} W_{\mu\nu}^a + \Sigma_{b=1}^{8} G_b^{\mu\nu} G_{\mu\nu}^b\right) \\
& + i\overline{L}_L^i \gamma^\mu D_\mu L_L^i + i\overline{e}_R^i \gamma^\mu D_\mu e_R^i \\
& + i\overline{Q}_L^i \gamma^\mu D_\mu Q_L^i + i\overline{d}_R^i \gamma^\mu D_\mu d_R^i + i\overline{u}_R^i \gamma^\mu D_\mu u_R^i \\
& + \left(D_\mu \Phi\right)^\dagger D^\mu \Phi - m_H^2 \Phi^\dagger \Phi - \lambda\left(\phi^\dagger \phi\right)^2 \\
& + \left(\lambda_1^{ij} \overline{L}_L^i \Phi e_R^j + \lambda_2^{ij} \overline{q}_L^i \Phi d_R^j + \lambda_3^{ij} \overline{Q}_L^i \Phi u_R^j\right).
\end{aligned} \tag{2.11}$$

The left handed component of the leptons and quarks of generation i are included in the Isospin doublet L^i and Q^i respectively while the associated right handed components (if present) are contained in e, u and d for the charged leptons as well as the up and down quarks of each generation. Note that no see-saw mechanism or right handed neutrino is included in this formulation of the Standard Model for historical reasons despite the observation of neutrino oscillations. This ommision produces no observable effects at the Large Hadron Collider (LHC). The quantum numbers of these particles under each group is shown in Table 2.1. The Higgs field, Φ, in particular transforms as a doublet under

Names		Symbols	$SU(3)_C$, $SU(2)_L$, $U(1)_Y$	$U(1)_{\text{QCD}}$
quarks	Q	$(u_L \;\; d_L)$	$(\mathbf{3}, \mathbf{2}, \frac{1}{6})$	$(\frac{2}{3}, -\frac{1}{3})$
($\times$3 families)	$\bar{u}$	$u_R^\dagger$	$(\overline{\mathbf{3}}, \mathbf{1}, -\frac{2}{3})$	$-\frac{2}{3}$
	$\bar{d}$	$d_R^\dagger$	$(\overline{\mathbf{3}}, \mathbf{1}, \frac{1}{3})$	$\frac{1}{3}$
leptons	L	$(\nu \;\; e_L)$	$(\mathbf{1}, \mathbf{2}, -\frac{1}{2})$	$(0, 1)$
($\times$3 families)	$\bar{e}$	$e_R^\dagger$	$(\mathbf{1}, \mathbf{1}, 1)$	-1
Higgs	H	$(H^+ \;\; H^0)$	$(\mathbf{1}, \mathbf{2}, \frac{1}{2})$	$(1, 0)$

Table 2.1: Chiral multiplets of the Standard Model consist of spin $\frac{1}{2}$ fermions that can be divided into three generations of leptons and quarks and a spin-0 complex Higgs doublet.

Name	Symbol	$SU(3)_C$, $SU(2)_L$, $U(1)_Y$
gluon	g	$(\mathbf{8}^*, \mathbf{1}, \mathbf{0})$
W boson	$W_{1,2,3}$	$(\mathbf{1}, \mathbf{3}^*, \mathbf{0})$
B boson	B^0	$(\mathbf{1}, \mathbf{1}, \mathbf{0})$

Table 2.2: The gauge bosons of the Standard model before spontaneous symmetry breaking. Each of these has spin 1.

Name	Symbol	$SU(3)_C$, $U(1)_{\text{QED}}$
gluon	g	$(\mathbf{8}^*, \mathbf{0})$
W boson	$W^\pm$	$(\mathbf{1}, \pm\mathbf{1})$
Z boson	Z^0	$(\mathbf{1}, \mathbf{0})$
Photon	γ	$(\mathbf{1}, \mathbf{0})$

Table 2.3: The gauge bosons of the Standard Model when in the vacuum state. The W and Z boson arise as a result of spontaneous symmetry breaking from the Higgs sector.

$SU(2)_L$ and is used to generate a VEV which induces the symmetry breaking:

$$\mathrm{SU}(2)_L \times \mathrm{U}(1)_Y \rightarrow \mathrm{U}(1)_{\mathrm{EM}}\,, \tag{2.12}$$

where the new gauge group is Electromagnetism. Like the general gauge theory in the previous section, a mass is induced for the fermions of the form $\lambda^{ii}v$. The effect of symmetry breaking is also to make the gauge eigenstate (shown above) differ from the mass eigenstate. In the Standard Model, switching to the mass eigenstate results in these massless bosons being absorbed by the gauge bosons associated with each force, W for $\mathrm{SU}(2)_{\mathrm{L}}$ and B for $\mathrm{U}(1)_{\mathrm{Y}}$. In the Standard Model, the would-be Nambu-Goldstone bosons form the longitudinal polarisations of the W and Z bosons[8, 9]. The mass eigenstates of the gauge bosons are as follows:

$$\begin{aligned} m_{W^\pm} &= \frac{1}{2}v\,|g| & W^\pm &= \frac{1}{\sqrt{2}}\left(W_1 \mp iW_2\right) \\ m_Z &= \frac{1}{2}v\sqrt{g^2+g'^2} & Z^0 &= \cos\theta_W W_3 - \sin\theta_W B \\ m_A &= 0 & A^0 &= \sin\theta_W W_3 + \cos\theta_W B \end{aligned} \tag{2.13}$$

Remaining is a single real scalar field refered to as the Higgs boson. This particle, couples to particles in proportion to the particles mass and provides a direct probe, through its Yukawa couplings, of the origin of lepton mass. The Standard Model, as described, is summarised in Table 2.1, 2.2 and 2.3.

In this form, excluding the source of neutrino masses and neutrino mixing, the SM is described by eighteen free parameters which can only be determined experimentally. These are the nine masses of the fermions, four parameters describing mixing between quarks due to differing mass and electroweak eigenstate (leptons are assumed not to have any mixing between states), the coupling strength of each of the three forces, and the two parameters (mass and vacuum expectation value) describing the Higgs boson's potential.

2.3 Phenomenology of the Higgs Boson

2.3.1 Production Modes

The Higgs boson can be produced by several mechanisms at a proton-proton collider. The main processes are gluon-gluon fusion (ggF), vector boson fusion (VBF), production in association with top quarks (ttH) and production by Higgs-strahlung of a vector boson (VH)[10–12]. These processes are summarised in Table 2.4 and their relative cross-sections in Figure 2.1. Of these processes, ggF has the highest production cross-section but VBF is typically the most sensitive due to its more distinctive topology. The distinctiveness of VBF occurs because the Higgs boson is produced in association with two additional jets which typically have a high rapidity and are flavour and colour independent. The VBF and ggF channels are also complimentary because VBF is sensitive to the Higgs-Boson coupling through the W/Z-Higgs interaction and ggF is sensitive to the Yukawa couplings through the fermion loop. This loop is dominated by the contribution of the top quark which limits its sensitivity to the lighter quarks and leptons.

The cross-sections of these production modes are calculated using the distributions of quark and gluon momentum fractions within the proton. The relevant quark and gluon initiated processes are calculated perturbatively to produce a final cross-section. The most extensive of these calculations has been done for ggF. The ggF process is dominated by slowly converging QCD corrections by comparison with the faster converging VBF which is predominately electroweak. The theoretical uncertainties are thus greater for ggF compared to VBF, 16% compared to $< 1\%$[13]. This also mean that ggF can get large contributions from next-to-leading order (NLO) Feynman diagrams. In particular, ggF with one additional jet is produced with approximately 80% of the cross-section of the leading order process. This is significant because the ggF+jet topology, consisting of a boosted Higgs boson with a recoiling jet, provides a more distinctive collider signature.

2.3.2 Decay Topologies

Once produced, the Higgs boson will decay within the beam pipe of the accelerator and can only be identified by its decay products. The decays of the Higgs boson which are of

experimental interest are $H \to WW$, $H \to ZZ$, $H \to \gamma\gamma$, $H \to \tau\tau$, $H \to bb$ and $H \to \mu\mu$. The relative importance of these channels depends on the mass of the Higgs boson. The relative branching fractions of the Higgs boson as a function of mass are shown in Figure 2.2.

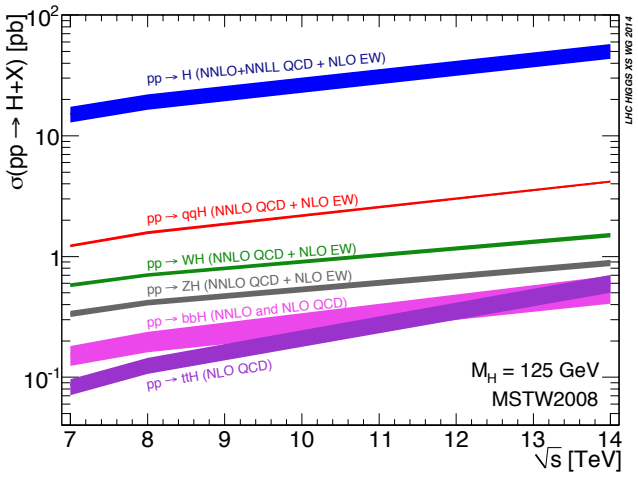

Figure 2.1: This figure provides the cross-section for each major Higgs boson production process at the LHC as a function of the centre-of-mass energy of the proton collisions. The shaded region indicates the one sigma error band about the nominal value[14].

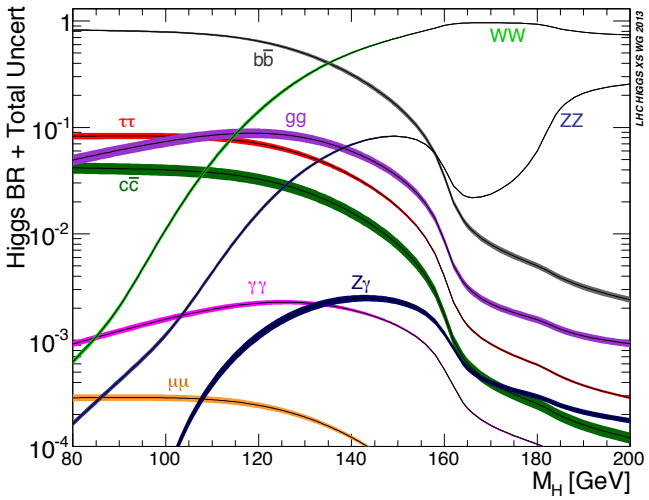

Figure 2.2: This figure provides the branching fraction of the Higgs boson as a function of its mass. All Higgs boson couplings are assumed to be Standard Model. The width of the lines indicates the one sigma error band about the nominal[14].

Process	Leading Order Diagrams
Gluon-Gluon Fusion (ggF)	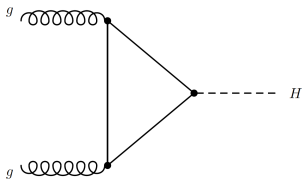
Vector Boson Fusion (VBF)	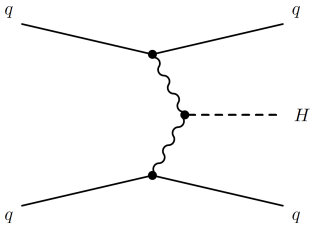
Higgs Production in Association with Vector Boson (VH)	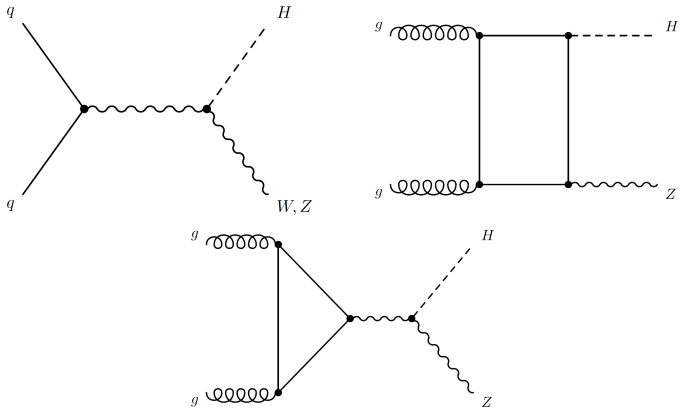
Higgs Production in Association with Top Quarks	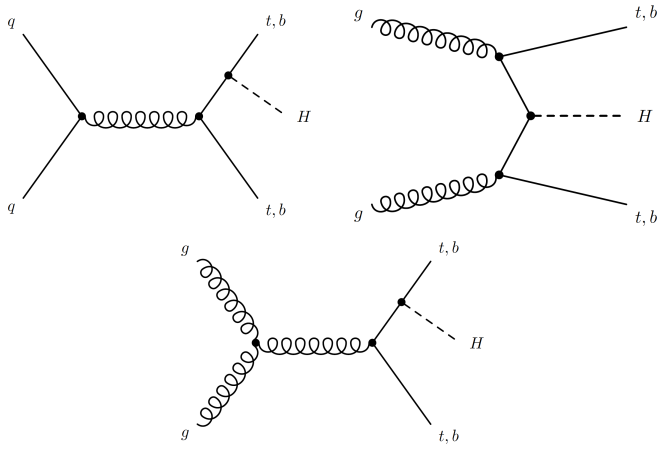

Table 2.4: The Higgs boson is produced primarily by ggF, VBF, VH and ttH (in order of decreasing cross-section) at the LHC. The leading order Feynman diagrams for each of these processes are shown.

2.4 Theoretical Limits and Experimental Measurements

2.4.1 Theoretical Considerations

As a free parameter in the Standard Model, the Higgs boson mass has few restrictions. It does however provide a fairly stringent upper and lower limit on the Higgs boson mass if the Standard Model is assumed to be complete within a given energy range. Both these limits rely on the VEV being at the currently accepted value of 246 GeV[15], derived from measurements of the W, Z mass and the gauge coupling strength of the SM.

The upper bound arises primarily from considerations of W-W scattering[16]. The presence of a Higgs boson mass above the TeV scale would require additional structure to prevent this process violating unitarity. More stringent, albeit less direct, constraints can also be generated by a careful examination of the high-energy behaviour of the Higgs quartic coupling. The Higgs quartic coupling, at high energy gives rise to a Landau pole at the one loop level. A Landau pole is considered unphysical so the scale at which it appears can be considered the scale at which the Standard Model is no longer valid. Requirements that the Standard Model is valid to the Planck Scale place an upper limit on the Higgs boson mass of 180 GeV. Even if the Standard Model is permitted to break down at energies around 5 TeV, an upper limit on the Higgs boson mass of approximately 400 GeV is attained.

A lower limit on the Higgs boson mass can be derived from considerations of vacuum stability. The vacuum of the Standard Model is required to be either stable or metastable (decay time longer than the age of the Universe) for straightforward reasons. The vacuum in the Standard Model is driven primarily by contributions to runnings of the Higgs quartic and mass terms from the top quark. This contributions is also sensitive to the cut-off scale below which the Standard Model is considered valid. Even for very low cut-off scales, a Higgs boson mass greater than 10 GeV occurs[17–19]. These constraints are summarised in Figure 2.3a.

2.4.2 Experimental Considerations

Direct searches for the Higgs boson have been performed by both LEP (Large Electron Positron collider) and the Tevatron (a proton-antiproton collider) prior to the particles discovery at the LHC[2, 20]. The mass region below 114 GeV was excluded at 95% confidence by LEP[21]. Tevatron was able to exclude the mass region between 149 GeV and 182 GeV and were able to reaffirm the limits established by LEP below 109 GeV[22] at greater than 95% confidence. These constraints are shown in Figure 2.3b. Although unable to form an observation of the Higgs boson, LEP was able to provide a tantalising clue through its precise measurements of the Z and W mass. These masses were found to be consistent with a Veltman parameter, ρ, of one[15]:

$$\rho = \frac{m_W^2}{m_Z^2 \cos(\theta_W)^2} = 1, \tag{2.14}$$

as predicted by the Standard Model with a Higgs doublet, although this property is also shared by other models.

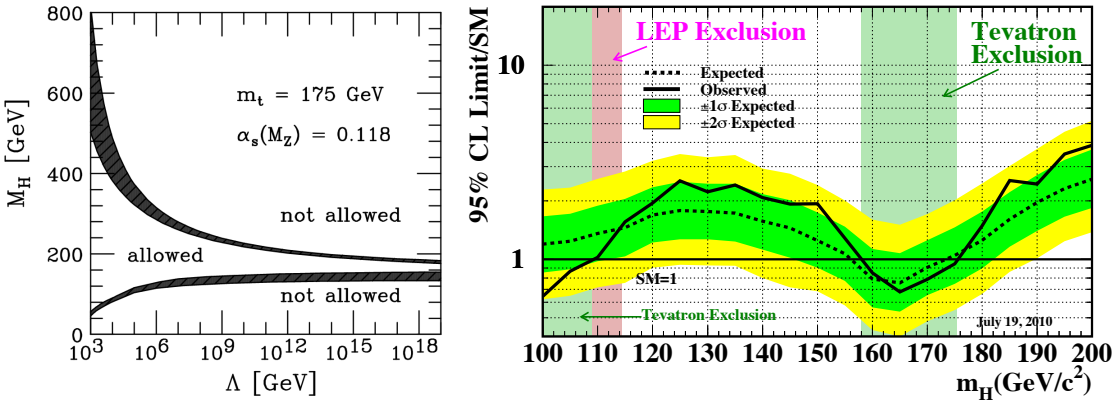

Figure 2.3: (a) The limits on the Higgs boson mass from theoretical constraints as a function of the cut-off scale at which the Standard Model is no longer deemed accurate. The allowed and disallowed regions are shown with the shaded region showing the uncertainties on these bounds. The upper limit on mass is primarily from WW scattering and the lower limit is derived from considerations of vacuum stability.[16]. (b) Limits on Standard Model Higgs boson from searches at the Tevatron experiments[22]. The 95% confidence limits are shaded for a Standard Model coupling strength. The limits are shown as a function of the Higgs boson masses and coupling strength relative to the Standard Model. The limits from LEP are also overlayed.

2.4.3 Discovery of the Higgs Boson

The CMS[23, 24] and ATLAS[25, 26] experiments were built to be able to probe the full range of possible Higgs boson masses from 100 GeV to 1 TeV. The Higgs boson was subsequently discovered at the LHC by both the CMS and ATLAS experiments with a significance of 4.9 and 5.0σ and announced at the 2012 ICHEP conference. The discovery of the Higgs boson occured primarily in the the $H \to ZZ^* \to 4l$, $H \to WW^* \to 2l2\nu$ and $H \to \gamma\gamma$ channels utilizing the ggF and VBF production modes. The discovery was performed using 7 and 8 TeV centre-of-mass proton-proton collisions with $4.8 - 5.1$ and $5.3 - 5.8\text{fb}^{-1}$ of data.

2.4.4 Current Status of Higgs Boson Measurements

The addition of more data (for a total of 25 fb^{-1}) has allowed additional measurements to be performed and others to be further refined. The current best estimate of the Higgs boson mass is 125.09 $\pm$ 0.21 (stat.) $\pm$ 0.11 (syst.) GeV, from the combined measurement of ATLAS and CMS[27]. This value for the Higgs boson mass occurs in a unique region of parameter space. It has been observed that at a mass of 125 GeV, the product of its branching ratios, $\Pi_i \text{Br}\,(H \to p_i p_i)$, is maximised. Whether this value is of theoretical significance is a matter of speculation. The experimental implication of this are less ambiguous, allowing for the widest possible set of measurements of Higgs boson couplings by the ATLAS and CMS experiments. These sets of measurements are shown in Figure 2.4 and 2.5. The properties of the Higgs boson's spin and parity have also been measured. The existance of a di-photon decay restricts the Higgs boson to be of spin 0 or spin 2 by the Landau-Yan Theorem. Distinguishing between the remaining possibilities for spin and parity was performed by measuring the angular distribution of the decay products. Using this method for the di-boson decays of the Higgs boson, the 0^-, $1^\pm$ and graviton-like 2^+ were excluded at over 99.9% confidence with the remaining hypothesis, 0^+, being favoured[28]. This is consistent with the predictions of the Standard Model for a 0^+ Higgs boson.

The Higgs boson's decay width is an important measurement that can be performed in the future. The current best estimate of the decay width of the Higgs boson has

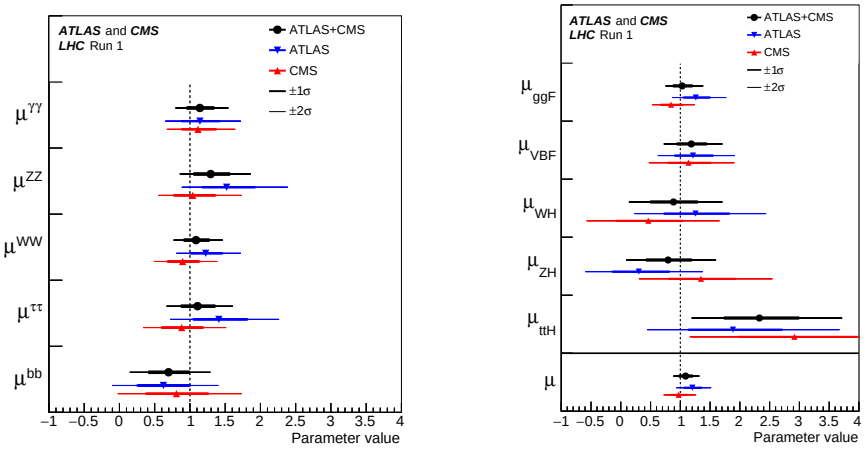

(a) (b)

Figure 2.4: Best fit values for the Higgs boson signal strength (normalised to the SM value) split by decay products (a) and by production method (b) for both the ATLAS and CMS experiments[27].

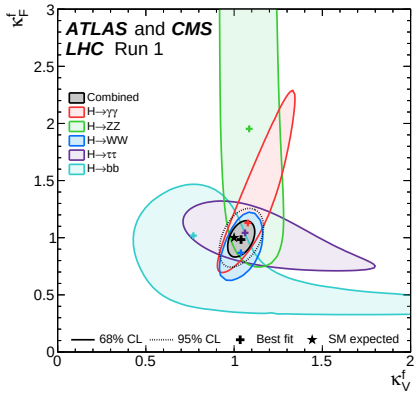

Figure 2.5: Likelihood contours at 1σ for Higgs boson coupling (normalised to SM value) to fermions (κ_F) and heavy bosons (κ_V) for each Higgs decay channel using the combination of ATLAS and CMS results[27].

been performed by CMS and ATLAS[29, 30] using the interference between non-resonant di-boson Feynman diagrams and Higgs diagrams. Currently, all values in the region $\Lambda_H > 17$ MeV have been excluded with 95% confidence by ATLAS and the region $\Lambda_H > 14$ GeV by CMS. This limit represents approximately four times the predicted width of the Standard Model Higgs boson, 4.1 MeV.

Chapter 3

The ATLAS Experiment

The primary apparatus of the ATLAS experiment[31] is one of four detectors located on the colliding ring of the Large Hadron Collider (LHC)[32]. The ATLAS detector, along with the CMS detector, was designed to be multi-purpose; capable of reconstructing all Standard Model particles (except the neutrino) and capable of probing the full possible mass range of the Higgs boson[33]. The ATLAS experiment is operated from Meryn, Switzerland, at the headquarters of the European Organisation for Nuclear Research (CERN). The ATLAS experiment directly involves the work of approximately 3000 physicists from over 175 institutions and 38 countries. The ATLAS experiment was officially started in 1992, recorded its first stable collision dataset in 2010, and was involved in the simultaneous and independent discovery of the Higgs boson (in conjunction with CMS) in 2012 [34].

3.1 The Large Hadron Collider

The LHC conducts proton-proton (pp) collisions at a centre of mass energy of 7, 8 and 13 TeV and designed to reach a maximum of 14 TeV[32].

The LHC accelerator complex consists of a chain of injectors which accelerate particles in stages. The protons are first accelerated to 50 MeV using a linear accelerator, LINAC3. They are then passed into three storage rings refered to as the Proton Synchrotron, Proton Synchrotron Booster and Super Proton Synchrotron; where particles are subsequently boosted to 1.4, 26 and 450 GeV before entering the main colliding ring. The main colliding ring, approximately 26.7 km long, then boosts the particle to their final collision energy which is currently set at 6.5 TeV[35]. This is shown in Figure 3.1a and schematically in Figure 3.1b.

(a)

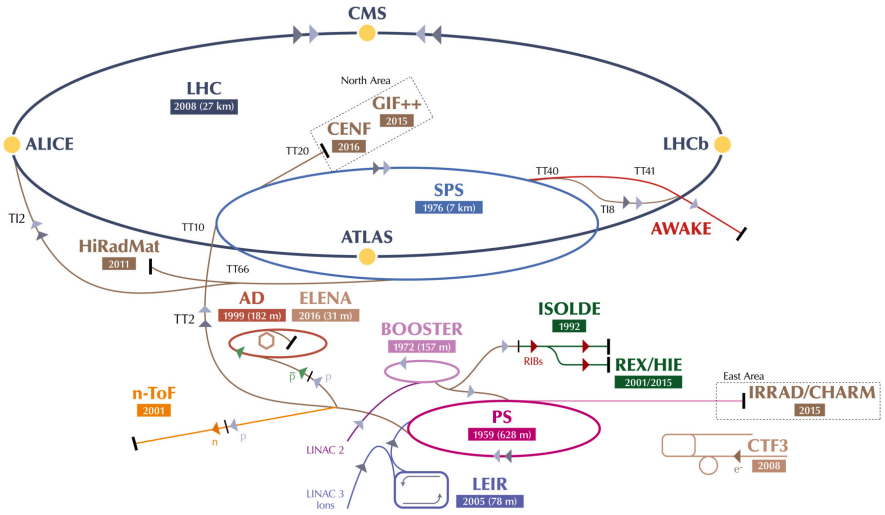

(b)

Figure 3.1: (a) shows a satellite image of Geneva with the location of the LHC rings and detectors overlaid. (b) shows a pictorial representation of the colliders complexes hosted at CERN. Of relevance to the ATLAS experiment are the Proton Synchrotron Booster (Booster), Proton Synchrotron (PS) and the Super Proton Synchrotron (SPS). © CERN

Table 3.1: Selected parameters describing the beam conditions delivered by the LHC[36, 37].

Beam Conditions	2010	2011	2012	2015	2016
$\sqrt{s}$ [TeV]	7	7	8	13	13
Bunch spacing [ns]	150	50	50	25	25
Typical Bunch Population [10^{11} protons/bunch]	0.9	1.2	1.7	1.2	1.2
Peak luminosity [$10^{33} cm^{-2} s^{-1}$]	0.2	3.6	7.7	6.3	11
Peak number of inelastic interactions per crossing	5	20	40	40	39
Average number of interactions per crossing	2	9	21	21	27
Total Integrated Luminosity Delivered [fb^{-1}]	0.047	5.5	23	5.0	31

The most relevant properties of the resultant beams are summarised in Table 3.1.

Once accelerated to the required energies, the particles are directed, in bunches separated by 25 ns (50 ns at 7, 8 TeV), into the four interaction points around which the four main experiments at the LHC are situated:

1. ATLAS[31] - general purpose, including Higgs, Standard Model and exotic searches.
2. CMS[38] - general purpose like ATLAS, but using complementary technology.
3. LHCb[39] - conduct measurements using B-mesons.
4. ALICE[40] - study high energy collisions of lead ions.

3.1.1 Pile-up and Beam Conditions

An event is defined as a bunch crossing in which at least one scattering (event) took place. Pile-up refers to any process which may degrade detector performance due to the overlap of multiple collisions within an event. Pile-up can be divided into 'in-time' and 'out-of-time' pile-up. In-time pile-up refers to the interaction between multiple collisions within a bunch crossing whereas out-of-time pile-up refers to collisions from different bunch crossings interfering. In-time pile-up is typically from multiple 'soft' (elastic) interactions between protons. By contrast, out-of-time pile-up typically arises because the recovery time of the electronics is much greater than the frequency of proton bunch crossings. The period of bunch crossing is currently 25 ns in contrast to the signal integration time of approximately 250 ms for portions of the ATLAS calorimeters.

Pile-up may result in phantom particles, and reduce the performance of the detector for particle and event reconstruction. The primary measure of pile-up is the number of interactions per bunch crossing (μ). The number of interactions per crossing are shown in Figure 3.2. The progression from Run I (2010-2012) to Run II (2015 onwards) is characterised by increased energy, luminosity and frequency of bunch crossings which is at the expense of greater activity within the detector from pile-up.

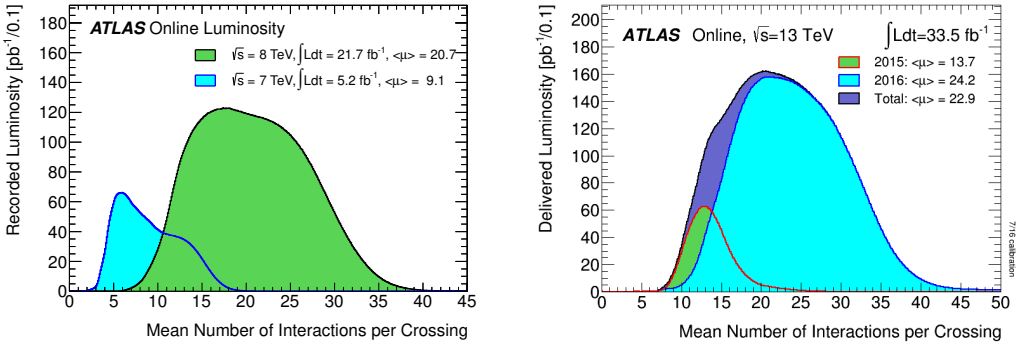

(a) (b)

Figure 3.2: Luminosity weighted distribution of the average number of vertices reconstructed in Run 1 and Run 2[41].

3.1.2 Luminosity Measurement

The measurement of the luminosity delivered to ATLAS by the LHC is measured by the LUCID and BCM detectors as well several subsystems of the ATLAS detector[36]. The main method used to measure the luminosity is through beam separation scans, also known as Van der Meer scans. The instantaneous luminosity ($\mathscr{L}$) for two colliding beams can be calculated as:

$$\begin{aligned}\mathscr{L} &= n_b f_r n_1 n_2 \iint \rho_1(x,y)\,\rho_2(x,y)\,dxdy, \\ &= \frac{n_b f_r n_1 n_2}{2\pi \Sigma_x \Sigma_y}\end{aligned}$$

where n_b is the number of protons per bunch crossing, f_r is the revolution frequency for the proton around the colliding ring, ρ is the normalised particle density in the transverse plane, $\Sigma_{x,y}$ are the convolved beam widths and $n_1 n_2$ is the bunch population product. Implicit in the above equation is the assumption that the transverse density factorises as $\rho(x,y) = \rho(x)\rho(y)$.

The ratio: $\frac{\Sigma_x \Sigma_y}{n_1 n_2}$ can be expressed in observable quantities through:

$$\frac{\sigma_{vis}}{\mu_{vis}^{max}} = 2\pi \frac{\Sigma_x \Sigma_y}{n_1 n_2}$$

where σ_{vis} is the cross-section for pp inelatic scattering within the detector's acceptance range and μ_{vis}^{max} is the average rate of interactions occuring during a bunch crossing and within the detectors acceptance.

The approach taken by ATLAS is to use several techniques to measure the luminosity and take the difference as a systematic error on the measurement. Of the above values, μ_{vis}^{max} can be calculated using the ATLAS inner detector and LUCID; the bunch population product $(n_1 \cdot n_2)$ is based on beam current measurements produced by the LHC collaboration; and the convolved beam widths $(\Sigma_x \Sigma_y)$ are measured using the root-mean-square of the beam widths (where a Gaussian beam distribution is assumed). An example of the particle density distribution for a beam produced at the LHC is shown in Figures 3.3.

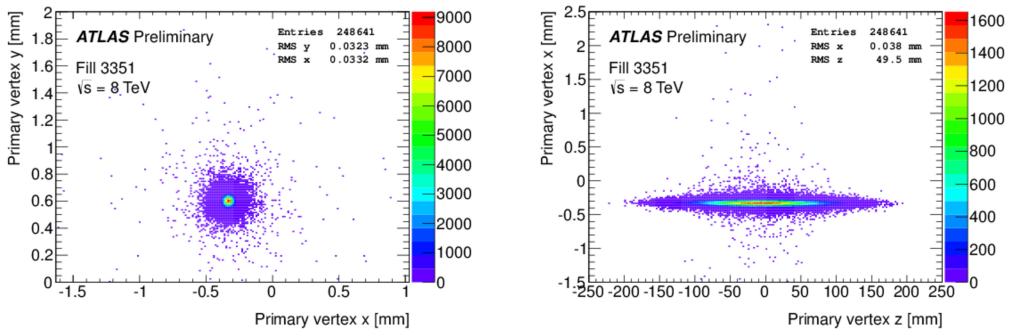

(a) (b)

Figure 3.3: (a) and (b) shows the beam density distribution in the x-y and x-z plane respectively. This beam cross-section was generated from fill 3351 with a beam collision energy of 8 TeV[41].

Alternatively, the ATLAS foward and tile calorimeters can provide a bunch blind luminosity measurement using the total calorimeter currents. These are generally used to measure slow drifts in the luminosity over time. This process is complicated by the non-linear relationship between total luminosity and calorimeter current. Along with the BCID detector, this is used to measure the long term stability of σ_{vis} over time.

The luminosity delivered to ATLAS differs slightly from the luminosity recorded due to inefficiencies in the data acquisition system as well as short periods (especially at start-up)

when the detector may be unreceptive.

The total recorded luminosity, as calculated by these methods, is used by all analyses within ATLAS to normalise any simulated events. The time series of the integrated luminosity for Run 1 (2010-2012) and Run 2 (2015-2016) are shown in Figure 3.4. The datasets used in this thesis are the 23 $\text{fb}^{-1} \pm 2.8\%$ recorded at 8 TeV and the first 13.2 $\text{fb}^{-1} \pm 2.7\%$ recorded at 13 TeV.

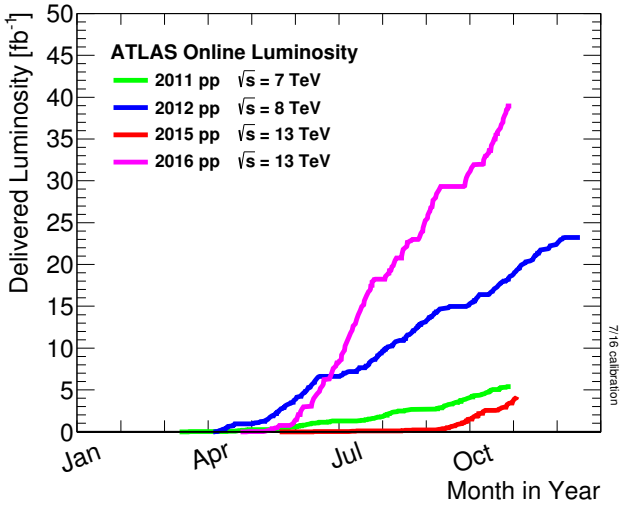

Figure 3.4: A breakdown of the luminosity delivered by the LHC and recorded by ATLAS in 2011, 2012, 2015 and 2016[41].

3.2 The ATLAS Detector

The ATLAS detector is one of two multi-purpose detectors located on the LHC. Along with CMS, it is designed to perform a wide range of searches for new physics at the GeV and TeV scale, as well as perform precision tests of the SM. In particular, the ATLAS and CMS detectors were designed to be able to probe the full possible mass range of the Higgs boson, from 100 GeV to 1.4 TeV. To perform these searches, the following principles were laid out at its inception:

- A tracking system capable of accurate and efficient track reconstruction for charged particles with high momentum.
- Calorimeters capable of accurate energy measurements for muons, electrons, jets and hadronic tau decays.

- Capable of covering a wide range of angles with high granularity.
- Efficient reconstruction of primary and secondary vertices
- Capable of operating in the high radiation environment present when the LHC is operational.

A cross-sectional view of the ATLAS detector is shown in Figure 3.5 with the major subsystems labelled. The ATLAS detector is located within Underground Cavern 1 at CERN.

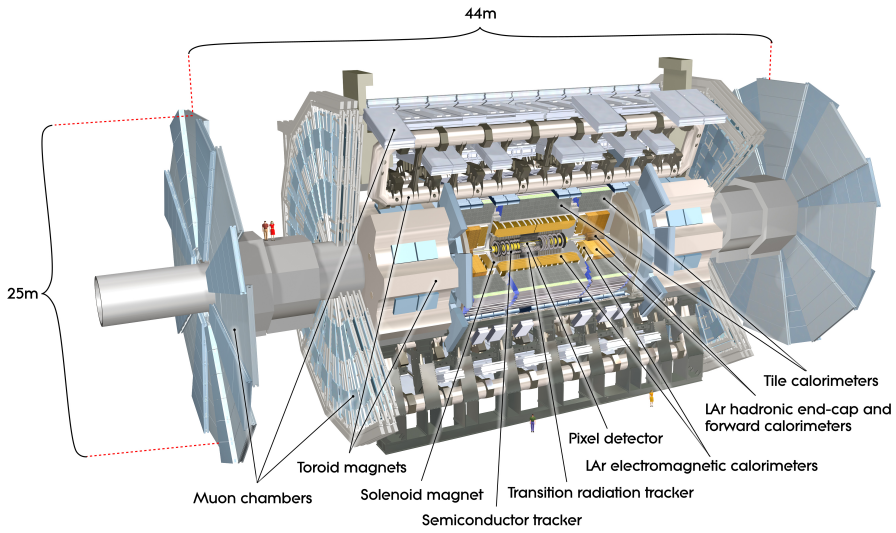

Figure 3.5: A cross-sectional view of the ATLAS detector. All main components and subsystems are listed. © CERN

3.2.1 Coordinate System in ATLAS

The interactions of interest for most of the physics program at ATLAS are those occuring between the proton's constituents which result in the inelastic scattering of protons. These are referred to as 'hard processes'. The quarks and gluons of the proton can carry a variable fraction of its energy and momenta. As a result, the centre of mass frame of the interactions cannot be determined *a priori* for any process containing missing energy.

The natural symmetry of a hadron collider is therefore rotational invariance about the beam direction and invariance under relativistic boosts parallel to the beam. This makes a

standard (right-handed) Cartesian coordinate system unhelpful. Using these symmetries, the following conserved values become significant:

- p_T - Momentum transverse to the beam direction,
- ϕ - Angle of rotation about beam,
- y - rapidity parallel to the beam,

where the rapidity, in natural units, is defined as:

$$y = \frac{1}{2} \log \frac{E + p_L}{E - p_L} \tag{3.1}$$

where p_L is the component of the objects momenta parallel or longitudinal to the beam. The rapidity is often approximated to the pseudo-rapidity (η):

$$\eta = -\log \left[\tan \left(\frac{\theta}{2} \right) \right], \tag{3.2}$$

where θ is the angle relative to the beam direction. This approximation is valid for particles with a mass much smaller than the centre of mass of the interaction, which is true for all leptons and most jets produced at the LHC.

The choice of rapidity, or pseudo-rapidity, is that it transforms under longitudinal boosts as:

$$\eta \to \eta + \beta, \tag{3.3}$$

where β depends on the magnitude of the boost and is independent of η. This allows the difference in rapidity, $\Delta\eta$ between any two objects to be conserved under boosts parallel to the beam.

With this coordinate system, the angular distance between two particles becomes:

$$\Delta R = \sqrt{\eta^2 + \phi^2}, \tag{3.4}$$

which, along with p_T, $\Delta\eta$ and $\Delta\phi$, is independent on the relationship between the centre-of-mass and lab frame.

A further convention defines the z-axis as being parallel to the beam's direction and the x-y axes are chosen so that they are right-handed and the axes are parallel or perpendicular

to the ground respectively.

Coordinate Systems for Track Reconstruction

For tracking, a perifocal coordinate system is used with the focus of the coordinate system being the collision or decay vertex of interest. In this coordinate system, the impact parameters are calculated by projecting the point of closest approach of the particle to the vertex onto the z-axis and also onto the x-y plane. The distances associated with these parameters are referred as z_0 and d_0 respectively. The impact parameters are shown diagramatically in Figure 3.6.

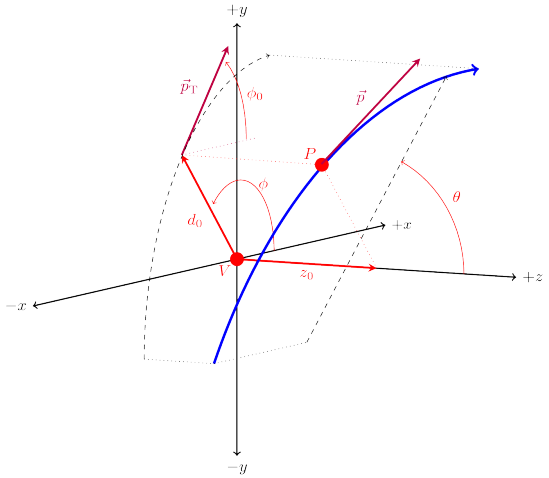

Figure 3.6: This figure provides an overview of the coordinate system used for tracking within ATLAS. The figure shows the path traced out by a particle in blue with the V denoting the vertice of interest and P as the point along the track closest to the primary vertice.[42]

3.2.2 Detector Components

Magnet System

The ATLAS detector uses a system of solenoidal and toroidal magnets to create a non-uniform magnetic field which can be used to measure the charge and momentum of particles. The three magnet systems are the barrel toroid, endcap toroid and central solenoid. The solenoid magnets encompass the ID while the toroids are located around the MS. The magnetic field generated varies between approximately 2 and 8 T. The

distribution of the magnetic field is optimised to be strongest in the inner detector region and in the muon spectrometers[43].

Inner Detector

After the beam pipe, the innermost portion of the detector consists of the insertable b-layer (IBL) followed by the remaining pixel detector, semiconductor tracker (SCT), and transition radiation tracker (TRT). In the period between final data in 2012 and first beam splash in 2015, the IBL was added to the detector in the space created by replacing the beam pipe. The function of the inner detector is to record 'hits' from the passage of charged particles from the beam pipe. These hits can then be used to reconstruct the trajectories (or 'tracks') of these particles.

The most sensitive layers, with the finest resolution (IBL and pixel detector) are located closest to the beam pipe where the angular separation between tracks is smallest. The SCT provides a more economical approach to tracking, but this comes at the expense of resolution.

The TRT functions by enclosing xenon and argon gas in straws consisting of material designed to induce radiation in charged particles. The quantity of radiation emitted is a function of the mass and energy of the particles. This is mainly used for the identification of electrons and can be used to discriminate against hadrons, particularly pions.

The intrinsic resolution of the pixel layers are approximately 10 μm transverse to the beam and 115 μm parallel to the beam. The SCT by contrast has a resolution of 17 and 580 μm in each respective direction. The resolution of the TRT is limited by the size of the straws with a resolution of approximately 130 μm along only one axis. This direction is in R-ϕ in the barrel region and R-z in the endcap region. The three dimensional coordinates of the track are provided by the pixel and SCT layers.

Calorimeters

The inner detector is enclosed by a system of calorimeters. The principal purpose of the calorimeter is to absorb the incident particles and use the resulting deposits to

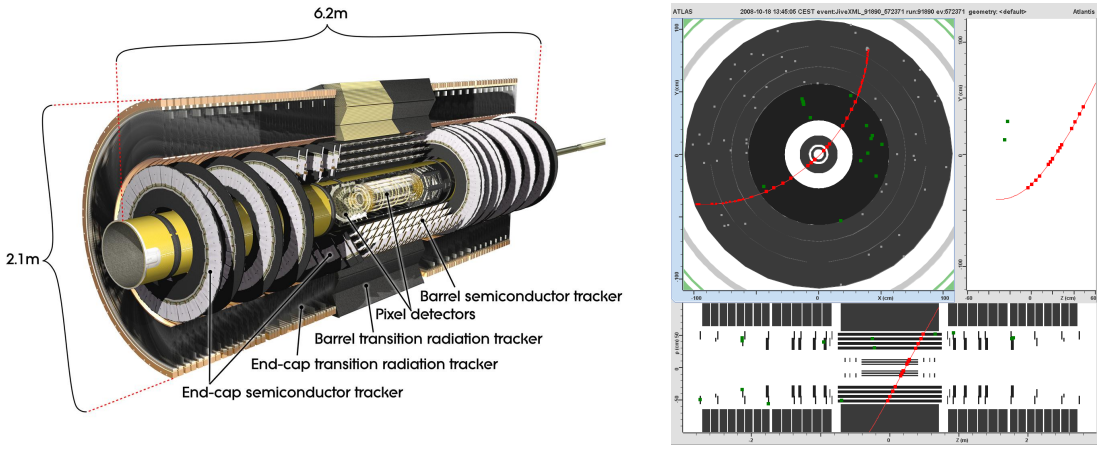

(a) (b)

Figure 3.7: (a) shows a cross-sectional view of the ATLAS Inner Detector. The three main subsystems are labelled with the exception of the IBL which was incorporated into the detector in the shutdown period between 2012 and 2015. (b) shows the pixel hits and path (in red) from a cosmic muon recorded during a cosmic run in which the detector is exposed to the sky and no beam is circulated. In (b), the top figure shows the x-y cross-section of the pixel detector and the bottom figure shows the y-z cross section. © CERN

estimate their energy. The two distinct calorimeters that are used are referred to as the Electromagnetic Calorimeter (ECAL) and the Hadronic Calorimeter (HCAL).

The ECAL has the finest granularity of the two. It is designed to completely absorb the energy of photons and electrons by inducing Bremmstrahlung radiation or pair production. This process happens continually until the final particles have little to no energy left leaving behind only a 'shower' in the ECAL. The shape of shower is also used to provide additional discrimination between photon and electrons as well as other hadrons. The ECAL consists of lead and liquid argon interleaved with readout electrodes in an accordion shape. In the endcap region, copper is substituted for lead as the absorber. This geometry allows three layers of measurement in the inner region, $|\eta| < 2.5$, and two in the high rapidity region, $2.5 < |\eta| < 3.2$.

The HCAL has a coarser granularity and is designed to stop all hadrons. The HCAL uses scintillator material to convert the hadron's energy into electromagnetic radiation. The radiation is then amplified by photo-multiplier tubes before being read-out by the detector. The HCAL is mainly used in the reconstruction of jets and identifying the presence of missing energy. The HCAL also serves as a buffer, preventing hadronic matter

penetrating the calorimeter system and interacting with the muon spectrometers. In the barrel region and the extended barrel region ($|\eta| < 1.0$ and $1.5 < |\eta| < 3.2$), the HCAL consists of the Tile Calorimeter which is composed of steel absorber in conjunction with scintillating tiles. The high rapidity region, $3.1 < |\eta| < 4.9$, uses tungsten as the absorber and liquid-argon as the active material.

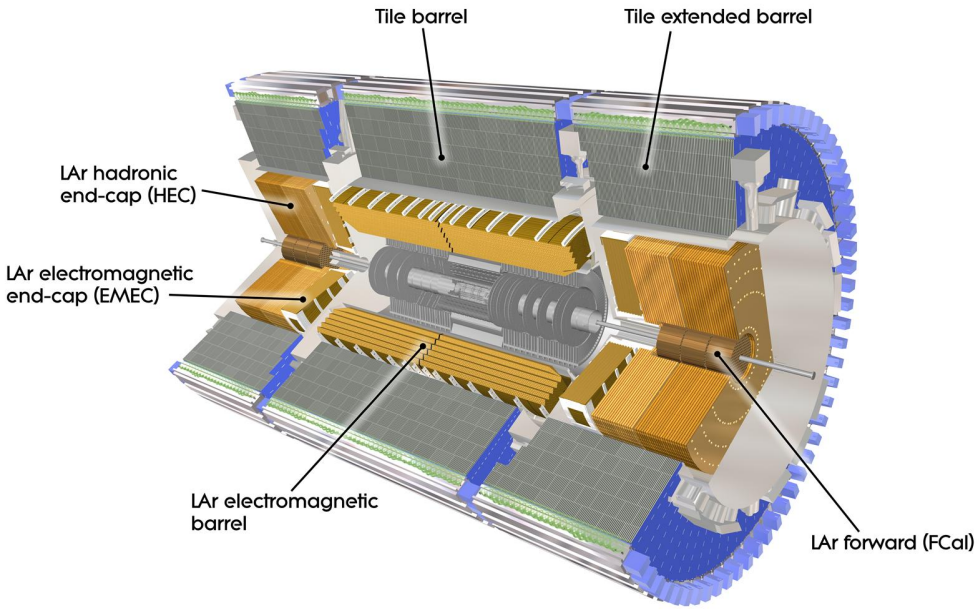

Figure 3.8: A schematic of the calorimeter system for the ATLAS detector. © CERN

Muon Spectrometer

The largest portion of the ATLAS detector is the Muon Spectrometer (MS). The MS consists of four components: monitored drift tubes (MDTs), cathode strip chambers (CSCs), resistive plate chamber (RPC), and thin gas chambers (TGCs).

This component is designed specifically to identify and measure the momentum of muons. At the energies at which they are produced by the LHC (of order 10-100 GeV), the muons are minimum ionising particles and are able to pass through the calorimeters. To measure their momentum, the amount of bending present in their tracks is used. The momentum resolution of muons is, hence, a function of the magnetic field strength and size of the spectrometer.

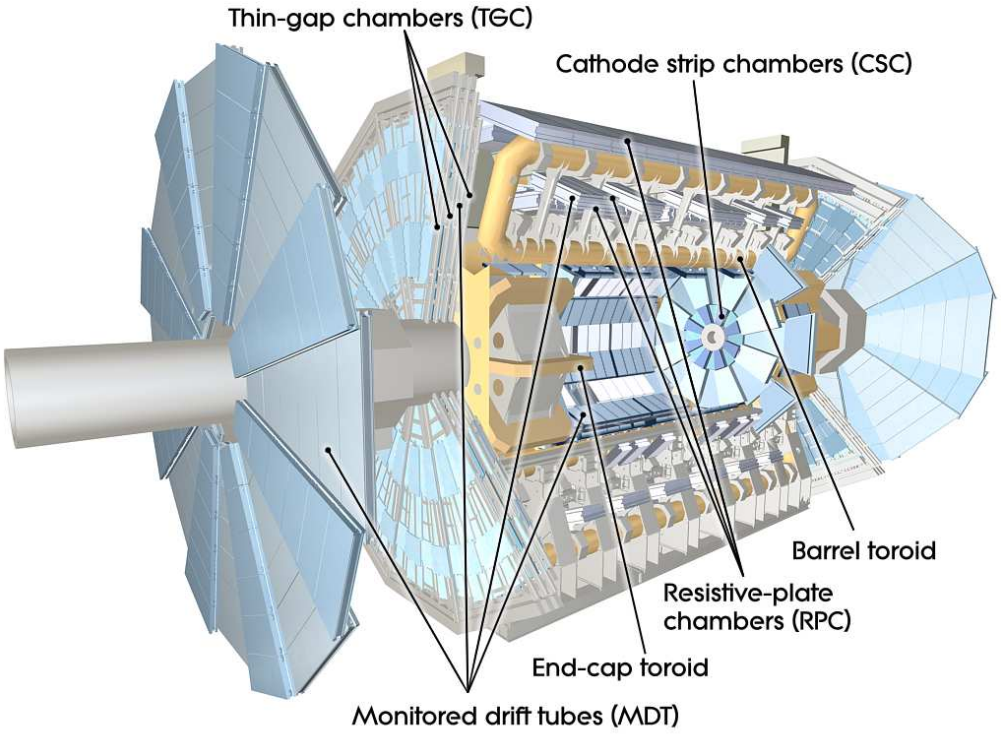

Figure 3.9: A schematic of the muon detector system for the ATLAS detector. © CERN

3.2.3 Trigger and Data Acquisition System

Most bunch crossings that occur within the ATLAS beam pipe produce events in which only elastic scattering or low energy interactions have taken place. These events, which produce multiple low p_T jets, dominate by several orders of magnitude over the electroweak processes that are of interest. The relative cross-sections for these processes are shown in Figure 3.10. The ATLAS detector is hence calibrated to collide protons at a higher rate than its capacity to record them and the trigger is optimised to identify physically interesting events at a rate that can be processed by the data acquisition system and storage farm. In 2015-2016, ATLAS was delivered a beam with a bunch crossing frequency of 40 (20 in Run 1) MHz. The trigger and data acquisition system (TDAQ) stores events at the rate of 1 kHz. A summary of the ATLAS TDAQ is shown in Figure 3.11.

The TDAQ is composed of a hardware and software system. The hardware portion consist of the front-end electronics and the level one (L1) trigger. The L1 trigger operates at the full 40 MHz rate and reduces this down towards an average rate of 100 (70 at Run 1) kHz using information from the muon system and calorimeters operating at a coarser

granularity. 100 kHz forms a hard limit on the number events that the DAQ is able to process. Events that are retained typically demonstrate large transverse energy or large energy imbalances in the transverse plane.

In Run 1, the next component of the trigger (L2 and Event Filter) further reduce this to approximately 4 kHz and 1 kHz respectively. L2 uses a portion of the tracking information and the calorimeters whereas the Event Filter uses the full available information. In Run 2, the L2 and Event Filter has been merged into a single system referred to as the High Level Trigger (HLT) which uses all information available to the Event Filter. The final rate at which data is stored has been further reduced from 1 kHz to approximately 300 Hz. This corresponds to approximately 450 MB/s in Run 2 and 1 GB/s for Run 1[44].

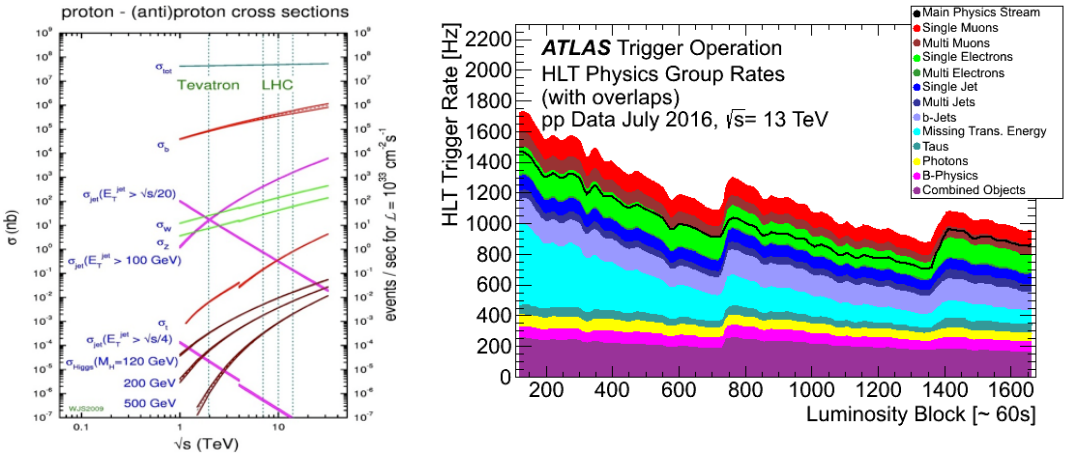

Figure 3.10: (a) shows the cross-section of various processes as a function of beam energy. The electroweak processes are several orders of magnitude smaller than the soft processes[45]. (b) shows the allocation of trigger rates for different processes as a function of the luminosity block from a single months data-taking in 2016[44].

3.2.4 Overview of Reconstructed Objects

The following objects are reconstructed by the ATLAS detector:

- **Electrons and Photons:** Photons and electrons as energy clusters in the electromagnetic calorimeter[46]. Photons are differentiated from electrons by both the shape of the energy deposits in the calorimeter and the existence of associated tracks in the inner detector. Both particles are expected to be completely absorbed by the ECAL[47–49]. Electrons with transverse energy greater than 5 GeV are reconstructed in the central region of the detector ($\eta < 2.5$). In the foward regions

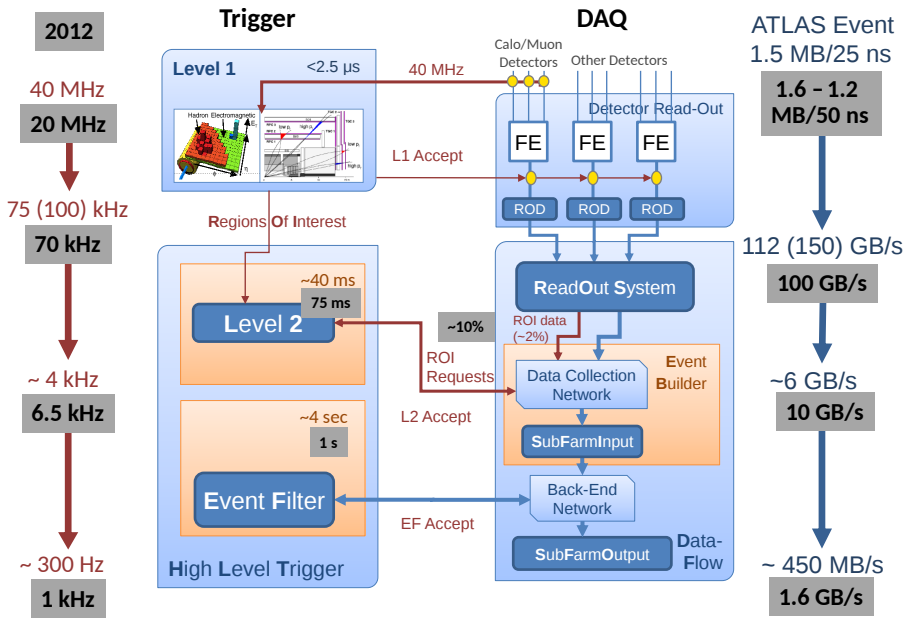

(a)

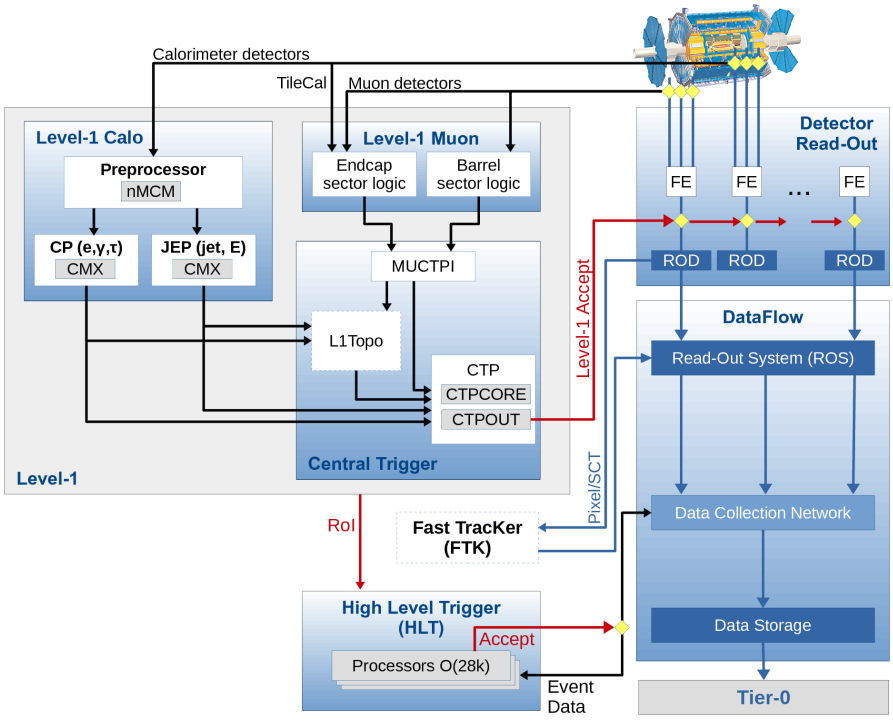

(b)

Figure 3.11: This figure provides an overview of the ATLAS Trigger and Data Acquisition System used in both Run 1 (a) and Run 2 (b)[44].

($2.5 < \eta < 4.9$), where tracking information is not present, electrons are required to have a transverse energy greater than 20 GeV. Photons with transverse energy greater than 15 GeV are reconstructed in the central region. Neither electrons nor photons are reconstructed in the region of the calorimeter crack ($1.37 < \eta < 1.52$).

- **Muons:** Muons are characterised by their small deposits of energy in the calorimeters and the presence of tracks in both the inner detectors and the MS. The curvature of the tracks in both the inner detector and the MS are combined to measure the muons momentum. Muon reconstruction in ATLAS is characterised by both accurate momentum reconstruction and the high rejection of hadronic fakes[50]. A more comprehensive discussion of muon reconstruction can be found in Chapter 4.
- **Jets:** Jets occur in ATLAS as localised clusters of energy deposited in the calorimeters. An anti-k_t algorithm with radius of $\Delta R = 0.4$ is used to tag jets[51, 52]. The energy calibration for these jets are described in References [53–57].
- **B-jets:** ATLAS reconstructs b-quark initiated jets as regular jets but with additional requirements based predominately on how collimated the jets are and the presence of a secondary displaced vertex[58].
- **Taus:** Taus in ATLAS decay within the beam pipe of the detector and can only be reconstructed from their decay products. The decays occur via a charged current to either lighter leptons or quarks. The lighter leptons are indistinguishable from prompt leptons and hence, can't be tagged as having originated from taus. The hadronic decays have distinctive features which allow it to be tagged as originating from a tau. The tagging and reconstruction of tau decays into hadrons will be discussed in more detail in Chapter 5.

Missing Transverse Energy

The collision of composite particles means that the initial momentum of the interacting constituents are unknown however the partons can be assumed to be at rest relative to the transverse direction of the beam. Hence, any imbalance in energy conservation in the direction transverse to the beam can be inferred. Missing Transverse Energy (MET), E_T^{miss}, can arise because of mis-reconstruction of particles, the production of weakly interacting particles (such as neutrinos) in the final state, or dead regions within the detector. The precise definition of MET is varies depending on the final state of the

process of interest but broadly, it is measured using all reconstructed particles associated with a vertex with the addition of a 'Soft Term'. The Soft Term seeks to improve the resolution of the MET by removing contributions which may arise from pile-up, and other energy deposits not associated with an object.

In the data taken from 2011 and 2012, the MET Soft Term is calculated using calorimeter clusters not associated with any reconstructed object[59]. In 2015 and 2016, the Soft Term was generated using the TrackSoftTerm algorithm [60, 61] which derives the contributions using tracks.

3.3 Simulation of the ATLAS Detector

The generation of the samples involves the interaction of multiple pieces of software. A brief overview is presented here. For brevity, simulated samples are typically refered to as Monte-Carlo (MC), named from the technique used by the event generators.

The parton distribution functions (PDFs) are generated and used to simulate the distribution energy carried by the fundamental particles which constitute the proton. These PDFs are tuned to agree with observation. The hard and soft scattering for a given process is then determined using particles drawn from the PDFs. The scattering of these particles are then determined using a scattering matrix. The elements of this matrix are generated by software referred to as 'Event Generators'. Event filters are often used to further restrict the final state to the required process. The showering and initial/final state radiation of the final particles is then calculated. The showering of quark or gluon initiated jets is especially complex and the process typically involves pair production until the confinment scale is reached at which hadronisation takes place and longer lived, colour-less particles are produced. The interaction of these particles with the ATLAS detector is simulated by GEANT4[62, 63]. Pile-up is incorporated into simulation by overlaying pile-up vertices generated by *PYTHIA*[64, 65] onto the simulation of the hard-scattering process. The simulated detector responses are reconstructed using the same software and tool chain used for the data samples.

Chapter 4

Reconstruction and Identification of Muons

The defining property of the muon at the LHC, is that they are minimum ionising particle and, as such, deposits very little energy in the calorimeters. The primary reconstruction information for muons comes from tracking information recorded by the ID and MS. A pure sample of muons is obtained in the MS by isolating it from the beam by the HCAL through which only minimum ionising particles can penetrate. Muons are, across most energy ranges, the most accurately reconstructed particle in ATLAS. The accuracy with which they are reconstructed allows them to be used to calibrate other objects and systems. The following chapter provides a brief overview of the reconstruction of muons. The muon triggers are described in more detail in Reference [66] and reconstruction algorithms and efficiency measurements are described in more detail in Reference [67]. An example of a di-muon event is shown in Figure 4.1.

4.1 Muon Trigger

Tracking information is unavailable at the L1 trigger and muons, which are minimum ionising particles at the LHC, deposit very little energy in the calorimeters. The portion of the MS used for the hardware trigger (L1) are the resistive plate chambers (RPC) in the barrel region ($|\eta| < 1.05$) and the thin gas chambers (TGC) in the forward regions ($1.05 < |\eta| < 2.4$). These systems provide over 99% coverage in the endcap region and 80% coverage in the barrel region (due to the inclusion of service and access infrastructure at $\eta \approx 0$). Multiple hits within an $\eta \times \phi$ of approximately 0.1×0.1 for the RPCs and approximately 0.03×0.03 TGCs are used to provide the initial trigger. These hits are

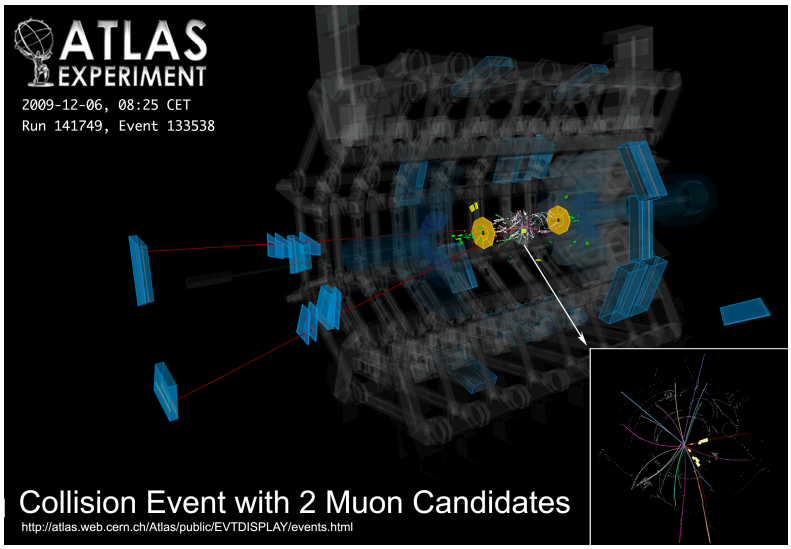

Figure 4.1: An event display of a collision with two muons reconstructed. A track fit has been successfully performed for each muon with the track shown in red. The muon tracks are visible in both the inner detector and the muon spectrometer. The event was recorded during a 7 TeV proton-proton beam[68].

required to be directed outward from the beam interaction point. At least three local hits are required to pass the L1 muon trigger. The transverse momentum of the muon is estimated at L1 by measuring the deviation of the hits from the distribution expected from an infinite energy muon.

The regions of interest (RoI) identified by the L1 trigger are then passed to the L2 (for Run 2, these pass directly to the HLT). Here, the RoIs from the TGCs and RPCs are also added to the information from the muon drift chambers (MDTs) to produce a more complete reconstruction. A track is reconstructed by fitting a parametrised curve to the hits. The outer track (formed in the muon spectrometers) is then matched to a track from the inner detector. The track closest in η, ϕ to the extrapolated outer track is chosen. These form a combined-muon which has a transverse momentum taken as a weighted average of the two tracks.

At the Event Filter, the combined-muon and RoIs from L2 are used. If no combined-muon was reconstructed, the inner detector tracks are extrapolated outwards and matched to MS tracks. A full scan procedure is also performed to find additional muons which were not identified using the L2 RoIs. These are reconstructed by attempting to match tracks throughout the MS with the inner detector tracks. The event filter also quantifies the muon's isolation by placing a threshold on the sum of the tracks' p_T within a cone of

the muon. In this method, only tracks with an energy above 1 GeV are used and the transverse momentum of the muon itself is excluded. The following isolation criteria was used in Run 1:

$$\Sigma_{\Delta R<0.2}\frac{p_T^{\text{track}}}{p_T^{\text{muon}}} < 0.12. \tag{4.1}$$

In Run 1, the two main physics triggers of relevance in this thesis are the `mu24i`, `mu36` and `mu18_mu8`. The mu24i trigger requires one or more combined-muons with $p_T > 24$ GeV. The `mu36` requires one or more combined-muons with $p_T > 36$ GeV but does not apply the isolation condition. The di-muon trigger, `mu18_mu8_FS`, requires at least one combined-muon with $p_T > 18$ GeV and two or more full-scan muons with $p_T > 8$ and $p_T > 18$ GeV.

4.1.1 Trigger Performance

A tag and probe method is used to measure the efficiency of the muon triggers. For the low p_T case ($p_T \lesssim 100$ GeV), di-muon decays from either a J/ψ or Z are targeted. A single muon trigger is used to tag one of the muons while the possible presence of a second muon is used to test the performance of the other trigger. To target higher p_T muons, a missing energy trigger is used to select single muon decays from either a W boson decay or from a top process. Between simulation and data, the efficiency of the trigger was found to be consistent to within one percent.

4.2 Muon Reconstruction

Combined (CB) muons are reconstructed independently in the ID and MS and then combined by either inward or outward extrapolation from these systems. These are the main type of reconstructed muon.

Two different software chains are used to reconstruct muons. These are referred to as STACO and MUID. These two algorithms have been shown to produce compatible results and provide redundancy to muon reconstruction. The strategy used by STACO involves performing a statistical combination of the existing tracks' parameters whereas MUID performs a global refit. The similarity of the results allows the use of only the STACO

muons in the results of this thesis. In Run 2, these two algorithms have been merged to create a single chain referred to as Unified Muon Identification Chain.

4.2.1 Muon Reconstruction Efficiency

A tag and probe method is used to measure the reconstruction efficiency of muons where a single muon trigger is used to select events and a second possible muon is probed. This involves measuring the conditional probability that a muon reconstruction by the ID portion of the detector is also reconstructed by the MS as that same type of muon. The probabilities can be represented by the function

$$\epsilon\left(\text{Type}\right) = \epsilon\left(\text{Type}|\text{ID}\right) \cdot \epsilon\left(\text{ID}\right), \tag{4.2}$$

where $\epsilon\left(\text{ID}\right)$ is the efficiency with which a muon is reconstructed in the ID. The value of $\epsilon\left(\text{ID}\right)$ cannot be measured so the following approximation is used

$$\epsilon\left(\text{Type}\right) \approx \epsilon\left(\text{Type}|\text{ID}\right) \cdot \epsilon\left(\text{ID}|\text{MS}\right). \tag{4.3}$$

The above formula is calculated for both data and simulation in a di-muon enriched region (around the J/ψ and Z peaks) and the ratio in efficiencies between data and simulation (efficiency scale factor) is applied to simulation to correct for mismodelling of muon reconstruction efficiencies. The differences in efficiencies have been measured to be within one percent of each other.

4.3 Momentum Scale and Resolution

The momentum of the muons is inferred from the track parameters of the muon track. The momentum generated by this value has an intrinsic uncertainty. To match the scale and resolution of muons reconstructed from data, a series of data driven corrections need to be applied to the simulated muons. A separate set of corrections are applied to ID and MS. These correct for energy loss due to any calorimeter material and the imperfect modelling of the magnetic field and detector geometry.

The variation in the muon momentum resolution has also been observed to vary between simulation and data. The correction has the form of a Lorentz function which compensates for fluctuations in the amount of energy absorbed by the calorimeters, the effect of multiple scatterings and misalignments between detector regions.

A template maximum likelihood fit is used to compare simulation to data and extract the parameters from the fit. Two regions of data are used corresponding to the peaks around $J/\psi \to \mu\mu$ and $Z \to \mu\mu$. The sample of events is obtained by requiring two opposite charge CB muons within a mass, $m_{\mu\mu}$, of 2.76 - 3.6 GeV or 8 - 17 GeV for the J/ψ and 76 - 96 GeV for the Z-boson.

Chapter 5

Reconstruction and Identification of Tau Leptons

The tau lepton has a mass of 1.78 GeV. The large mass of the tau gives it properties distinct from other leptons. The most important of these properties, from the perspective of the LHC experiment, is the short lifetime, a mean of $(290.6 \pm 1.0) \times 10^{-15}$s, and the large branching fraction for taus decaying to hadrons and neutrinos, 65%[15]. The short lifetime results in the tau decaying within the beam pipe of the ATLAS detector, in general within a few millimeters of its primary vertex. Hence the tau lepton decays before it reaches the active parts of the detector and can only be reconstructed from its decay products.

The tau decays almost exclusively through the W boson via the charged weak current. The decay products of the tau lepton are either lighter leptons or quarks. The leptonic decay modes are indistinguishable from prompt leptons, but the hadronic decay modes do provide a distinctive signature. In this thesis, as within ATLAS, tau reconstruction will refer specifically to the reconstruction of taus decaying to hadronic matter.

The majority of hadronic tau decays consist of a combination of photons, neutrinos and pions, see Figure 5.1. The decays not containing charged pions constitute only 8% of hadronic tau decays and are of less interest. The photons and pions form the detectable portion of the tau decays, $\tau_{h,vis}$. Of these components, only the charged pions interact with the inner detector and tracking system. The most likely decays of the tau contain one or three charged pions, 72 and 22% of hadronic tau decays respectively. The one or three charged pions decays can be distinguished by the number of tracks and are referred to as one or three pronged taus respectively.

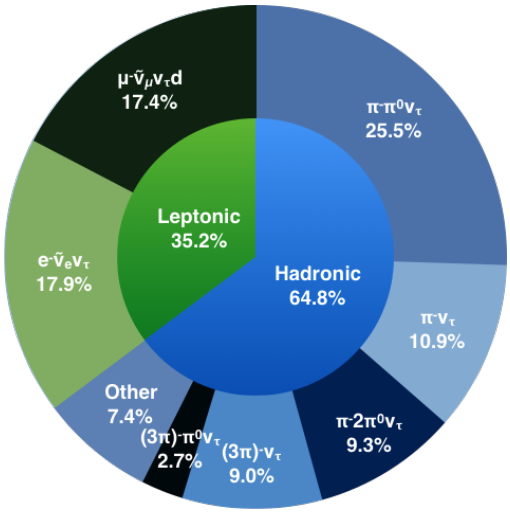

(a)

Figure 5.1: The branching fraction for each decay of a single charged tau is shown. Those that are reconstructed as light leptons are shown in blue and those that are reconstructed as hadronic taus are shown in green[15]. The charged mesons, denoted by $h^{\pm}$, are composed mainly of pions with a lower fraction of kaons.

5.1 Tau Reconstruction

The tau reconstruction algorithm is seeded using localised deposits of energy in the calorimeter. These seeds are formed using the anti-k_t algorithm with a distance parameter of $R = 0.4$ using the calorimeters as input. To form a tau candidate, the jet must have a $p_T > 10$ GeV and $|\eta| < 2.5$.

The tracking information is then considered. Tau candidates are associated to a primary vertex using the dedicated Tau-Vertex Association algorithm[69]. This vertex is required to have at least three associated tracks. The vector between the primary vertex and the calorimeter deposit is used to define a cone of $R = 0.2$. This cone contains all the tracks associated with the tau candidate. These tracks are required to have $p_T > 1$ GeV. The tracks associated with the tau candidate are then used to reconstruct the secondary vertex, corresponding to the flight of the tau from primary vertex until it decays.

The tau tracks are required to have a distance of closest approach from the primary vertex of $|d_0| < 1.0$ mm in the transverse plane and $|z_0 \sin\theta| < 1.5$ mm in the longitudinal plane[69, 70].

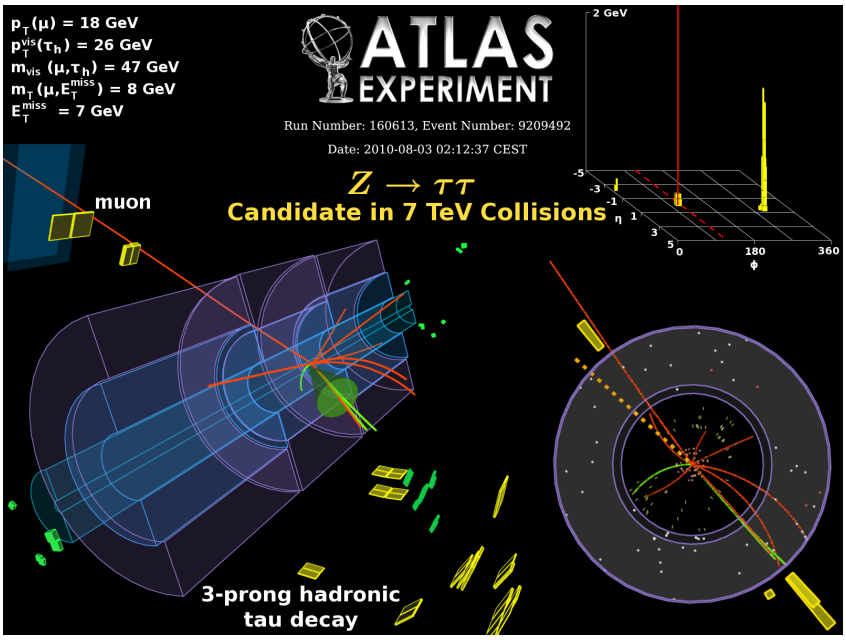

Figure 5.2: An event display of a $Z \rightarrow \tau\tau \rightarrow \mu\tau_h\nu\nu$ event reconstructed in the ATLAS detector. The reconstructed tau contains three tracks and was produced using 7 TeV proton-proton collisions[68].

5.1.1 Tau Energy Calibration

Although fundamentally a jet, the specific combination of hadrons within taus motivates the energy calibration of taus to be performed separately to that for other jets. The tau energy scale (TES) is constructed by comparing, from simulation, the true energy of tau with the reconstructed energy. The calibration function ($\mathscr{R}$) can be expressed as:

$$E^{\tau}_{\text{TES}} = \frac{E^{\tau}_{\text{reco}} - E_{\text{pile-up}}}{\mathscr{R}\left(E^{\tau}_{\text{reco}}, \eta_{reco}, \mu\right)},$$

in terms of the energy at reconstruction level (E^{τ}_{reco}), reconstructed pseudo-rapidity (η_{reco}), and the number of vertices in the recontructed event (μ). The addition of the $E_{\text{pile-up}}$ term serves to corrects E^{τ}_{reco} for the avergae amount of pile-up in the sample. The function, $\mathscr{R}$, is calibrated using simulation where E^{τ}_{reco} is fixed using the true energy of the visible products of the simulated tau.

The resolution of this is defined to be one standard deviation from fitting a Gaussian to the difference between calibrated and simulated tau energy. The uncertainty arising from

the calorimeter response is determined by convolving the single particle response function with the expected composition of the tau.An additional correction was also provided to the insitu TES by comparing the shift in the Z-peak between data and simulation, targeting the $Z \to \tau\tau$ process. Due to the limited phase space covered by $Z \to \tau\tau$, this correction mainly affects taus with a transverse momentum of 20-30 GeV.

5.1.2 Electron and Muon Discrimination

Tau jets can also be faked by lighter leptons. The most commons is electrons faking one pronged taus. To mitigate this, a separate BDT is trained on variables to discriminate taus from electrons. The disciminating power is mainly provided by the shapes of the clusters in the electromagnetic calorimeter. Generally, the electron deposits its energy in a shorter and narrower cone than the tau.

Muons can also fake taus if an energy cluster in the calorimeters is incorrectly associated with the muon track. To reduce the rate at which these fakes occur, requirements are placed on the fraction of momentum of the lead track in the tau candidate to the energy deposited in the calorimeter.

In addition to these two methods, the tau fakes are further supressed by removing objects which overlap with reconstructed electrons or muons.

5.2 Tau Identification

The process described in the previous section provides very little discrimination against jets not originating from taus. The discrimination between tau jets and other jets is performed by the tau identification algorithm.

Most jets detected by ATLAS do not originate from taus but from QCD processes. They can be divided into either quark-like or gluon-like jets depending on which particle is dominant. The concept of a quark-like or gluon-like jet is inherently ambiguous but for simplicity may be interpretted as either the parton initiating the jet or the highest energy parton within the jet. The gluon-like jets are typically less collimated than both taus and quark-like jets. Hence, the quark-like jet is typically the most difficult background to

discriminate against.

The variables chosen for background discrimination are listed below. Note that all measurements from the ECal have the appropriate corrections applied for both energy and pile-up. The contribution to the ECal due to pile-up is subtracted using a correction factor parametrized by the number of reconstructed primary vertices in the event. A plot of the important distributions are shown in Figures 5.5 and 5.6.

Central charge fraction, $f_{\mathbf{cent}}$: Fraction of transverse energy deposited in the calorimeters within the $\Delta R < 0.1$ region relative to the $\Delta R < 0.2$ region.

Leading track momentum fraction, $f_{\mathbf{track}}$: The ratio of the transverse momentum of the highest p_T track in the tau candidate relative to the energy deposited in the calorimeters.

Track radius, $R_{\mathbf{track}}$: The p_T weighted radius, $\Sigma_{\mathrm{i}} R_i p_{T,i}$, of all tracks in within a $\Delta R < 0.4$ cone about the tau candidate.

Leading track impact parameter significiance, $S_{\mathbf{leadtrack}}$: Transverse impact parameter, z_0, of the highest p_T track divided by the estimated uncertainty in the measurement.

Number of tracks in isolation region, $N^{\mathbf{iso}}_{\mathbf{track}}$: Number of tracks associated with the tau candidate within the isolation region of the tau corresponding to a cone of $0.2 < \Delta R < 0.4$ about the tau's direction.

Maximum ΔR, $\Delta R_{\mathbf{max}}$: The largest ΔR of the any track associated with the tau candidate and within the core region of the tau candidate, $\Delta R < 0.2$.

Transverse flight path significance, $S^{\mathbf{flight}}_{\mathbf{T}}$: The decay length of the secondary vertex with respect to the primary vertex in the transverse plane divided by its uncertainty.

Track mass, $m_{\mathbf{track}}$: The invariant mass calculated from the sum of all track four-momenta within a cone of $\Delta R < 0.4$ about the tau candidate.

Track-plus-π^0-system mass, $m_{\pi^0+\mathbf{track}}$: Invariant mass of the system composed of the tracks and π_0 mesons in the core region of the tau candidate.

Number of π^0 mesons, N_{π^0}: Number of π_0 mesons reconstructed in the core region.

Ratio of track-plus-π^0-system p_T, $p_T^{\pi^0+\mathbf{track}}/p_T$: Ratio of the p_T calculated using the track and π_0 information relative to the energy deposited in the calorimeter.

The information contained in these variables are then used to train a boosted decision tree (BDT) algorithm to identify taus from other jet activity. A separate BDT is trained for one and three pronged pronged taus. The BDTs are trained on taus produced by a combination of Z and W decays where the reconstructed tau matches a true tau in simulation. Z$\prime$ (a Z-boson with mass of 1-2 TeV) is also used to simulated the possible presence of taus produced by very high energy bosons. The background processes used in training the BDT are taken from data collected by the jet triggers. The discrimination of the BDT algorithm on a subset of the training samples set-aside for testing is shown in figure 5.3.

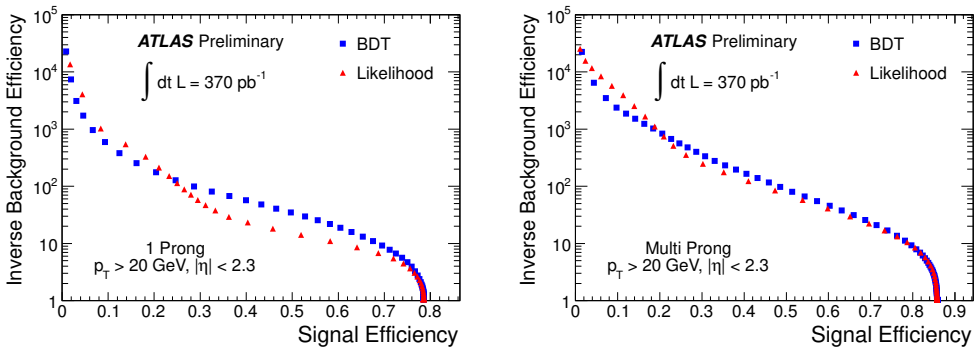

(a) (b)

Figure 5.3: The signal efficiency plotted against the inverse background efficiency for tau candidates from simulation reconstructed with $p_T > 20$ GeV. Figure 5.3a and 5.3b refer the one and multipronged cases resepectively. Both the BDT and likelihood discriminant are plotted although only the BDT is recommended for physics analyses[68].

Using the BDT, three working points are defined and referred to as loose, medium and tight. Each of these are designed to have a constant signal efficiency. These are shown separately for one and three prong taus in figure 5.4.

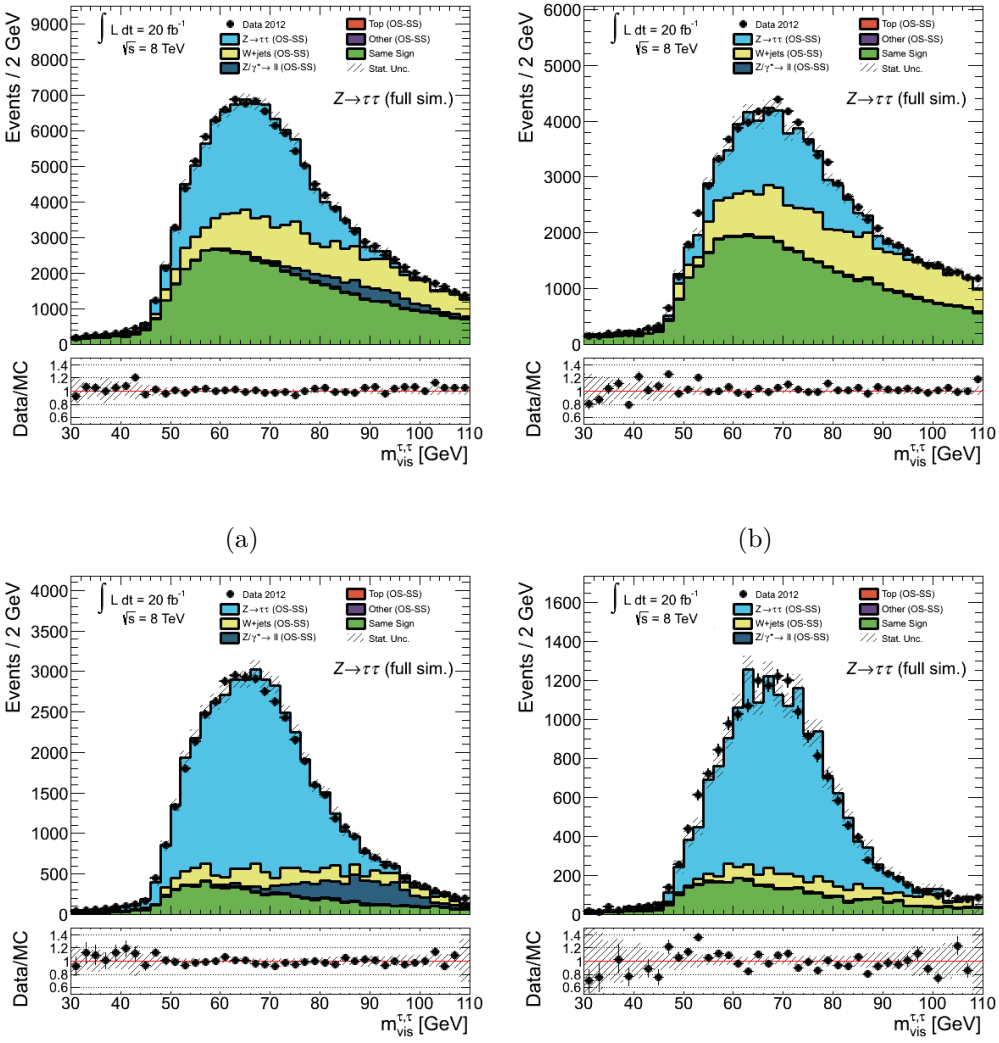

Figure 5.4: Shown are the visible mass distribution for one (left) and three (right) pronged taus using a tag-and-probe analysis for the process Z$\rightarrow \tau\tau \rightarrow \mu\tau_h$. The top row has no identification requirement whereas the second row requires that the tau pass the BDT Medium requirement.

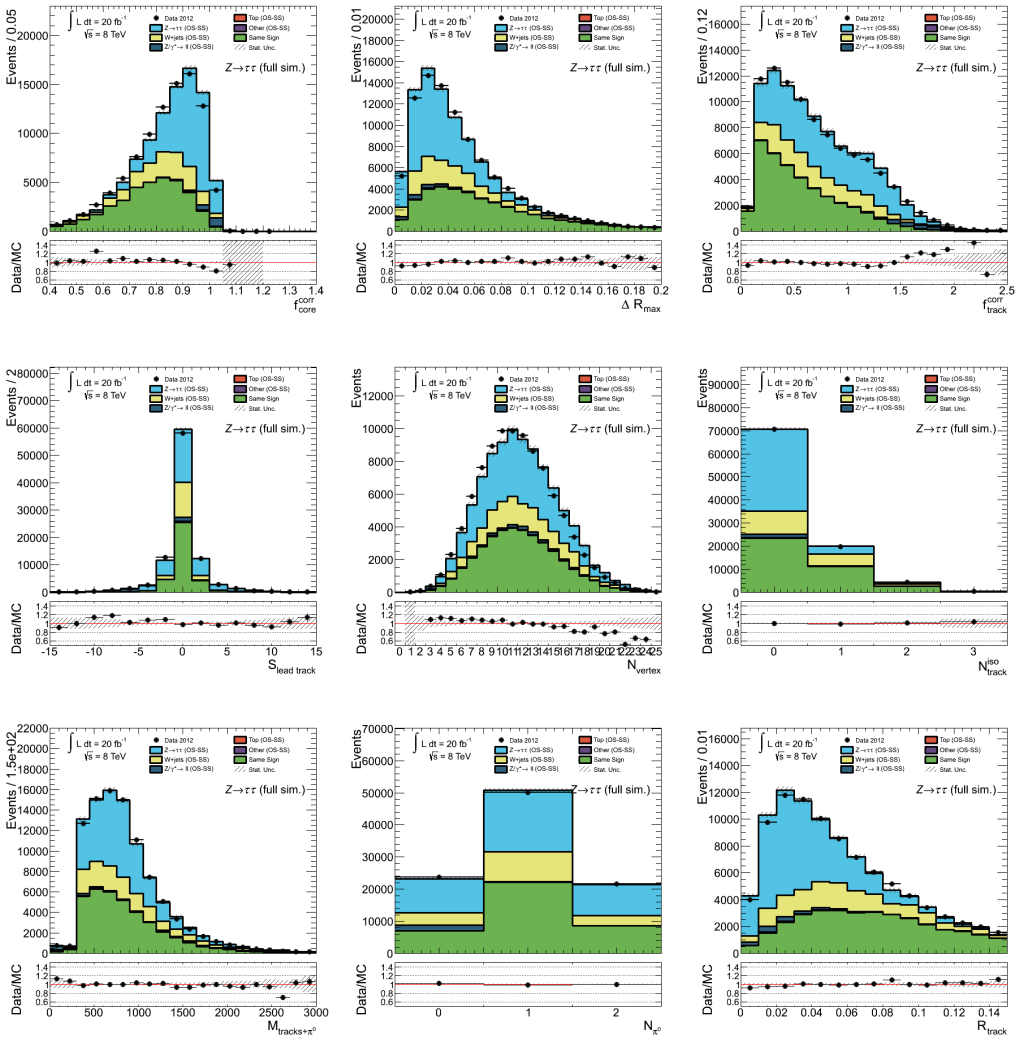

Figure 5.5: The figure shows the variables used as inputs in the one prong tau identification using a tag-and-probe analysis for the process Z$\rightarrow \tau\tau \rightarrow \mu\tau_h$ where the tau decaying into hadrons is single pronged. No tau identification requirement is placed on these variables[71].

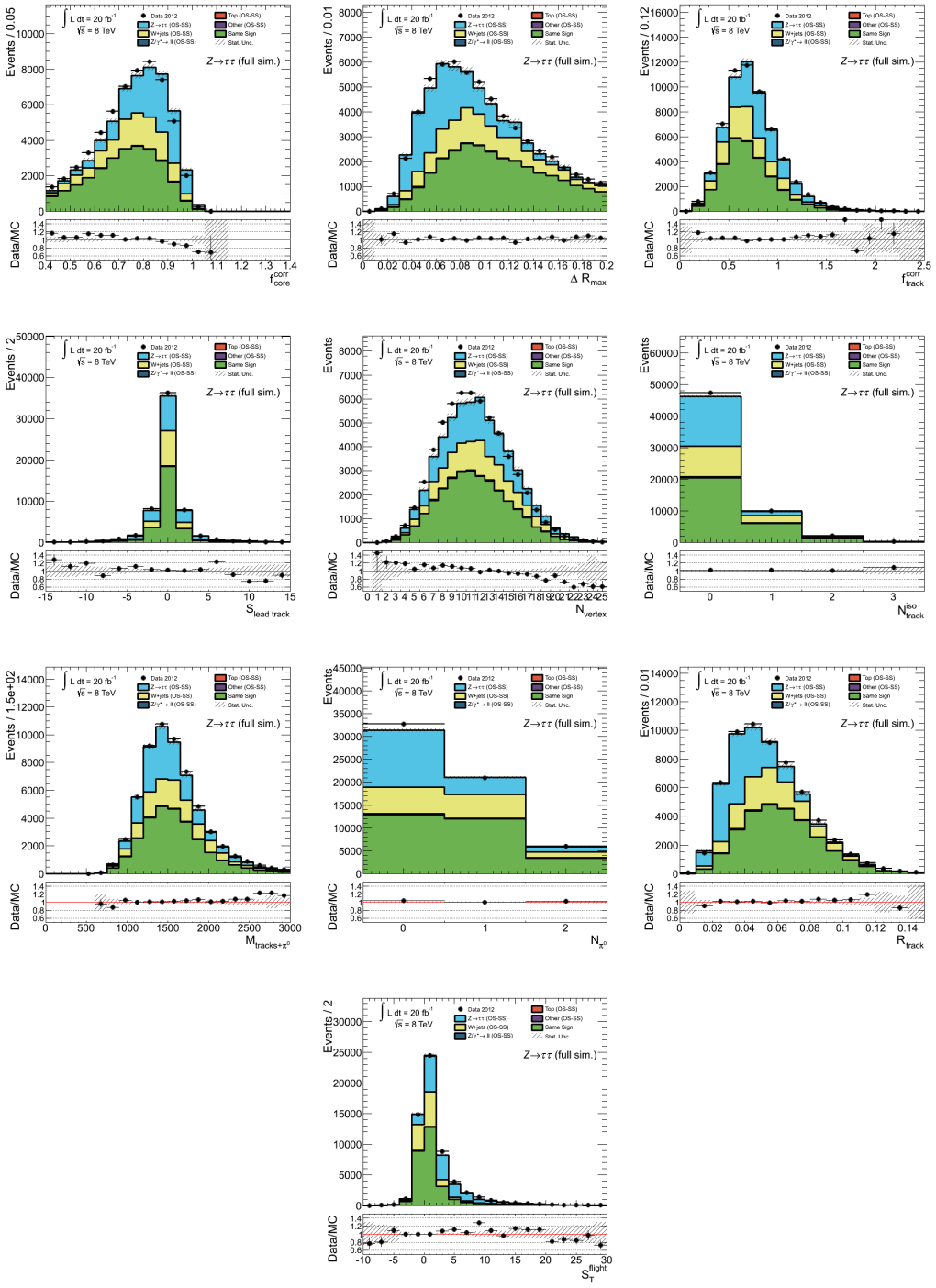

Figure 5.6: The figure shows the variables used as inputs in the tau identification for three pronged taus using a tag-and-probe analysis for the process Z→ $\tau\tau \rightarrow \mu\tau_h$ where the tau decaying into hadrons is three pronged. No tau identification requirement is placed on these variables[71].

5.3 Tau Trigger System

In Run 2, the tau trigger system consists of two systems. Level One (L1) and the High Level Trigger (HLT). A detailed description is available in Reference [72].

At L1, the only relevant information available to the trigger are the energy readouts from the calorimeter clusters, albeit with reduced granularity and resolution. For each tau, an associated set of hits in the calorimeter towers are required. Note that this energy reading differs from that available to the full analysis. These clusters are approximately 0.2×0.2 in ΔR for the taus with the surrounding and 0.4×0.4 region used to enforce isolation requirements on the taus. A requirement on the transverse energy and psuedo-rapidity is then placed on the tau.

The calorimeter clusters from L1 are then used to seed regions of interest (RoI) for the HLT. At HLT the tracking information and full resolution calorimeter information is incorporated and a subset of the kinematic variables are then used with the tau identification algorithm to further reduce the contribution of jets.

5.3.1 L1Topo Commissioning

The di-tau trigger is the highest priority tau trigger because of its importance for the Higgs boson to di-fermion measurements. An acceptable event rate and high signal acceptance for this trigger is most constrained at the L1 trigger because, in the absence of the BDT identification algorithm, there is very poor rejection of the large jet backgrounds. Only calorimeter information is available at Run 1 which limits the ways this can be ameliorated. This issue is intensified by the increase in instantaneous luminosity delivered by the LHC. The addition of the L1Topo hardware to the L1 trigger system has provided the means to reduce this event rate without compromising signal acceptance. The L1Topo, using input from the L1Calo, allows the incorporation of topological properties of the calorimeter hits into the trigger decisions[72, 73].

The method used in 2016 to reduce the rate of the primary di-tau trigger was the addition of a jet requirement with an offline transverse momentum of 25 GeV. This was preferable to increasing the tau transverse momentum thresholds (from 20 and 12 GeV respectively)

because the main $H \to \tau_h\tau_h + 2\nu$ analysis targets either a VBF topology or a boosted ggF topology. In either case, a recoiling jet is expected. The L1Topo hardware allows an additional requirements to be placed on the event, $\Delta R_{\tau\tau} < 2.9$, to further reduce the trigger rate. This is once again motivated by the boosted topologies which are targeted by the Higgs boson analysis. The rates of these triggers is shown in Figure 5.7. These upgrades have allowed the trigger rate to be reduced from 22.9 kHz for a luminosity of 1.34×10^{34} cm^{-2}s^{-1} in 2015 (L1 trigger with isolation requirement) to 6.7 kHz with the addition of the jet requirement and 5.9 kHz with the addition of the $\Delta R_{\tau\tau}$ requirement. In combination, the jet and $\Delta R_{\tau\tau}$ requirements reduce the trigger rate to 3.8 kHz. Figure 5.8 demonstrates that the $\Delta R_{\tau\tau}$ requirement reduces the rate with no loss of signal events from the analysis, in contrast to the jet requirement. Furthermore, the trigger is fully efficient when a jet of offline transverse momentum greater than 70 GeV and two tau candidates with transverse momenta greater than 35 and 40 GeV respectively as shown in Figure 5.9.

These studies were performed using Z+jets and $H \to \tau\tau$ simulation using PowHeg[74] and the CT10[75] PDF tune to generate the matrix elements and Pythia8[65] with AZNLO[76] and CTEQ6L1[77] to simulate the non-perturbative effects. Final state radiation due to QED is modelled by PHOTOS++[78], EvtGen[79] is used to model the decay of bottom and charm quarks and the tau decays are modelled by TAUOLA[80]. The samples used the standard HLT di-tau trigger with only the L1 input being varied. These are the same samples used in the Higgs boson to di-tau decay present in Chapter 7.

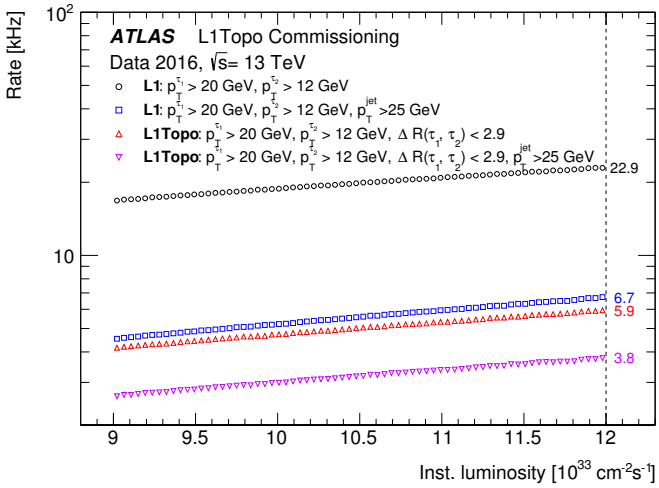

Figure 5.7: Comparison of the L1 rates for a selection of di-tau triggers. The trigger rates are shown as functions of instantaneous luminosity.

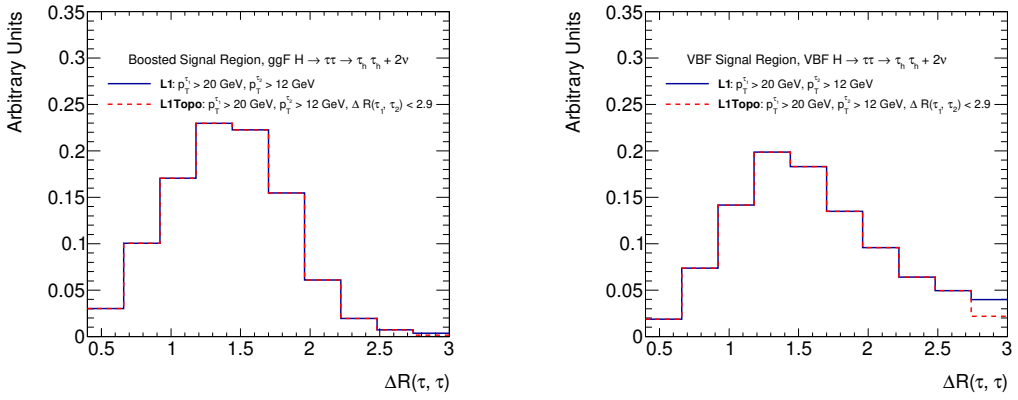

(a) (b)

Figure 5.8: Comparison of event acceptances for the di-tau triggers with and without the L1Topo $\Delta R_{\tau\tau}$ selections in the signal region of the $H \to \tau_h\tau_h + \nu\nu$ signal regions for (a) ggF and (b) VBF. The signal region in both cases corresponds to $\Delta R_{\tau\tau} < 2.4$ as described in Section 7.

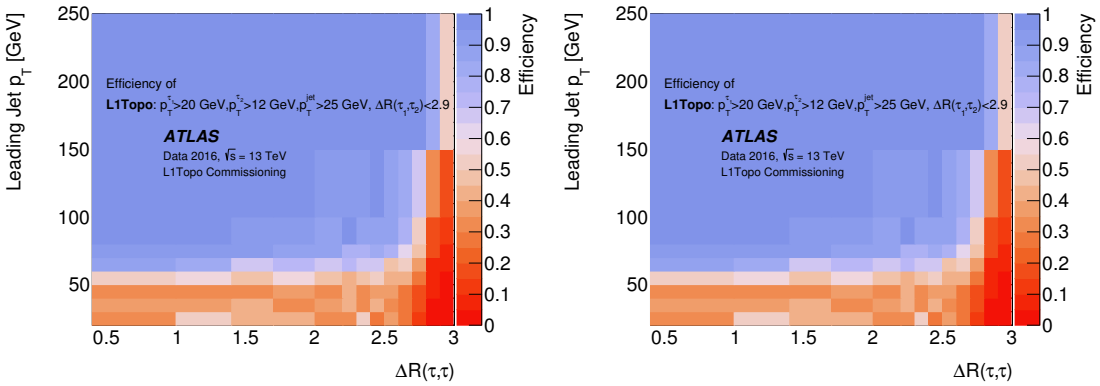

(a) (b)

Figure 5.9: Efficiencies of the di-tau triggers with and without L1Topo $\Delta R_{\tau\tau}$ requirement using ggF $H \to \tau_h\tau_h + \nu\nu$ simulation. The efficiencies are shown with respect to the ditau trigger without topological requirements. No selections are applied except for the presence of two well reconstructed taus.

5.4 Tau Efficiency Measurements

For these results to be useful for physics analyses, the performance and accuracy of these techniques must be verified using data from collisions. It is not possible to define a kinematic region which consists entirely of taus, at most it is possible to define regions which are enriched in taus. An enriched source of taus was created by taking events from resonant Z production. These processes allow the performance to be examined over a wide range of tau p_Ts. This region does tend to be deficient in very high p_T taus but these regions of phase space can be explored using processes like $t\bar{t}$ or W production.

To explore the efficiency of tau production in an unbiased way, it is necessary to avoid placing kinematic requirements on the tau jets being examined. The method chosen to produce this unbiased sample is known as the 'tag-and-probe' method. In this method, the process $Z \to \tau\tau \to \tau_l\tau_h$ is chosen where one tau decays into a light lepton and the other tau decays into hadrons. To avoid the afformentioned bias, an electron or muon trigger is used to select the events. The following efficiency measurements are for the Run 1 tau identification algorithm. Similar measurements were made by others for Run 2.

5.4.1 Event Selection

The $Z \to \tau_l\tau_h$ events are selected by either a muon or electron trigger. These require one isolated electron or muon with a p_T of at least 26 GeV. Additional quality requirements are also placed on the electrons and muons. These leptons are also required to reside within $|\eta| < 2.4$ region. Additionally electrons are required to not reside in the crack between the endcap and barrel calorimeter region which corresponds to $1.37 < |\eta| < 1.52$.

The τ_h is then chosen from amongst the jets in the events. It has the requirement that it has $p_T > 15$ GeV and $|\eta| < 2.5$. The following are also required: one or three tracks in the core region, an integer electric charge, not have any geometrical overlap with a loose or medium electrons and muons with p_T greater than 15 or 4 GeV respectively, and must also satisfy the isolation requirements. One prong taus have the additional requirement that it passes the electron or muon veto. If multiple τ_h candidates are present, only the candidate with the highest p_T is probed. A cut is placed on the BDT score of the tau candidate of 0.4. This value was chosen because no true taus were found below this value.

Muon	$p_T > 26$ GeV etcone/pt < 0.04 nucone40 $= 0$
Electron	$p_T > 26$ GeV ptcone40/et < 0.06 topoetcone20/et < 0.06
Tau	One tau candidate $p_T > 20$ GeV (test $p_T > 15$ GeV) Charge ± 1 Muon and electron veto placed on tau Number of tracks $= 1$ or 3 BDT Score > 0.4 (No real taus below this)
Event Topology	$M_T < 50$ GeV SCDP > -0.4
If muon trigger If electron trigger	$45 < M_{\text{vis}} < 85$ GeV $50 < M_{\text{vis}} < 80$ GeV

Table 5.1: Selections used for the tag-and-probe studies of the tau identification algorithm.

Furthermore, a set of kinematic requirements are used to suppress the other background processes. These are:

- The transverse mass of the light lepton and tau system is required to be less than 50 GeV. This suppresses the contribution of events where a W is produced.
- A variable called sum-cos-delta-phi (SCDP) is used to remove the contribution of W processes. This variable is define as: $\cos(\Delta\phi(\tau_l, \text{MET})) + \sin(\Delta\phi(\tau_h, \text{MET}))$. This variable is required to take a value greater than 0.4.
- A cut is placed on the visible mass of the light lepton and tau system. When the light lepton is a muon, the requirement of $50 < M_{\text{vis}} < 85$ GeV and when the light lepton is an electron, the requirement becomes $50 < M_{\text{vis}} < 80$ GeV. This is used to restrict the event to a window around the Z-peak. This requirement is tightened for events triggered on electrons due to the greater rate at which $Z \to ee$ are able to fake the signal relative to $Z \to \mu\mu$. When examining the low p_T region, ($p_T < 20$ GeV), this requirement is again tightened to $45 < M_{\text{vis}} < 70$ GeV.
- The tau and light lepton are further required to have an opposite charge.

The full set of requirements are summarised in table 5.1.

5.4.2 Background Estimation

Although effort is taken to create a pure sample of taus, contamination from background processes is still present. These must not only be controlled but modelled. The modelling of these processes are divided into what are referred to as charge symmetric and charge asymmetric processes. The key idea is that the charge symmetric processes can be correctly modelled using the same region as the signal region but with the requirement that the tau-lepton pair has the same rather than opposite electric charge. This category of events, referred to henceforth as the 'same-sign' background consists predominately of fake taus where the charge on the tau and charge on the lepton are uncorrelated. The main processes expected to be completely charge symmetric are the processes in which jets fake both the tau and the lepton in the event. For these processes, the shape for a given variable is taken from the same-sign region. The normalisation of the same-sign region is fixed using the region where the BDT Score for the tau candidate is less than 0.3. This region consists almost entirely of same-sign processes with a contribution from processes where a W is produced in association with jets (W+jets) which must be subtracted. Any other process is also subtracted. This normalisation factor, which corresponds to extrapolating from the same sign region to the opposite sign region, is referred to as $\mathrm{R_{QCD}}$.

The largest charge asymmetric background arises from W+jets. The main events in this process consist of a real lepton produced from the decay of the W and a jet generated by either initial or final state radiation faking a tau. These processes are modelled using a data control region generated by requiring that the SCDP variable is inverted to SCDP < -0.6. Data in this region is taken separately for opposite sign and same sign tau-lepton pairs. This background is then normalised to data, again separately for opposite and same sign pairs, in a region consisting of high transverse mass and high missing energy: $E_T^{\mathrm{miss}} > 20GeV$ and $M_T > 60GeV$. The difference between the two distributions, taken as $\mathrm{OS} - \mathrm{R_{QCD}} \times \mathrm{SS}$, is then used to calculate the charge asymmetric component.

Smaller backgrounds which are also present include $Z \to ll$ and processes involving top quarks. These processes are minor and their contribution is taken from simulation.

The $Z \to \tau_l \tau_h$ form the signal of interest. It is for this process that we wish to quantify and

Process	Scattering	Non-Peturbative	PDF[82]
V+jets	Alpgen[83]	Pythia[64]	P2011C
Drell-Yan Z+jets	Alpgen	HERWIG[84]	AUET2CTEQ6L1
di-top with leptons	MC@NLO[85]	HERWIG	CT10
di-top all hadronic	AcerMC[86]	Pythia	AUET2CT10
Single Top (t channel)	AcerMC	Pythia	AUET2BCTEQ6L1
Single Top (s channel)	MC@NLO	HERWIG	AUET2CT10
Di-boson (WW)	Alpgen	HERWIG	AUET2CTEQ6L1
Di-boson (ZV)	HERWIG	HERWIG	AUET2CTEQ6L1

Table 5.2: Simulated samples used in the Tau Identification studies.

mis-modelling present, it is therefore reasonable to use simulation to extract the charge asymmetric component, once again taken to be $\mathrm{OS} - \mathrm{R}_{\mathrm{QCD}} \times \mathrm{SS}$ although the charge same sign component of this process is much smaller than the opposite sign component[81].

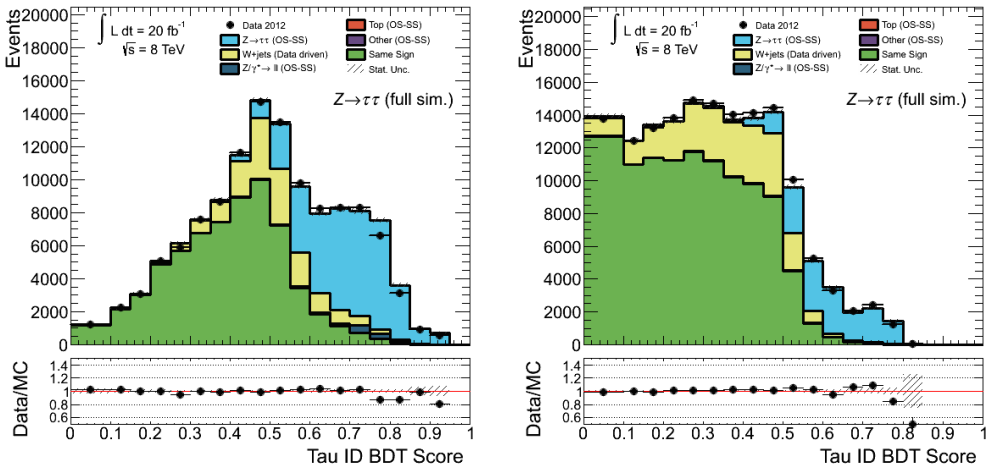

Figure 5.10: The figure shows the BDT spectrum for the probed tau in the tag-and-probe analysis. Figure (a) shows the BDT for single pronged taus, and Figure (b) shows the same for multipronged taus[71]. The background dominated region shows good modelling but the region dominated by real taus modelled by simulation ($Z \to \tau\tau \to \mu\tau$ in blue) shows mis-modelling which must be corrected through the use of scale factor corrections.

5.4.3 Simulated Samples

The simulated samples used in this analysis were generated by the ATLAS collaboration and are summarised in Table 5.2. In addition, all taus decays have been simulated by TAUOLA[80] with QED final state radiation generated by PHOTOS++[78].

5.4.4 Modelling of Kinematic Distributions and Tau Identification Variables

Several variables as well as relevant ones used in tau identification are shown in Figure 5.5 and 5.6. In some cases they are split by up by η region into barrel and endcap. This is motivated by the presence of a different calorimeter and tracking performance in these two regions. Some distributions are also divided into one and three prong because these two taus have separate BDTs trained for each. It can also be reasonably expected that the performance of the tau identification will vary with the transverse momentum of the tau candidate.

Also worth noting is the variation in modelling between low and high amounts of pile-up where pile-up is represented as the number of primary interactions per crossing. The importance of this is that it informs us how well the tau identification algorithm performs at the conditions of higher luminosity expected in future runs.

5.4.5 Calculation of Tau Identification Scale Factors

It can be noted from the previous section, that there is some significant mis-modelling in some of the variables used in the tau identification variables. The modelling of the BDT spectrum, shown in figure 5.10, confirms that this mis-modelling has propagated to the identification algorithm. It is therefore necessary to calculate corrections to compensate for this difference between simulation and data. This correction will be applied to each tau candidate to which a tau identification requirement is applied.

The scale factor is calculated as the ratio of the efficiencies, ϵ:

$$\mathrm{SF} = \frac{\epsilon_{\mathrm{Simulation}}}{\epsilon_{\mathrm{Data}}},$$

where the efficiencies are defined in terms of the fraction number of events, N passing the tau identification requirement:

$$\epsilon = \frac{\mathrm{N}_{\mathrm{Pass\ ID}}}{\mathrm{N}_{\mathrm{No\ ID}}}.$$

Several systematics are placed on these scale factors to account for uncertainties in the detector performance, particle reconstruction and background estimation. The main systematics are:

1. Uncertainty in the normalisation of multijet background,
2. Uncertainty in the normalisation of the W+jets background,
3. Uncertainty in the Tau Energy Scale,
4. Uncertainty in the MET,
5. Uncertainty in the Muon Trigger, Identification and Isolation.

Of these systematics, the largest contributions are from the TES, and the normalisation of the multijet backgrounds.

The set of derived scale-factors are shown in Table 5.3 and Figures 5.11 respectively[81, 87].

Table 5.3: The tau identification scale factors (SF) for each of the working points used in the Run 1.

Tau Identification Working Points		
	1 pronged taus	3 pronged taus
Fails Loose	$0.980 \pm 1.7\% \pm 9.2\%$	$0.976 \pm 2.0\% \pm 1.0\%$
Loose	$1.003 \pm 0.6\% \pm 1.6\%$	$1.008 \pm 1.1\% \pm 3.2\%$
Medium	$0.991 \pm 0.6\% \pm 1.9\%$	$0.999 \pm 1.1\% \pm 3.5\%$
Tight	$0.966 \pm 0.8\% \pm 2.3\%$	$1.007 \pm 1.1\% \pm 4.2\%$
Loose not Medium	$1.072 \pm 2.3\% \pm 1.8\%$	$1.060 \pm 5.2\% \pm 5.9\%$
Medium not Tight	$1.039 \pm 1.5\% \pm 1.7\%$	$1.019 \pm 4.6\% \pm 2.0\%$

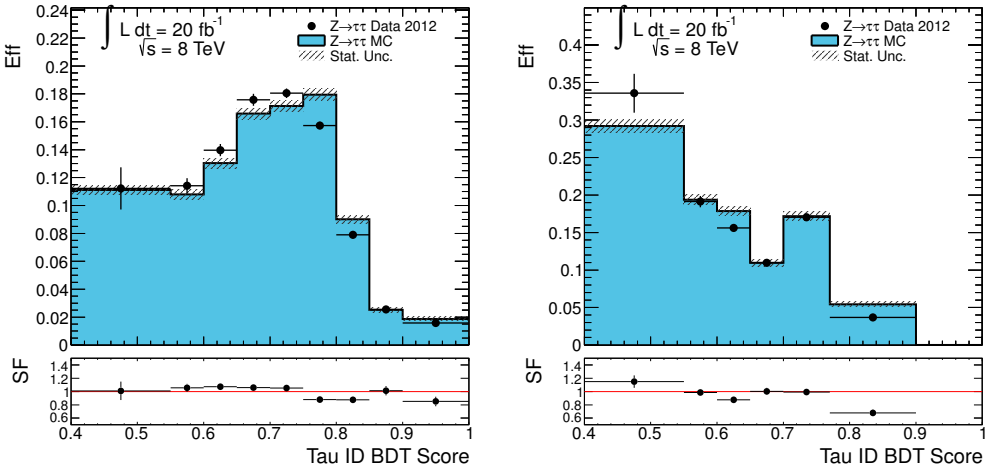

Figure 5.11: The (a) 1p and (b) 3p tau identification efficiencies of data and simulation are shown as functions of the BDT score. The Scale factors are also shown in the lower panel.

Chapter 6

Topological Variables for Hadron Colliders

6.1 Introduction

The complexity of final states being studied at hadron colliders motivates the use of topological variables. The topological variables being used at the LHC were often developed in the context of electron-positron colliders. This is true of the Fox–Wolfram moments (FWMs). The FWMs have been applied in the context of the ATLAS and CMS experiments [88–90] but are not widely used. In contrast, the B-factories, such as Belle and BaBar, use the FWMs extensively to partition phase space [91, 92]. In particular, the FWMs are used in the algorithms to suppress the continuum background [93]. The FWMs partition phase space in a way which is natural for B-factories but not always natural for hadron colliders. The FWMs correspond to a decomposition of the event's phase space into Fourier modes on the surface of a sphere. In the context of hadron colliders, it would be desirable for a harmonic analysis to be invariant under Lorentz boosts parallel to the direction of the beam. Incorporating and evaluating this change will be the subject of this chapter.

6.2 Overview of Fox–Wolfram Moments

The FWMs are defined as [94–96]:

$$H_l = \frac{4\pi}{2l+1} \sum_{m=-l}^{l} \left| \sum_{i=1}^{N} Y_l^m \left(\theta_i, \phi_i\right) \left|\vec{p}_i\right| \right|^2 , \tag{6.1}$$

where Y_l^m are the of spherical harmonics, $\sum_{i=1}^{N}$ is the sum over all reconstructed objects or particles, $\sqrt{s}$ is the centre-of-mass energy of the collision and θ_i, ϕ_i and $\vec{p}_i$ are the i$^{\text{th}}$ object's spherical coordinates and momentum in the event's centre-of-mass frame. The moments can be written in terms of the angular distance between each final state object:

$$H_l = \sum_{i,j=1}^{N} |\vec{p}_i|\,|\vec{p}_j|\,P_l\left(\cos\Omega_{ij}\right), \tag{6.2}$$

using the addition formula for the spherical harmonics:

$$P_l(\cos\Omega_{i,j}) = \frac{4\pi}{2l+1}\sum_{m=-l}^{m=l} Y_l^m(\phi_i,\theta_i)Y_l^{*m}(\phi_j,\theta_j), \tag{6.3}$$

where P_l is the Legendre polynomial of order l and Ω_{ij} is the angular distance between particle i and j. In this form, the invariance under rotation is made manifest as the dependence on the arbitrary axis in equation 6.1 disappears. The moments are typically normalised to the zeroth moment; this corresponds to a uniform rescaling for electron-positron colliders but is more significant in hadron colliders.

Intuitively, the Fox–Wolfram moments describe how compatible the event topology is with each of the spherical harmonics. The utility of the FWMs arises because the moments form an orthogonal basis and are invariant under the set of rotations, $SO(3)$. The rotational symmetry reflects the symmetry of the particle collision in the event's centre-of-mass frame. In effect, this means that any rotation of a given event will not change the moment (up to and excluding detector effects). Similarly, orthogonality removes the redundancy between different moments. When applied correctly, this allows the most important features of an event to be reduced to the lower order moments, with higher order moments describing features of the event dependent on finer resolutions. The FWMs do not contain enough information to reconstruct the energy-density because all information about phases has been removed. They do, however, allow the reconstruction of the energy-density correlation function.

6.3 Limitations of the Fox–Wolfram Moments

In hadron collider experiments, the Fox–Wolfram moments no longer describe the symmetry of the detector and are no longer orthogonal. The limitation of hadron colliders is that the centre-of-mass frame of the event cannot be accurately reconstructed for many processes; particularly processes with final states containing missing energy or where objects are mis-measured jets. In e^+e^- colliders, the centre-of-mass energy of the collision is known and the event can always be boosted from the lab frame into the centre-of-mass frame. By contrast, hadron colliders can only determine the transverse missing energy, so for final states with large missing energy, the event's four-vector sum cannot be reconstructed. The use of FWMs in this context implicitly assumes that the event is produced at rest in the lab-frame. This motivates the creation of a new set of moments that, unlike the Fox–Wolfram moments, are invariant under longitudinal boosts rather than rotations in the polar angle, θ. Both moments are invariant under rotations in the transverse plane. For brevity, the new moments will be referred to as the Hadron Collider Moments (HCMs).

A further weakness of the FWMs is that the orthogonality condition for the spherical harmonics,

$$\int\int_{\Omega} Y_l^m Y_{l'}^{m'*} d\Omega = 4\pi\delta_{ll'}\delta_{mm'}, \tag{6.4}$$

no longer holds because of the incomplete coverage of the detectors. For example, the ATLAS detector's inner tracker has a coverage in rapidity of $|\eta| \lesssim 2.5$, corresponding to $\theta \approx 40°$ missing out of 360°. Over this reduced integral, equation 6.4 becomes:

$$\int\int_{\Omega'_{\text{cut}} \subset \Omega} Y_l^m Y_{l'}^{m'*} d\Omega \neq 4\pi\delta_{ll'}\delta_{mm'}, \tag{6.5}$$

and hence the spherical harmonics no longer form an orthogonal basis. This limitation also applies to experiments where the centre-of-mass frame can be reconstructed. This problem is identical to that faced by the Cosmic Microwave Background (CMB) mapping experiments where the all-sky spectrum is expressed as a Fourier-Legendre series. In CMB experiments, the galactic plane must be excluded (again approximately 40° of 360°). To remedy this, a simple orthogonalisation procedure can be adopted identical to that used by the CMB experiments [97]. This limitation is not present in the HCMs.

6.4 Symmetries of the Lab Frame in Hadron Colliders

The natural symmetries of an event in the centre-of-mass frame is $SO(3)$, or the two rotations of $\mathbb{R}^3$. By contrast, the natural symmetries of an event in the lab frame of a hadron collider experiment is $SO(2)_T \times SO(1,1)_\beta$, where $SO(2)_T$ refers to rotations in the plane transverse to the beam and $SO(1,1)_\beta$ refers to the Lorentz boosts parallel to the beam. This motivates the use of the standard coordinate system of hadron colliders:

$$p = m_T \cosh(y), \quad p_x = p_T \cos\phi, \quad p_y = p_T \sin\phi, \quad p_z = m_T \sinh(y), \tag{6.6}$$

where the rapidity, y, is defined as:

$$y = \frac{1}{2} \log \frac{E+p}{E-p}. \tag{6.7}$$

The rapidity if often approximated by the pseudorapidity:

$$\eta = -\log\left(\tan\frac{\theta}{2}\right), \tag{6.8}$$

which is valid in the limit that the mass of the particles are negligible relative to their energy. At the LHC this is valid for leptons but may not be valid for jets which often have much larger masses. Similarly, the transverse mass, m_T, is often approximated to the transverse momentum, p_T, in this limit. This coordinate system has the advantage that the symmetries of the system are manifest with the invariance of both $\Delta\eta$ and $\Delta\phi$ under longitudinal boosts and rotations about the transverse plane.

It is also useful to define an invariant distance in this coordinate system:

$$\Delta R = \sqrt{\Delta\eta^2 + \Delta\phi^2} = R_1^2 + R_2^2 - 2R_1R_2\cos(\Delta\gamma), \tag{6.9}$$

where $\Delta\gamma$ is the angle between the two radii in η-ϕ space. This contrasts with 6.2 where the distance on a great circle, Ω, is given by:

$$\cos\Omega_{i,j} = \cos(\phi_i)\cos(\phi_j) + \sin(\phi_i)\sin(\phi_j)\cos(\theta_i - \theta_j). \tag{6.10}$$

6.5 Proposed Moments

The FWMs are equivalent to a Fourier series on the surface of a sphere, also known as a Legendre series. Equation 6.9 describes a cone with radius ΔR. In this case, it is necessary to take a Fourier series on the radial component of a cylinder, also known as a Fourier-Bessel series. Together with γ, the polar angle of R in (y, ϕ) space, this forms a set of cylindrical coordinates with the metric:

$$ds^2 = m_T^2 dy^2 + p_T^2 d\phi^2 \approx p_T^2 \left(dR^2 + R^2 d\gamma^2\right) \tag{6.11}$$

The new set of moments can be calculated for the new symmetry by solving the Laplacian for the metric in equation 6.11. Alternatively, the Fourier expansion can be rewritten in terms of γ and R and the moments inferred. This can be seen from the partial wave expansion:

$$e^{-i\vec{k}\cdot\vec{r}} = e^{-ikrsin(\theta)} = \sum_{m=-\infty}^{\infty} J_m\left(kr\right) e^{-im\theta} i^m, \tag{6.12}$$

where J_m is the m^{th} Bessel function. The partial wave expansion can be used to rewrite the Fourier series as:

$$\sum_{n=1}^{\infty} a_n e^{-i\vec{k_n}\cdot\vec{r}} = \sum_{n=1}^{\infty} \sum_{m=-\infty}^{\infty} J_m\left(k_n r\right) e^{-im\theta} i^m \tag{6.13}$$

As with the FWMs, the HCMs describes the Fourier modes of the density correlation function and not the density. Using the equation 6.13, a set of modes can be constructed which are analogous to equation 6.1:

$$S_n = \sum_{m=-\infty}^{\infty} \left| \sum_{i=1}^{N} p_{T,i} J_m\left(k_l R\right) e^{-im\gamma} \right|^2. \tag{6.14}$$

The infinite sum in this equation limits the usefulness of this form. The infinite sum can be removed by applying the addition theorem for Bessel functions,

$$J_0(\Delta R_{1,2}) = \sum_{m=-\infty}^{\infty} J_m\left(R_1\right) J_m\left(R_2\right) e^{-im\Delta\gamma_{1,2}}, \tag{6.15}$$

where $\Delta R_{1,2}^2 = R_1^2 + R_2^2 - 2R_1 R_2 \cos\gamma_{i,j}$. The resulting equation has the dependence on

an arbitrary axis removed and is analogous to equation 6.2:

$$S_n = \sum_{i,j} p_{T,i} p_{T,j} J_0 \left(k_l \Delta R_{i,j} \right). \tag{6.16}$$

The coefficients of this expansion, k_l, are defined by the boundary conditions. Using the Dirichlet boundary condition that the energy-density correlation function becomes zero outside of the detector acceptance region, the coefficients, k_l, corresponds to the l^{th} zero of J_0. For convenience, u_0 is set to zero. The moments are normalised to the zeroth HCM in the same manner as the FWMs. The dependence on the arbitrary axes disappears and the symmetries become manifest. Using these new moments, an event can be expected to give the same value whether they are measured in the lab or centre-of-mass frame.

Information about the particle identifications can be incorporated into both the FWMs and the HCMs by splitting up the summand as follows:

$$\sum_{i,j=all} = \sum_{i,j=\text{jets}} + \sum_{i,j=\text{leptons}} 2 \times \sum_{i=\text{jets},j=\text{leptons}} . \tag{6.17}$$

This allows the moments to be divided into several moments consisting of each of these summands:

$$S_l = S_{l,\text{lepton}\times\text{lepton}} + S_{l,\text{jets}\times\text{jets}} + 2 \times S_{l,\text{leptons}\times\text{jets}}. \tag{6.18}$$

Equation 6.2 is a Fourier-Bessel series which can also be interpreted as the Hankel transform on a discrete interval. The Hankel transform is linked to the Abel transform by the Projection-Slice theorem [98]. In this theorem, the Hankel transform is equivalent to the Abel transform view in Fourier space:

$$\mathscr{F} \cdot \mathscr{A} = \mathscr{H}. \tag{6.19}$$

The Abel transform of a function, $f(r)$, can be written in the following form:

$$\mathscr{A} = \int_{-\infty}^{\infty} f\left(\sqrt{x^2 + y^2}\right) dy. \tag{6.20}$$

This allows the moments to also be interpreted as examining, in Fourier space, the projection of the density correlation function in (η, ϕ) space along parallel lines of constant ϕ.

6.6 Application to Associated Production of $H \to b\bar{b}$

As a simple test of the utility of the HCMs relative to the FWMs, the moments are applied to the all-hadronic final state of the $H \to b\bar{b}$ produced by Higgs-strahlung from a W- or Z-boson. This process was chosen because of the complexity of its final state, and it is a new channel which offers the potential to increase the explored final states of the process $H \to b\bar{b}$ at the LHC. One of the main backgrounds for this signal is the production of $t\bar{t}$ and $t\bar{t}$ + jets. The moments are tested for their discriminating power against this background.

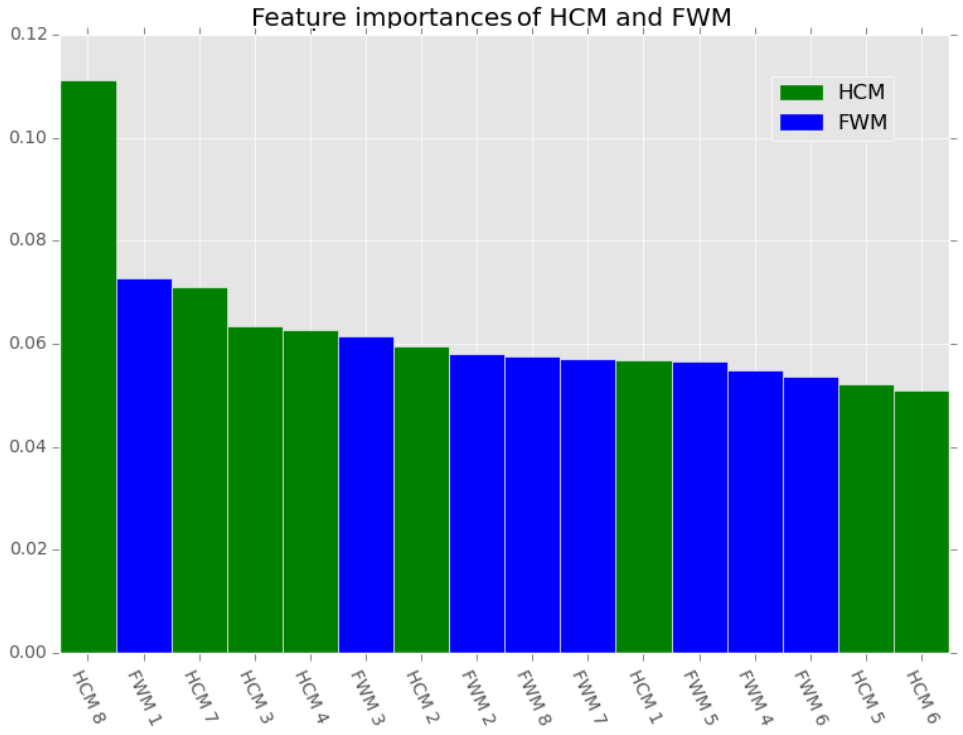

Figure 6.1: The distribution of feature improtance from the random forest when testing the separation of the all-hadronic final state for the signal $H \to b\bar{b}$, produced in association with a W- or Z-boson, from the backgrounds consisting of top quark pair production with additional jets. The distribution of feature importances is shown for the FWMs (blue) and the HCMs (green) with the moments arranged in decreasing importance. The feature importance in each tree is defined as the normalised reduction in node impurity brought by all splits on that feature in the tree. The overall features importance is the average feature importance across all trees. For brevity, only the first eight moments were calculated for both the FWMs and HCMs. The corresponding index for each moment is shown on the x-axis.

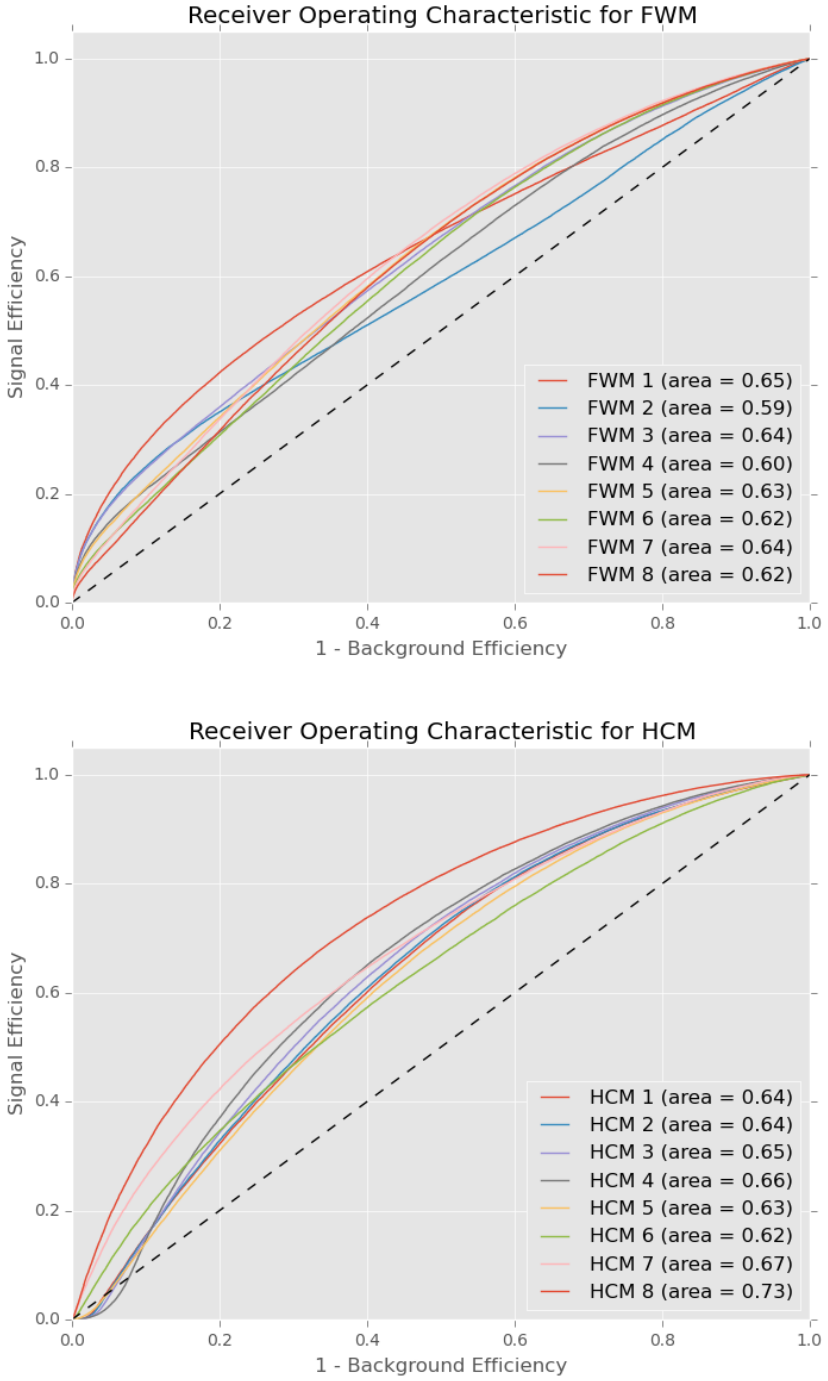

Figure 6.2: The ROC curves and their respective areas for the FWMs (top) and HCMs (bottom) used in testing the separation of the all-hadronic final state for the signal $H \to b\bar{b}$, produced in association with a W- or Z-boson, from the backgrounds consisting of top quark pair production with additional jets.

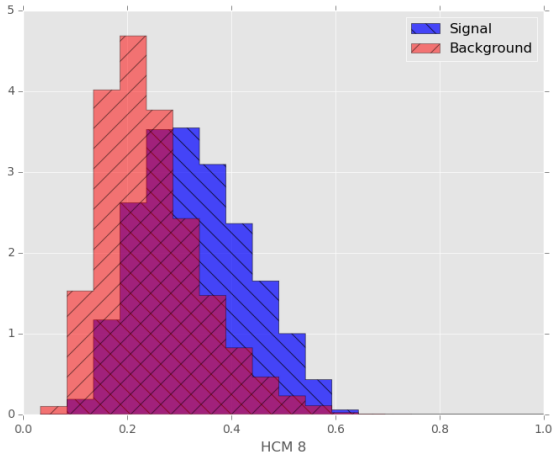

Figure 6.3: The distribution for the eighth order HCM ($l = 8$) for the all-hadronic final state for the signal H $\to$ b$\bar{\text{b}}$ (blue), produced in association with a W- or Z-boson, from the backgrounds consisting of top quark pair production with additional jets (red). This moment was shown to have the most separation of the HCMs (for $l < 8$).

6.6.1 Simulation and Monte-Carlo Generation

The simulated events used to test the new moments are generated using the `MadGraph`[99] and `Pythia8`[65] simulation framework with the ATLAS detector simulated by Delphes [100] with proton-proton collisions at $\sqrt{s} = 13$ TeV. A filter is placed on the jets which corresponds to a 17 GeV cut on jet p_T at the parton level and a 20 GeV cut was used at reconstruction level. The background sample includes up to three additional jets. The final state requires at least two jets which are tagged as coming from the decay of a b-quark.

6.6.2 Quantifying Separation

The separation of these two processes is quantified by the integrated area under the receiver operating characteristic (ROC) curves. In addition to the ROC curves, a simple random forest [101] is constructed to obtain the separation which includes the effect of correlations. A random forest was chosen for this task because it is able to more fully explore the full phase space provided by these variables in a less biased way. At each decision node in the decision tree, the best cut from a random subset of the input variables is performed; by contrast a classic decision tree is usually deterministic. Even when

boosted, a decision tree will tend to look fairly uniform and it will consistently cut on a few dominant moments in the first few decision nodes. This prevents the full phase space of the moments being fully explored.

The feature importance is generated by the random forests and consists of the normalised reduction in node purity brought by all splits on that feature averaged across all trees in the random forest (with the sum of all scores normalised to one) [101]. The distribution of feature importances for the first eight moments of the FWMs and HCMs are shown in Figure 6.1.

6.6.3 Analysis

Figure 6.1 shows greater separation between signal and background when using the HCMs over the FWMs for the first eight moments. The moment which demonstrates the most separation for the HCMs are shown in Figure 6.3 and the feature importance and ROC curves for the HCMs and FWMs are shown in 6.1 and 6.2 respectively. The HCMs, in particular the eighth moment, show consistently better performance and separation than the FWMs. This is reflected by both the random forest's ranking of feature importance and the ROC curves.

The use of the FWMs and the HCMs are not mutually exclusive. Both provide information based on two different limits. The FWMs approximate the final state as being produced at rest while the HCMs assume that the boost is arbitrary. For the very heavy final mass states, the FWMs are expected to improve because heavier mass states are generally very close to rest in the rest frame of the two colliding protons.

6.7 Conclusion

The inability to determine the centre-of-mass frame of the collision in events with missing energy causes the centre-of-mass to only be determinable in the transverse plane. This causes the standard rotational symmetries implicit in the Fox–Wolfram moments to no longer hold. Hence, the same underlying event topology can lead to different Fox–Wolfram moments due to the varying longitudinal boost. To remedy this, a new set of topological

moments are proposed for hadron colliders which reflect the underlying symmetry of the lab frame. The use of HCMs and FWMs is complementary with both moments representing limiting cases. The HCMs can be incorporated into analyses in the same way as the FWMs are; individual moments can be used as cuts or inputs for a multi-variable analysis. Furthermore, these variables will be used for signal extraction in the $H \to \tau\tau$ analysis described in the following chapter.

Chapter 7

Measurement of the Higgs-Tau Yukawa Coupling

7.1 Introduction

Of the final states (or 'channels') which can directly measure a Higgs-lepton Yukawa coupling, the most sensitive is the di-tau decay of the Higgs boson. The di-tau channel has the challenge of large, complex backgrounds some containing multiple jets. Furthermore, the presence of multiple neutrinos in the decay products of the tau leptons limits the resolution of the di-tau invariant mass, limiting its use as a discriminating variable. Evidence of the Higgs-Lepton coupling was found in Run 1 with an observed significance of 4.5σ (3.0σ expected), corresponding to a rate of 1.4 times the SM[4]. This chapter forms the continuation of this measurement using Run 2 data.

As described earlier, the tau lepton can decay via the W-boson into either leptons or hadrons (in addition to neutrinos). The reconstruction of each of these leptonic modes requires very different triggers and object reconstruction which greatly affects the composition of fake and irreducible backgrounds. This motivates the further splitting of the $H \to \tau\tau$ process into different sub-channels based on the composition of the tau decays. The resulting sub-channels with associated branching ratios are[15]:

1. $H \to \tau\tau \to \tau_l\tau_l$, 12%
2. $H \to \tau\tau \to \tau_l\tau_h$, 46%
3. $H \to \tau\tau \to \tau_h\tau_h$, 42%

The $\tau_l\tau_h$ and $\tau_h\tau_h$ sub-channels have the highest branching ratios and have been found to have approximately equal sensitivity[4]. The all hadronic final state ($\tau_h\tau_h$) is the focus of this thesis.

7.2 Analysis Strategy

The processes targeted in this analysis are the production of a Higgs boson through either ggF or VBF. As described in Section 2.3, these two processes have the largest production cross-sections and offer the most promising path to discovery.

The main challenge of performing a measurement in the $\tau_h\tau_h$ channel is the combination of large multijet backgrounds and a large $Z \to \tau\tau$ background. The background from Z decays is considered irreducible because it contains two true taus and its relative contribution cannot be decreased by improved reconstruction techniques. The only way to reduce the relative contribution of the Z background is by targeting different kinematic regions. By contrast, the multijet background consists of processes where multiple jets fake both tau candidates. Typically these processes arise from QCD mediated processes with multi quark final states. Although the tau identification criteria significantly reduces the rate of jets faking taus, the large cross-section for these processes at the LHC means they still constitute a large background. The remaining backgrounds are referred to as 'Others'. These processes are electroweak processes with at least one real tau or electron in the final state. The backgrounds included in this are the production of W+jets, top and dibosons. Examples of these backgrounds are shown in Figures 7.1 and 7.2.

The main method used to suppress background events, especially the Z background, is through the invariant mass of the di-tau system. The method used to reconstruct this variable are discussed in the following section. The preference for on-shell production means that the Z background will be centered around the mass of the Z boson (90 GeV) whereas a Higgs boson would be concentrated around 125 GeV. Typically the fakes background decreases monotonically with the mass of the di-tau system.

The region of phase space that is targeted is the boosted region where the Higgs is produced with a Lorentz boost. This manifests itself as a higher energy and more collimated di-tau system. This significantly reduces the contribution from multijet fakes

as these are typically produced back-to-back with a negligible boost. The boosted topology also favours the production of the Higgs boson over the Z-boson in the ggF channel. As discussed in Section 2.3, the Higgs boson produced via ggF is produced at NLO at a rate comparable to the LO diagram resulting in a high proportion of boosted Higgs boson events with a recoiling jet. The boost of the can be quantified by the angular separation of the tau candidates and the transverse momentum of the di-tau and MET system.

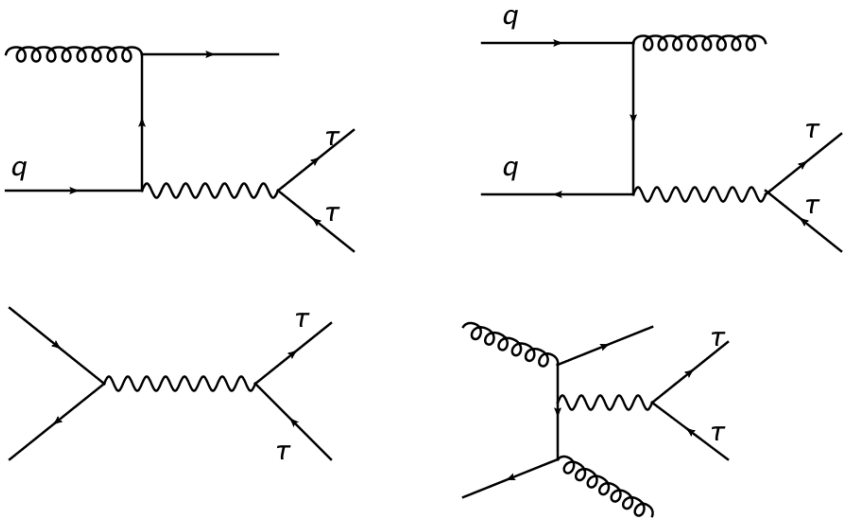

Figure 7.1: Examples of Feynman diagrams for processes expected to contribute to the irreducible Z+jets background for the $\tau_h\tau_h$ channel.

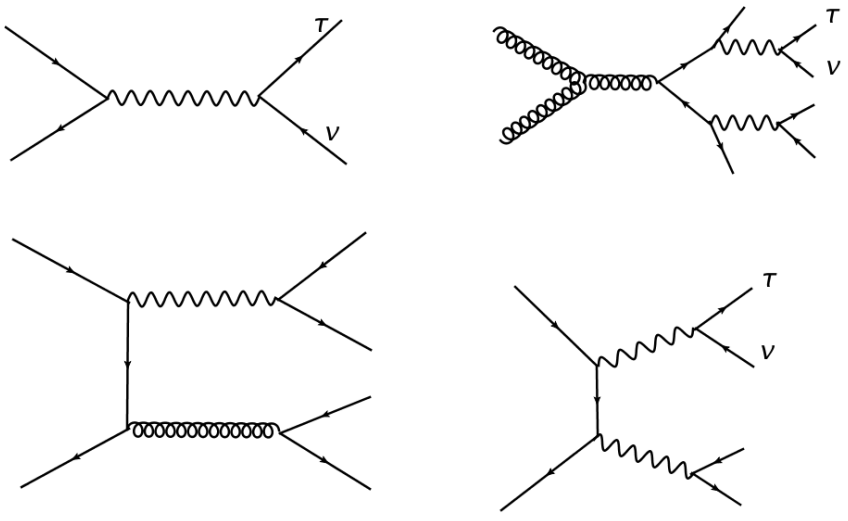

Figure 7.2: Examples of Feynman diagrams for processes expected to contribute to the 'Others' background component which consists of processes containing exactly one prompt tau.

7.3 Higgs Boson Mass Reconstruction

The presence of multiple undetected particles in the final state causes the system of kinematic equations describing the di-tau system to be under constrained. For the $\tau_{\mathrm{h}}\tau_{\mathrm{h}}$ final state, these equations are:

$$
\begin{aligned}
E_x^{\mathrm{Miss}} &= p_{\nu_1} \sin\phi_{\nu_1} \cos\theta_{\nu_1} + p_{\nu_2} \sin\phi_{\nu_2} \cos\theta_{\nu_2}, \\
E_y^{\mathrm{Miss}} &= p_{\nu_1} \sin\phi_{\nu_1} \sin\theta_{\nu_1} + p_{\nu_2} \sin\phi_{\nu_2} \sin\theta_{\nu_2}, \\
m_\tau^2 &= m_{\nu,1}^2 + m_{h_1}^2 + 2\sqrt{p_{\nu_1}^2 + m_{\nu_1}} \cdot \sqrt{p_{h_1}^2 + m_{h_1}^2} - 2p_{\nu_1}p_{h_1} \cos\Delta\Omega_{\nu_1,h_1}, \\
m_\tau^2 &= m_{\nu,2}^2 + m_{h_2}^2 + 2\sqrt{p_{\nu_2}^2 + m_{\nu_2}} \cdot \sqrt{p_{h_2}^2 + m_{h_2}^2} - 2p_{\nu_2}p_{h_2} \cos\Delta\Omega_{\nu_1,h_1},
\end{aligned}
$$

where ν_i refers to the momentum of the i$^{\mathrm{th}}$ neutrino, h_i refers to the visible component of the tau decay, and $\Delta\Omega_{i,j}$ is the angular separation between objects i and j. The final constraint is the experimentally measured mass of the tau, $m_\tau = 1.78$ GeV[15]. This system of equations cannot be solved given that the angles, momentum and mass of the various missing components are not known. The unknown neutrino masses are negligible relative to the centre of mass energy of the collisions and treated as massless. Two approaches are normally taken to resolve this impasse.

The first approach is to assume that the neutrinos are collinear to the tau lepton. This is known as the collinear approximation. This approximation becomes more accurate in the regime where the taus are produced with a large initial momentum.

The second approach uses a likelihood method to infer the missing information. This is known as the Missing Mass Calculator (MMC). The MMC algorithm scans over grid of possible values of $\Delta\Omega_{i,j}$ and calculates the four vectors of the invisible particles. Based on simulation, the four-vectors which best match the missing energy of the detector are chosen. From this the invariant mass of the di-tau system can be estimated. The algorithms are described in more detail in Reference [102].

In the limit that the Higgs boson has a large boost, the neutrinos become collinear to the taus and both algorithms are comparable. In the low boost region, the MMC algorithm is expected to be more accurate. The MMC invariant mass of the di-tau system is used in

the analysis in favour of the collinear mass and forms one of the most important variables used in this analysis.

7.4 Data Samples and Simulation

This section summarises the data and simulation used in the measurement of the $\tau_h\tau_h$ channel.

7.4.1 Data Samples

The data samples used for this analysis were collected by the ATLAS experiment between 2015 and 2016. The data consists of 13.2 fb^{-1} collected from proton-proton collisions at $\sqrt{s} = 13$ TeV. The beam conditions are described in Table 3.1. Of the data collected, only that recorded when the ATLAS detector was fully operational was used[103].

7.4.2 Di-Tau Trigger

The data used in this analysis was collected using a di-tau trigger. During all periods in Run 2, the High Level Trigger (see Section 3.2.3) used was `HLT_tau35_medium1_tracktwo_tau25_medium1_tracktwo`. This trigger requires two isolated hadronically decaying taus passing the online medium tau identification requirement with a p_T greater than 35 and 25 GeV respectively. To avoid any mis-modelling associated with regions of low trigger efficiency, offline cuts of 40 and 30 GeV were placed on the tau transverse momentum.

The main constraint placed on the ditau trigger is at the hardware level of the trigger (L1). At L1, the only useful information available for triggering on taus is the energy deposits in regions of the calorimeters albeit with a reduced granularity. With only this information available, tracking and the tau identification algorithm cannot be used to suppress the large multijet backgrounds. To accommodate the increase in instantaneous luminosity between 2015 and 2016, the L1 selection was changed. In 2015, the `L1_L1TAU20IM_2TAU12IM` selection was used which required two isolated taus with online p_Ts greater than 20 and 12 GeV respectively.

Constraints on the L1 bandwidth resulted in changing to the `L1_TAU20IM_2TAU12IM_J25_2J20_3J12` selection for 2016. This L1 selection corresponds to the previous L1 selection with the addition of a jet with an online p_T greater than 25 GeV. This necessitated the addition of a cut on the transverse momentum of the jet to avoid the turn on curve. The motivation for this using this additional requirement was that the targeted topology for ggF was boosted which typically contains a recoiling jet. Similarly, at least one extra jet is expected from the VBF topology. As shown in Figure 7.3 using simulated Zor$H \to \tau\tau$ events, the requirement that $p_{T,j} > 70$ GeV was sufficient to ensure that the new trigger was fully efficient with respect to 2015. This cut was also applied retroactively to 2015 data to maintain consistency across the different periods.

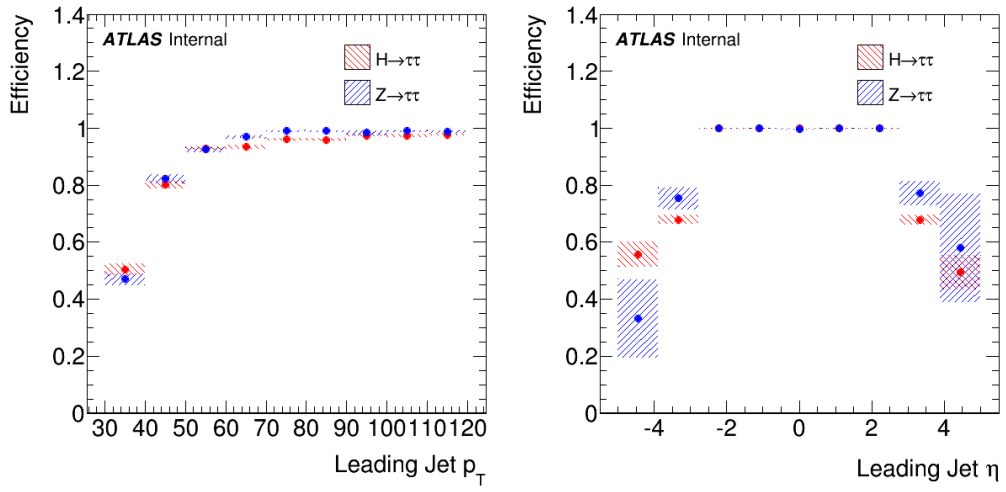

Figure 7.3: Trigger efficiency curves for the L1 selection trigger `L1_TAU20IM_2TAU12IM_J25_2J20_3J12` with respect to `L1_TAU20IM_2TAU12IM` as a function of offline p_T and η for the most energetic reconstructed jet.

7.4.3 Simulated Samples

The simulated samples used in this analysis were generated by the ATLAS collaboration. The detector simulation has been performed using GEANT4[62, 63] before being reconstructed using the same software as data. These samples have been reweighted to match the pile-up conditions in the analysed data along with data-driven corrections to ensure that the performance of the object reconstruction and identification algorithms match those measured in data.

Table 7.1: List of simulated samples and their associated PDFs and event generators. 'V' refers to either a W or Z boson.

Process	MC	PDF
Signal		
ggF $H \to \tau\tau$	Powheg[74, 104–106] + Pythia8[65]	CT10_AZNLOCTEQ6L[76]
VBF $H \to \tau\tau$	Powheg + Pythia8	CT10_AZNLOCTEQ6L
VH $H \to \tau\tau$	Pythia8	A14NNPDF23LO[107]
ttH $H \to \tau\tau$	aMcAtNlo[85, 86] + Pythia8	A14NNPDF23NNPDF30ME[107]
Background		
V+jets (Drell-Yan)	Madgraph[99] + Pythia8	NNLO
V+jets (QCD)	Sherpa 2.2[108]	NNPDF30NNLO[109]
Low mass Drell-Yan	Sherpa 2.1	CT10[75]
V+jets EW	Sherpa 2.1	CT10
Top and Di-Top	Powheg + Pythia[64]	P2012[110]
Di-Boson	Sherpa 2.1	CT10

The samples used to generate the main signal in this analysis (VBF and ggF) are modelled using the `CT10_AZNLOCTEQ6L1` PDF tune with the PowHeg event generator interfaced with Pythia8 for parton showering. The Z+jets background is simulated using Madgraph for hard scattering and Pythia8 for parton showers. As an alternative sample for Z+jets, Sherpa 2.2 with the NNPDF30NNLO PDF tune is used. The decay of tau leptons are modelled using TAUOLA[80] and PHOTOS[78].

A complete summary of the samples used in this analysis can be found in Table 7.1.

7.5 Object Reconstruction

The topology of $H \to \tau\tau \to \tau_h\tau_h$ makes it necessary to reconstruct tau leptons, jets and MET. Any events containing light leptons are vetoed.

7.5.1 Tau Leptons decaying into Hadrons

Exactly two taus are expected from the Higgs boson decays in this channel and hence two taus are required to be reconstructed in each event. Of these taus, both must pass the 'medium' identification requirement (BDT) and at least one must pass the 'tight' requirement[111]. The candidates must have a p_T of at least 40 and 30 GeV which is the p_T range of the trigger acceptance. To reduce the effect of electrons faking taus, the taus

must not overlap within a cone of $\Delta R < 0.4$ of an electron candidate passing the 'tight' identification. The electron identification criteria is chosen such that the tau efficiency is constant at 95% in each region of η and ϕ[112].

A detailed discussion of tau reconstruction is provided in Chapter 5.

7.5.2 Jets

Jets are reconstructed as topological clusters of calorimeter cells using the anti-k_t algorithm with a radius of $R = 0.4$[52]. The jet energy is determined using the electromagnetic scaling scheme. Jets are required to have $p_T > 20$ GeV and be within $|\eta| < 4.5$. Low energy central jets ($p_T < 50$ GeV and $|\eta| < 2.4$) are required to have a $|\text{JVF}| > 0.64$ where JVT refers to the jet vertex tagger algorithm. The JVT requirement is used to select for jets which originate from inelastic proton collisions and can be associated with the primary vertex in the event via tracking information[113].

7.5.3 Other Leptons

Electrons and muons are not present in the $\tau_{\text{h}}\tau_{\text{h}}$ channel but they are used to veto events and in resolving ambiguities from overlapping physics objects.

Muons are reconstructed as tracks in the muon spectrometer and inner detector. Muons are required to pass the 'loose' identification requirement for muons which is based primarily on the number of hits and track quality in the inner detector and muon spectrometer. Muons are required to have $p_T > 10$ GeV and $|\eta| < 2.5$ as well as a graded isolation criteria[114].

Electrons are reconstructed as energy deposits in the calorimeter with associated tracks in the inner detector. Electrons are required to pass a 'loose' identification criteria for electrons and a 'loose' isolation working point. Furthermore, the electron must satisfy $p_T > 15$ GeV and $|\eta| < 2.47$. Electrons occuring within the transition region between the barrel and end-cap calorimeters ($1.37 < |\eta| < 1.52$) are rejected[115, 116].

7.5.4 Missing Energy

The MET definition used in this analysis consists of two components. The first uses the vector sum of the reconstructed jets and taus. The second term, referred to as the 'soft term', incorporates the remaining activity in the detector. The soft term is computed using the TrackSoftTerm (TST) algorithm[117–119] as described in Section 3.2.4.

7.5.5 Overlap Removal

The reconstruction of physics objects that overlap geometrically can create ambiguity as to the correct identity of the object. To address this situation the following criteria is applied:

1. Electrons within $\Delta R = 0.2$ of a muon are excluded.
2. Tau-jets within $\Delta R = 0.2$ of an electron or muon are excluded.
3. Jets within a $\Delta R = 0.4$ cone of an electron or muon are excluded
4. Jets within a $\Delta R = 0.2$ cone of a medium tau are excluded.

The muons used for overlap removal are identical to those above but have a lower threshold of 2 GeV and must pass the 'loose' identification requirements for a muon.

Tau candidates with one core track have the additional criteria that they cannot overlap with an electron candidate ($p_T > 5$ GeV) where the electron identification working point is chosen such that the tau efficiency is a constant 95%.

7.6 Event Selection

Using the physics objects described in the previous section, the set of events analysed is restricted to a sample of events that resemble the signature of the Higgs boson. First a preliminary selection is applied (referred to as preselection) which restricts the events to a set which can be used to analyse the backgound modelling. Subsequent selections target more specific signal topologies. The selections applied are summarised in Table 7.2.

7.6.1 Preselection

To isolate a set of events compatible with the targeted signal, a series of kinematic and topological cuts are applied to each event. Preselection consists of the most preliminary of these selections and provides a large set of events for which the background modelling can be analysed using the object selections of the previous section.

Each event is required to have at least one reconstructed primary vertex from which the two taus are required to originate. Fake jets can arise due many problems including hardware failure, cosmic showers and beam conditions. To suppress the effect of these, all events affected by hardware problems or cosmic showers are rejected[103].

The event is required to contain exactly two taus passing medium identification, at least one of which must also pass the tight identification. The taus are also required to be of unit charge ($|q| = 1$), opposite sign and each tau is required to have one or three tracks. The taus are required to have an angular separation satisfying $0.8 < \Delta R < 2.4$ and $\Delta\eta < 2.0$ which ensures they neither overlap and are consistent with emanating from a boosted intermediate boson. These two taus are also required to be geometrically compatible with the two candidates used by the ditau trigger. To ensure that the trigger is equally efficient in both data and simulation, the taus are required to have a p_T of 40 and 30 GeV respectively. These values were chosen so that the taus are on the 'plateau' of the trigger efficiency curves.

Due to increases in instantaneous luminosity, L1 trigger also required a jet with transverse momentum greater than 25 GeV (online p_T) and an absolute pseudorapidity less than 3.2 was added in 2016. To ensure this trigger is fully efficient, a further requirement of at least one jet with transverse momentum greater than 70 GeV (offline) was applied. This requirement was also applied retroactively to data from 2015 to ensure consistent kinematics across both years, simplifying the analysis.

The events are also required to have transverse missing energy greater than 20 GeV to be consistent with the presence of two neutrinos in our target final state. Furthermore the direction of the transverse missing energy is required to be between the transverse momentum vectors of the taus (in the arc traced out by their minor angle) to be consistent with the neutrinos being approximately collinear with the taus. The low invariant mass

region (corresponding to MMC < 70 GeV) was excluded due to a lack of signal and doubts about the quality of its modelling in simulation.

Any events containing electrons or muons (the lighter leptons) are vetoed as these are not compatible with the signal we are examining. This also ensures that the above selections are formally orthogonal to the selections used in the $H \to \tau\tau \to \tau_l\tau_l$ and $H \to \tau\tau \to \tau_l\tau_h$ analyses.

7.6.2 Boosted Region

This region targets events where the Higgs boson is produced by ggF and where the Higgs is boosted. A boosted Higgs boson is typically produced with a recoiling jet due to considerations of momentum conservation. Events consistent with an unboosted Higgs boson were found to be insensitive to the signal due to the large Z backgrounds in Run 1[4]. This region has been used in the past to aid in normalising the backgrounds used in the main analysis. The addition of the jet requirement to the ditau trigger has caused the unboosted region to become sparsely populated and there is little gain in including these events in the analysis.

To satisfy the Boosted region, an event is required to satisfy preselection in addition to the stricter requirement that the absolute pseudorapidity between the taus is less than 1.5 (due to the taus being produced from a boosted object) and the transverse momentum of the Higgs (defined as the transverse component of the sum of the two tau four-momentums and missing energy vector) must be greater than 100 GeV. This is in addition to the requirement for a jet of $p_T > 70$ GeV.

7.6.3 VBF Region

This region targets events where a Higgs candidate is produced by the VBF process. The topology of this process is typically two taus produced by a boosted Higgs with two high pseudorapidity jets detected in opposite regions of the forward calorimeters. Events are required to satisfy preselection as well as have two additional jets, one with a transverse momentum greater than 70 GeV and the other greater than 30 GeV. The two taus are required to be separated by a pseudorapidity of less than 1.5. The remaining topological

properties are exploited using a multivariate approach described in Section 7.9.

The VBF and boosted regions, as described, can potentially overlap. To prevent this and ensure the regions are orthogonal, the additional requirement is placed on the boosted category that its events fail the VBF category.

Preselection	One medium tau and one tight tau with one tau with $p_T > 40$ GeV and the other with $p_T > 30$ GeV and within $\|\eta\| < 2.5$ Taus have $\|q\| = 1$ and $q_1 \times q_2 = -1$ Taus have one or three prongs At least one jet with $p_T > 70$ GeV and $\|\eta\| < 3.2$ $E_T^{\text{miss}} > 20$ GeV Direction of MET vector between taus' transverse momentum vector $\Delta\eta_{\tau\tau} < 2.0$ $0.8 < \Delta R_{\tau\tau} < 2.4$ MMC > 70 GeV No electrons or muons
VBF	In addition to preselection requirements $\Delta\eta_{\tau\tau} < 1.5$ Additional jet with $p_T > 30$ GeV
Boosted	Fail VBF but pass preselection $\Delta\eta_{\tau\tau} < 1.5$ Reconstruct a Higgs with $p_T > 100$ GeV

Table 7.2: Summary of requirements placed on the preselection, boosted and VBF categories.

7.7 Background Composition and Estimation

The object and event selection requirements are not sufficient to attain a pure sample of $H \to \tau\tau$ events. In this region, the majority of events are produced by other processes. To perform this measurement it is necessary to understand and estimate these backgrounds precisely and impose additional selections to improve the sensitivity of this channel. The backgrounds for this channel are divided into the irreducible and the reducible. The irreducible background consists of all processes with two real taus in the final state as in signal events. By contrast, reducible refers to processses where an object, typically a jet, is mis-reconstructed as a tau. The reducible backgrounds can be further divided into processes with one real tau and processes with no real taus. Each of these classes of backgrounds are estimated differently.

7.7.1 Irreducible Background

The irreducible background consists of processes where a Z boson decays into two taus, $Z \to \tau\tau$. This is referred to as Z+jets. The Z boson may be generated by either QCD processes, as shown in Figure 7.1, or from electroweak processes. The Z bosons produced by the QCD processes are the dominant process but small amounts of electroweak Z production is important in the VBF sub-channel.

Because each object in the final state is not mis-reconstructed, the shape of the irreducible background is modelled using simulation.

7.7.2 Reducible Background: One Real Tau

Processes with exactly one real tau are the smallest of the three background categories. For brevity, it is simply referred to as 'Others'. There are many processes which contribute to this category including the production of di-bosons, top quarks, and processes resulting in the production of a W boson with jets (W+jets). Of these, the W+jets events form the larger background in boosted events whereas top backgrounds dominate in VBF events.

7.7.3 Reducible Background: Two Fake Taus

The least understood of these backgrounds are processes which contain no real taus. These 'Fake' processes are dominated by multijet fakes produced from QCD in which taus are faked by jets. The tau identification significantly reduces their contribution but they still form a major background by virtue of their large production cross-sections at the LHC. There are many difficulties in estimating the contribution of these processes using simulation. Aside from issues of reliability, the low rate at which jets fake taus requires the generation and simulation of extremely large numbers of events of which few pass the object level cuts. The number of simulated events needed to provide a workable sample is impractical. This is compounded by the greater difficulty of simulating mis-reconstructed taus. This necessitates estimating the Fakes contribution from data.

To produce a region enhanced with fakes but which doesn't bias the kinematics of our event, the charge selection is inverted. The requirement that the charge of the two tau

candidates be opposite in sign is inverted to produce a region where the shape of various kinematic variables is thought to be unchanged and the proportion of fake processes enhanced. The implicit assumption in performing this cut is that the charge identification of fake taus is sufficiently poor that both regions are kinematically comparable. To produce an estimate of processes of only fake taus, all not opposite sign (nOS) events from simulation with one or two real taus are subtracted. To allow the proper inversion of the charge requirement, the track requirements are also relaxed permitting any number of tracks. This enables taus to be potentially uncharged.

7.7.4 Normalisation

The shape of the fakes distribution is taken from the nOS data region, the normalisation for this is then taken by performing a fit on the data distribution in the preselection region for the $\Delta\eta\,(\tau,\tau)$ between the taus. The post-fit $\Delta\eta\,(\tau,\tau)$ is shown in Figure 7.4. The fit is performed on events in a $\Delta\eta$ of 0 to 2 separated into 4 bins. In this fit, the normalisation of 'Others' is fixed while the normalisation of Z+jets and Fakes are floated. It is worth noting that the final normalisation for Z+jets is consistent with one, as estimated by simulation. The $\Delta\eta$ variable was chosen for the fit because it shows a reasonable separation of Z+jets and Fakes over the spectrum. In practice, the normalisation does not vary much with the choice of variable and the final normalisation for all processes are re-floated in the signal extraction stage, described in Section 7.11.

A minor complication to this is that the multijet background also contains subtractions taken from Z+jets. To remedy this, the fit is performed iteratively where the normalisation of the subtracted Z+jet events is taken from the previous fit. This process is continued until all values stabilise.

7.7.5 Background Validation

Figures 7.4 and 7.5 show some relevant kinematic distributions at preselection with the background estimates also shown.

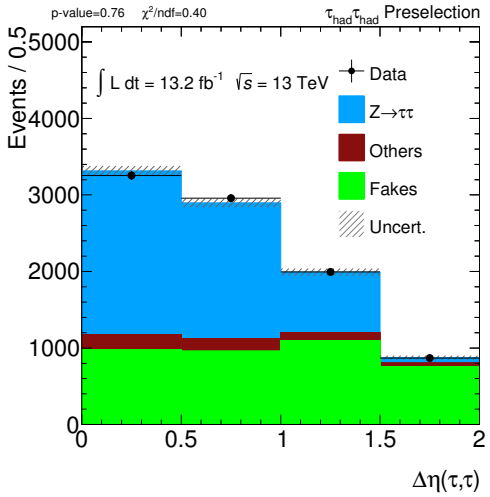

Figure 7.4: The $\Delta\eta_{\tau\tau}$ distribution at preselection used to normalise the background components in the analysis. The distribution is shown post-fit.

7.8 Systematic Uncertainties

In order to validate the quality of our background modelling and the level of confidence in any results we obtain, it is necessary to measure and incorporate any systematic uncertainties. The systematic uncertainties can be divided into experimental and theoretical uncertainties. The experimental systematics consist of any uncertainty that may arise in any calibrations performed, reconstruction algorithms, data-driven background models or the simulation of the detector. The theoretical systematics consist of uncertainties in the production cross-sections, branching ratios and the PDFs arising from any approximations used. The systematics for these are given as ± 1 standard deviation.

7.8.1 Theoretical Systematics

Signal Modelling

The signal samples are normalised to the inclusive cross-section and branching ratio as described by the LHC Higgs Cross-Section Working Group[120]. The uncertainty on the normalisation arises from several sources. These can be divided into uncertainties on the production cross-section, branching ratio, detector acceptance and the underlying event model.

The effect of truncating the QCD perturbative expansions for VH and VBF are estimated by varying the renormalisation and factorisation scales from twice to a half of its nominal value of m_W. For ggF, the uncertainty from this is included by varying the renormalisation and factorisation scales from three times to a third of the nominal value of $\sqrt{m_H^2 + p_T^2}$. This follows the recommendations found in Reference [121]. The uncertainty is also calculated on the contribution from missing diagrams to the EWK component of VH and VBF.

Further systematics arise from the uncertainty in the simulation of the underlying event and the parton showering model. The contribution from this has been quantified by studies comparing different MC generators. To attain an estimate of the uncertainties in the parton distribution functions, the available PDF (CT10) is varied within its uncertainties. The final systematic uncertainty arises from the flat uncertainty on the branching fraction of the Higgs boson to two tau leptons, $0.06256^{+1.17\%}_{-1.16\%}$[122].

Normalisation of Background Components

The Z+jets and Multijet background templates are normalised to data and allowed to float in the final series of likelihood fits are performed. The error associated with these normalisation are found by considering the log-likelihood variation of these values about their best fit values.

7.8.2 Experimental Systematics

The major experimental uncertainties arise from estimating the efficiencies of object reconstruction, identification and triggering as well as the limited resolutions of the various energy scales.

Luminosity

The uncertainty on the integrated luminosity delivered to ATLAS was 2.1% and 3.7% for 2015 and 2016 respectively with an uncertainty on the combined dataset of 2.7%. This has been derived using the procedure described in Section 3.1.2 and in Reference [41].

The uncertainty on the luminosity affects all simulated samples whose normalisation is fixed by the product of their cross-section and luminosity. This is particularly significant for measuring the rate of Higgs boson production.

Pile-Up Reweighting

Due to the computationally demanding nature of generating Monte-Carlo samples, the preparation of these samples must precede data taking. The exact beam conditions, in particular the pile-up distributions, are not known in advance and hence simulation can only approximate this. Once data has been recorded, the simulation is reweighted to match the observed pile-up profile (modelled by the number of interaction points in a bunch crossing) in data.

Tau Reconstruction

The efficiency with which taus are reconstructed, identified and triggered on in simulation is reweighted to match the efficiency observed in data. Uncertainties on these measurements are treated as a systematic. The efficiency measurement has both a systematic uncertainty and a statistical uncertainty. These two sources of error are separate and thus treating independently. The TES systematic is also included and is divided into an in-situ, detector and modelling component. The systematics on tau reconstruction are described in Chapter 5 and in Reference [70].

Jet Reconstruction

The jet energy scale (JES) and resolution (JER) reflect uncertainties in the propagation of calibration and resolution uncertainties. These are quantified using a combination of simulation, test-beam data and in-situ measurements performed with 13 TeV data. The JES is divided into six independent components for light jets. Additional JES uncertainties are included for variations in flavour composition and detector response between gluon and quark initiated jets (extrapolated from 8 TeV to 13 TeV data), the effect of pile-up on the jet energy scale through varying the assumed inelastic cross-section by +16% and -6% and uncertainties in the variation of the calibration across different detector

regions[123–125].

The vertexing algorithm (JVT) is used for jet-vertex association for jets with $p_T < 60$ GeV and $|\eta| < 2.4$. The difference in performance of this algorithm between simulation and data.

MET Scale and Resolution

The transverse missing energy is sensitive to the energy scales of each object and is recalculated for each of these variations. The MET soft term is related to the presence of energy deposits not related to objects and an uncertainty is generated from resolution measurements of the soft terms between simulation and data in $Z \to \mu\mu +$ jets events.

Multijet Background Model

The Multijet background template is taken from a data control region consisting of the inversion of the opposite sign charge requirement on the taus and the loosening of the removal of the track multiplicity requirement. The systematic error in this template is performed by replacing it with the symmetrised and largest difference between !OS events and events with !OS and anti-isolation requirements. The anti-isolation requirements involve the requirement that there are additional tracks within the tau isolation cone of $\Delta R = 0.5$.

7.8.3 Validation of Background Modelling

The number of events observed in each categories along with the predicted signal and background events are described shown in Table 7.3. Note that the VBF and Boosted region are cross-contaminated by ggF and VBF signals.

Process	**Preselection**	**Boosted**	**VBF**
VH	$0.22 \pm 0.04\ ^{+0.03}_{-0.02}$	$0.20 \pm 0.04\ ^{+0.03}_{-0.02}$	$0.020 \pm 0.009\ ^{+0.004}_{-0.012}$
VBF	$21.7 \pm 0.2\ ^{+3.1}_{-2.4}$	$15.9 \pm 0.1\ ^{+2.3}_{-1.7}$	$4.56 \pm 0.07\ ^{+0.65}_{-0.50}$
ggF	$68.1 \pm 1.1\ ^{+9.7}_{-7.4}$	$35.8 \pm 0.8\ ^{+5.1}_{-3.8}$	$23.7 \pm 0.7\ ^{+3.4}_{-2.7}$
ttH	$0.88 \pm 0.03\ ^{+0.12}_{-0.09}$	$0.87 \pm 0.03\ ^{+0.12}_{-0.09}$	$0.0009 \pm 0.0005\ ^{+0.0002}_{-0.0001}$
Total Signal	$90.8 \pm 1.1\ ^{+12.9}_{-9.8}$	$52.8 \pm 0.8\ ^{+7.5}_{-5.6}$	$28.3 \pm 0.7\ ^{+4.0}_{-3.2}$
Z$\rightarrow \tau\tau$	$4697.9 \pm 76.2\ ^{+693.5}_{-538.7}$	$2488.6 \pm 50.2\ ^{+365.6}_{-283.1}$	$1616.3 \pm 48.9\ ^{+236.2}_{-182.2}$
Fakes	$3033.1 \pm 55.7\ ^{+121.4}_{-116.5}$	$1512.5 \pm 39.4\ ^{+62.7}_{-59.4}$	$703.9 \pm 27.8\ ^{+30.3}_{-28.9}$
Others	$471.5 \pm 21.2\ ^{+47.5}_{-36.9}$	$336.2 \pm 13.5\ ^{+36.0}_{-29.0}$	$110.5 \pm 15.3\ ^{+9.1}_{-10.8}$
Total Background	$8202.5 \pm 96.8\ ^{+690.9}_{-538.1}$	$4337.3 \pm 65.2\ ^{+372.2}_{-288.8}$	$2430.7 \pm 58.3\ ^{+229.2}_{-177.2}$
Data	8208.0 ± 90.6	4177.0 ± 64.6	2515.0 ± 50.1

Table 7.3: Event yields with statistical errors for each category used in this analysis. The systematic variations are shown in the sub- and superscripts.

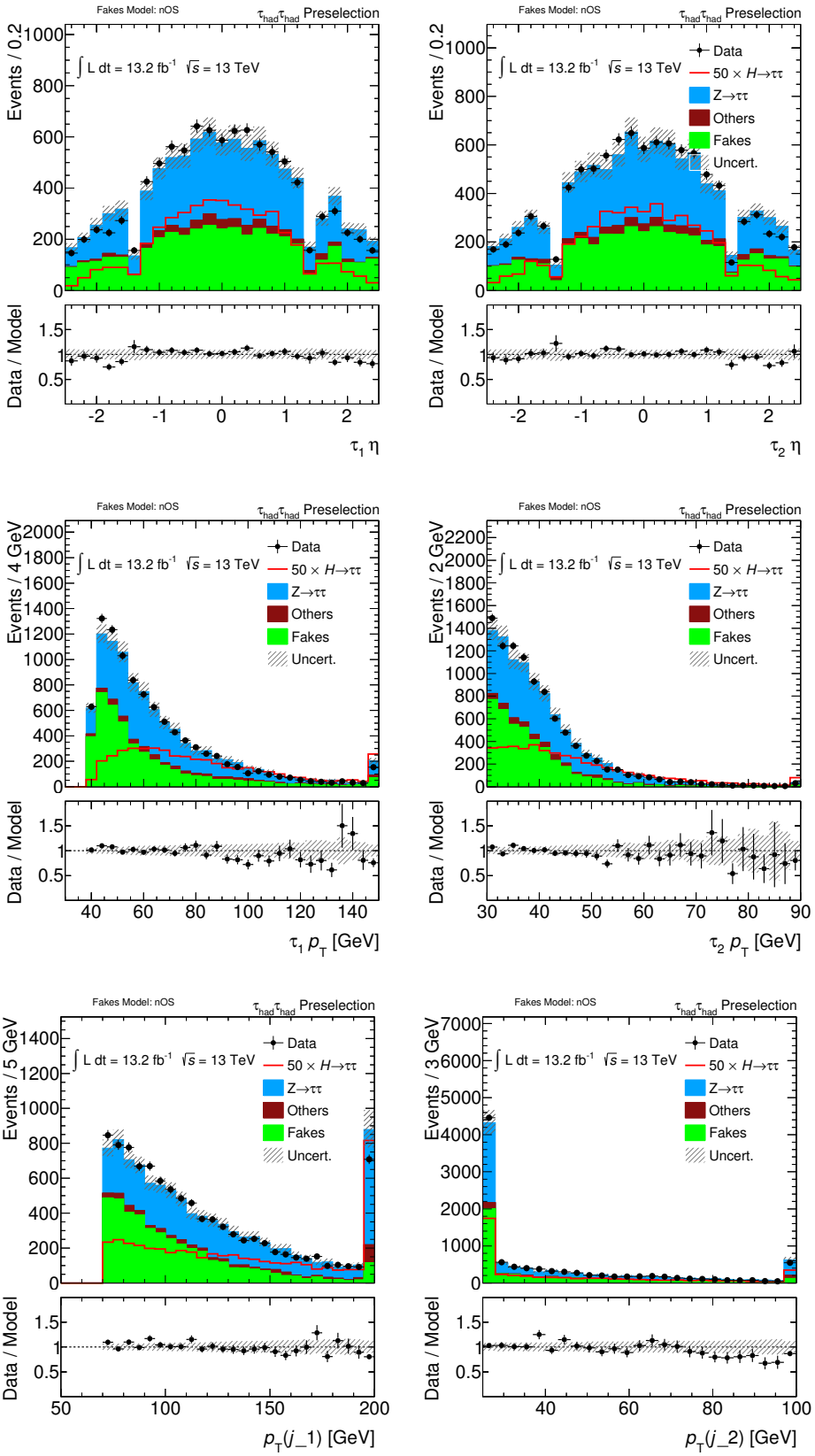

Figure 7.5: Background modelling at preselection for important kinematic variables. Both systematic and statistical errors are included in the uncertainty band.

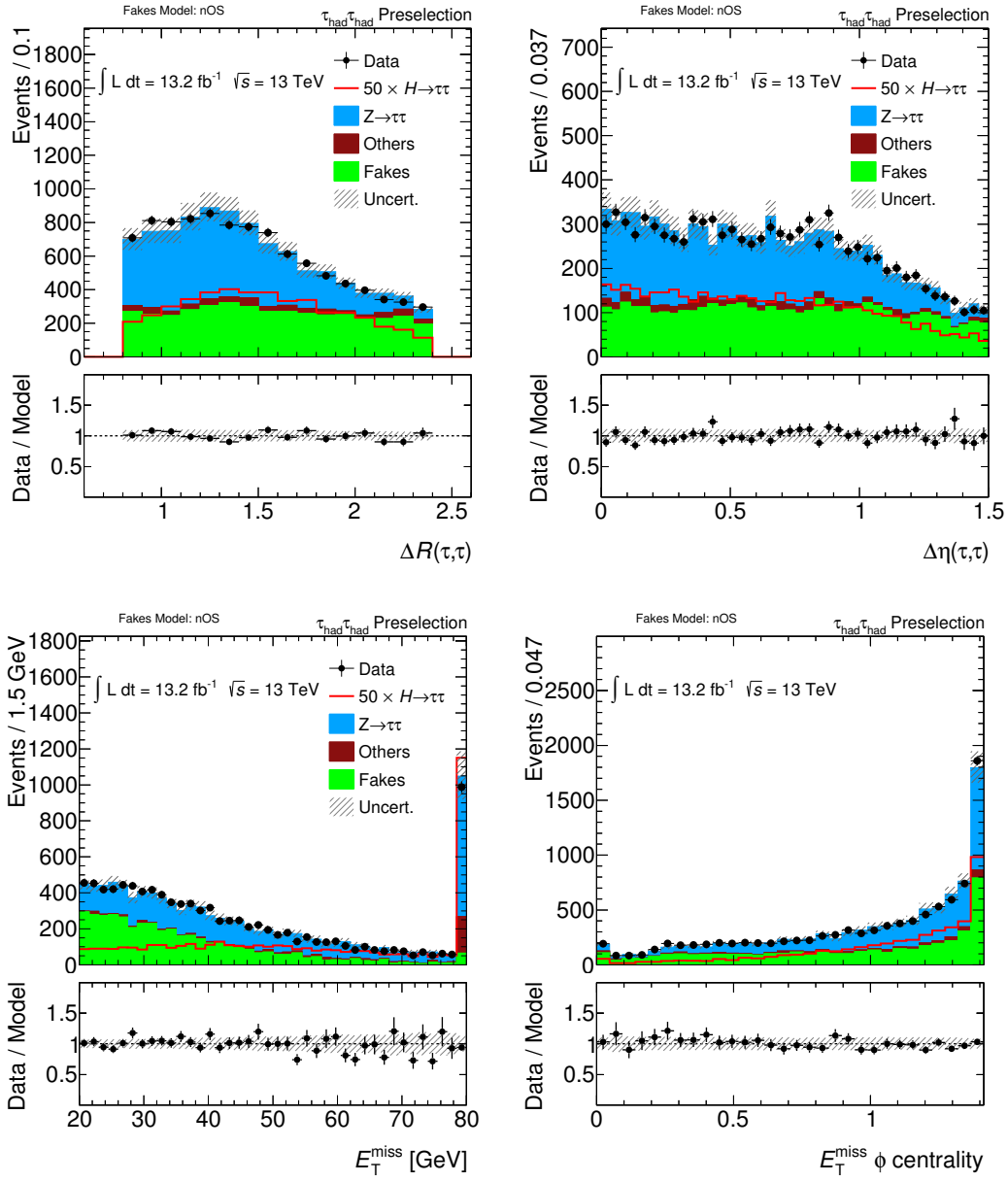
Fakes Model: nOS
$\tau_{had}\tau_{had}$ Preselection
$\int$ L dt = 13.2 fb^{-1} $\sqrt{s}$ = 13 TeV
Data
50 × $H\to\tau\tau$
$Z\to\tau\tau$
Others
Fakes
Uncert.
Events / 0.1
Data / Model
$\Delta R(\tau,\tau)$
Fakes Model: nOS
$\tau_{had}\tau_{had}$ Preselection
$\int$ L dt = 13.2 fb^{-1} $\sqrt{s}$ = 13 TeV
Data
50 × $H\to\tau\tau$
$Z\to\tau\tau$
Others
Fakes
Uncert.
Events / 0.037
Data / Model
$\Delta\eta(\tau,\tau)$
Fakes Model: nOS
$\tau_{had}\tau_{had}$ Preselection
$\int$ L dt = 13.2 fb^{-1} $\sqrt{s}$ = 13 TeV
Data
50 × $H\to\tau\tau$
$Z\to\tau\tau$
Others
Fakes
Uncert.
Events / 1.5 GeV
Data / Model
E_T^{miss} [GeV]
Fakes Model: nOS
$\tau_{had}\tau_{had}$ Preselection
$\int$ L dt = 13.2 fb^{-1} $\sqrt{s}$ = 13 TeV
Events / 0.047
Data / Model
E_T^{miss} ϕ centrality

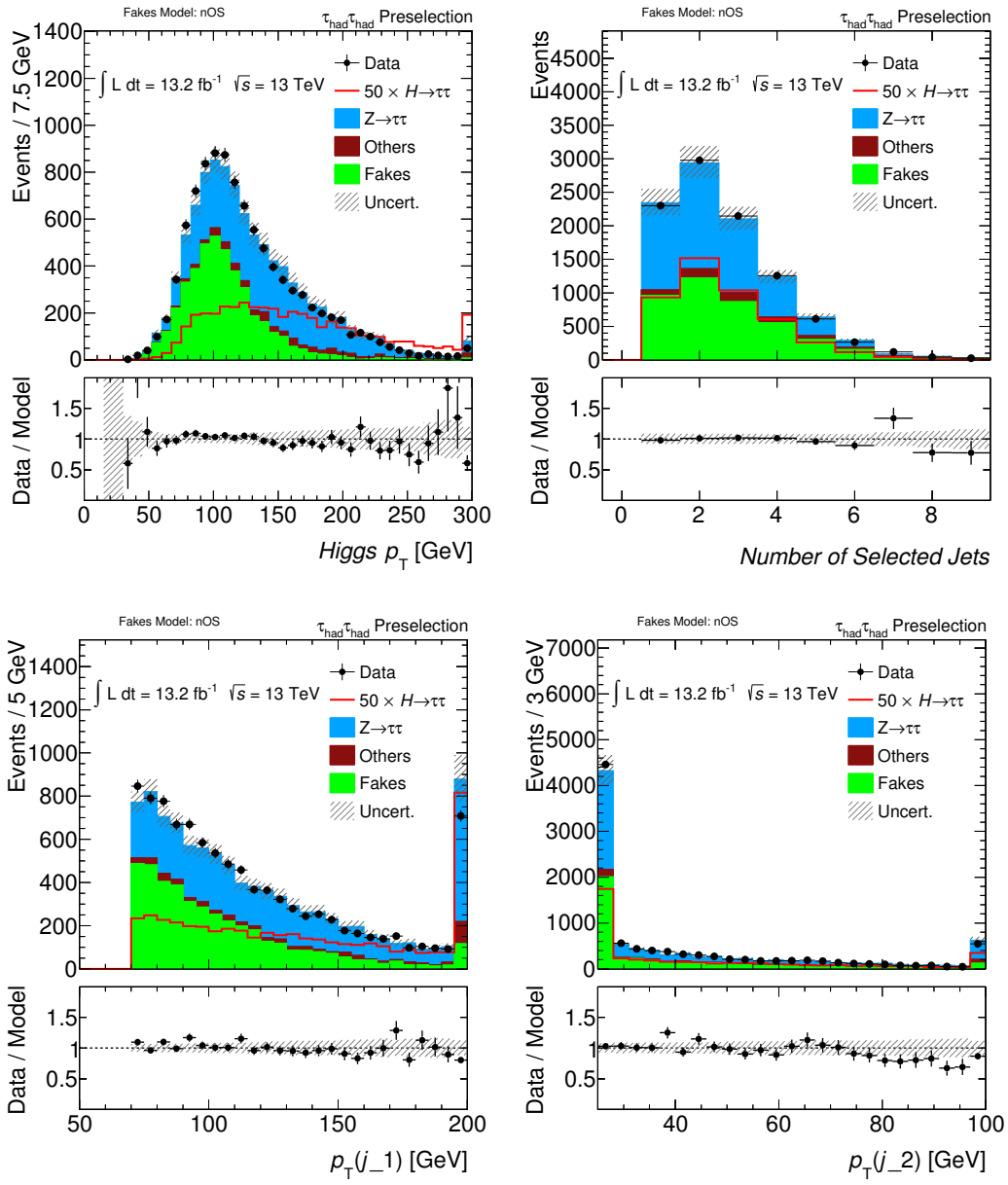

Figure 7.6: This figure shows the modelling and distribution of the variables used to define the boosted and VBF regions. Both systematic and statistical errors are included in the uncertainty band.

7.9 Signal Extraction

To extract an observable signal from the categories defined above, it is necessary to create an additional layer of signal and background separation. The final signal separation attempts to isolate and target regions of phase space where the backgrounds are heavily suppressed relative to the signal.

7.9.1 Boosted Decision Tree Learning

The method used is that of Boosted Decision Tree Learning (BDT). A BDT allows multiple properties of an event to be incorporated with the final output forming a one dimensional spectrum. The BDT is built from many individual decision trees. A decision tree consists of nodes where at each node the most sensitive variable is chosen and the events partitioned around a value of this variable. This process is repeatedly iteratively from a single parent node, which contains all events, until a specified terminating condition is reached[126]. The use of decision trees allows the exploration of more complex regions of phase space while the use of boosting allows the classifier to be less sensitive to issues of overtraining.

The optimal variable and value about which the events are partitioned is determined by minimising the sum of the Gini impurities of the two daughter nodes. This can be summarised as:

$$(i^*, c^*) = \text{argmin}_{i,c}\Big(N_{\text{Signal}}\left(x_i \leq c\right) \cdot N_{\text{Background}}\left(x_i \leq c\right) + N_{\text{Signal}}\left(x_i > c\right) \cdot N_{\text{Background}}\left(x_i > c\right)\Big)$$

for the set of background and signal events with the set of features $\{x_i\}$. A terminating condition must also be specified for the decision tree. The point at which a daughter node is no longer divided is chosen when they contain the daughter node contains less than a minimum number of weighted events.

The limitation of the single decision trees is that they can be unstable under small variations in the training sample. To mitigate this, a 'boosting' procedure is used. This procedure involves training multiple decision trees where each decision tree is trained

and evaluated on the events reweighted to emphasise the misclassified events from the previous trees. The trees are summed with each tree given a coefficient based on their classification rate:

$$\frac{1}{2}\log\frac{N_e}{N_c}. \tag{7.1}$$

The boosting algorithm used is referred to as the Adaptive Boosting (AdaBoost)[127]. AdaBoost reweights each event from the previous iteration by

$$w \leftarrow w \times \left(\frac{N_e}{N_c}\right)^{\pm\alpha\frac{1}{2}}, \tag{7.2}$$

where N_e and N_c are the number of events being correctly or incorrectly tagged and α is the learning rate. To be correctly assigned, a signal (background) event must occur in a terminating node with signal purity greater (less) than 50% to be correctly assigned.

7.9.2 Features

The list of features used in the BDT was constructed using an iterative approach where taking the feature list used in the Run 1 analysis as a starting point. Performance was found to improve by the addition of the HCM variables and the removal of the centrality variables. The aim of each feature is to capture some unique property of an event which can be used to distinguish between background and signal. To ensure that the BDT is well described in data and simulation, only well modelled variables were used in the final feature list. The validation plots for these variables are shown in Figure 7.7 and 7.8.

The final list of variables are shown in Table 7.4 showing the subset used for the boosted and VBF analysis categories. The listed variables target the events total momentum, invariant mass and its topology.

7.9.3 Parameter Optimisation

The three parameters that are not fixed by this BDT prescription are the minimum weighted leaf fraction (terminating condition), the number of trees (depth or complexity of BDT) and the learning rate. The learning rate is closely related to the number of trees and just needs to be fixed to a value small enough to allow the BDT not to overshoot a

Variable	Definition	VBF	Boosted
MMC	The invariant mass of the ditau system with the neutrino momenta estimated using a likelihood method	●	●
$\Delta R_{\tau\tau}$	The angular separation of the two taus.	●	●
$\frac{p_T(\tau_1)}{p_T(\tau_2)}$	The ratio of the transverse momentum of the taus where the leading tau in the denominator and the subleading tau in the numerator.		●
Σp_T	The scalar sum of the transverse momentum of the taus and jets.		●
$\left\lvert p_T^{\text{Total}} \right\rvert$	The absolute value of the vector sum of the transverse momentum vectors of the two taus, two jets and missing energy.	●	
m_{jj}	The invariant mass of the di-jet system.	●	
$\Delta\eta_{jj}$	The separation in pseudorapidity of the two jets.	●	
HCM 3	The third hadron collider moment as described in Chapter 6.	●	
HCM 5	The fifth hadron collider moment as described in Chapter 6.		●

Table 7.4: Features used in the training of the VBF and Boosted BDTs

global minimum. The remaining two parameters are determined by scanning a grid of these values and using the values for which the separation is maximised on the testing data. The separation is quantified by the area under the receiver operating characteristic (ROC). The ROC corresponds to a plot of the signal efficiency versus the inverse background efficiency. A Five-Fold method was used. In this method the training sample is divided into five approximately equal parts. The performance of the BDT is taken from the average of the performance of the BDT on each of the five samples using the remaining four in each case as training samples.

7.10 Statistical Methods

The statistical procedure used to extract information from the relevant distributions is based on the recommendations by the LHC Higgs Combination Group and described in Reference [121]. The procedure used here is to construct a binned likelihood function as a function of the signal strength modifier. The signal strength modifier (μ) corresponds to a scaling factor for the observed number of Higgs boson events where no observed excess corresponds to $\mu = 0$ and observation consistent with a Standard Model cross-section

corresponds to $\mu = 1$. This distribution is also subject to the effect of various systematics, referred to as nuisance parameters. The general form of this likelihood function ($\mathscr{L}$) is

$$\mathscr{L}\left(\text{data}|\mu,\theta\right) = \text{Poisson}\left(\text{data}|\mu\cdot s\left(\theta\right)+b\left(\theta\right)\right)\cdot p\left(\widetilde{\theta}|\theta\right), \tag{7.3}$$

where the likelihood of observice a distribution of data is expressed as a function of the expected signal (s), background (b) and the value of the nuisance parameters (θ) and the expected value for this nuisance parameter ($\widetilde{\theta}$) given the expected probability distribution, p, of the nuisance parameters. The probability distribution of nuisance parameters is typically constructed as the product of the probability function of each nuisance parameter where the individual nuisance parameters are constructed as either Gaussian or log-normal probability distributions. For a binned fit, as is performed in this analysis, Poisson error becomes:

$$\text{Poisson}\left(\text{data}|\mu,\theta\right) = \Pi_i \frac{\left(\mu\cdot s_i + b_i\right)^{n_i}}{n_i}\exp(-\mu\cdot s_i - b_i), \tag{7.4}$$

where n_i is the number of observed events in bin i. In this way, the above approach is frequentist but with Bayesian priors for the nuisance parameters.

The significance of the signal hypothesis is explored by determining the probability that the observed or larger excess can be produced by the background only hypothesis. To examine this, a test-statistic is constructed as:

$$q_0 = -2\log\frac{\mathscr{L}\left(\text{data}|\mu=0,\theta_0\right)}{\mathscr{L}\left(\text{data}|\hat{\mu},\theta_{\hat{\mu}}\right)}, \tag{7.5}$$

where θ_μ refers to for a nuisance parameter which maximises the likelihood for a given signal strength. By scanning all possible values of the nuisance parameters within their best fit value, it is possible to form the probability distribution, $P\left(q_0\right) = f\left(q_0|\mu=0,\theta_0\right)$ where the data is replaced by the the background only hypothesis, $b(\theta_0)$. The significance of any excess can then be quantified as $P\left(q_0 > q_0^{\text{obs}}\right)$. Expected limits can also be generated in this way by determining the value $P\left(q_0 > q_{\mu=1}\right)$. In addition, the likelihood function can also be used to generate the best fit value for the signal strength, μ.

The systematic error associated with any individual nuisance parameter, referred to as the 'pull', can be obtained by generating the above probability distribution where a single

nuisance parameter is fixed and scanned over. The systematic then corresponds to the $\pm 1\sigma$ about the best fit value.

The hypothesis being tested in this thesis considers the compatibility of the observed Higgs boson (with mass 125 GeV) with the Standard Model formulation of fermion mass generation. As such, no scan over mass values is performed and no alternative hypotheses are considered. This allows the corrections from the diluting effect of scanning multiple hypotheses to be disregarded (often referred to as the 'look-elsewhere effect').

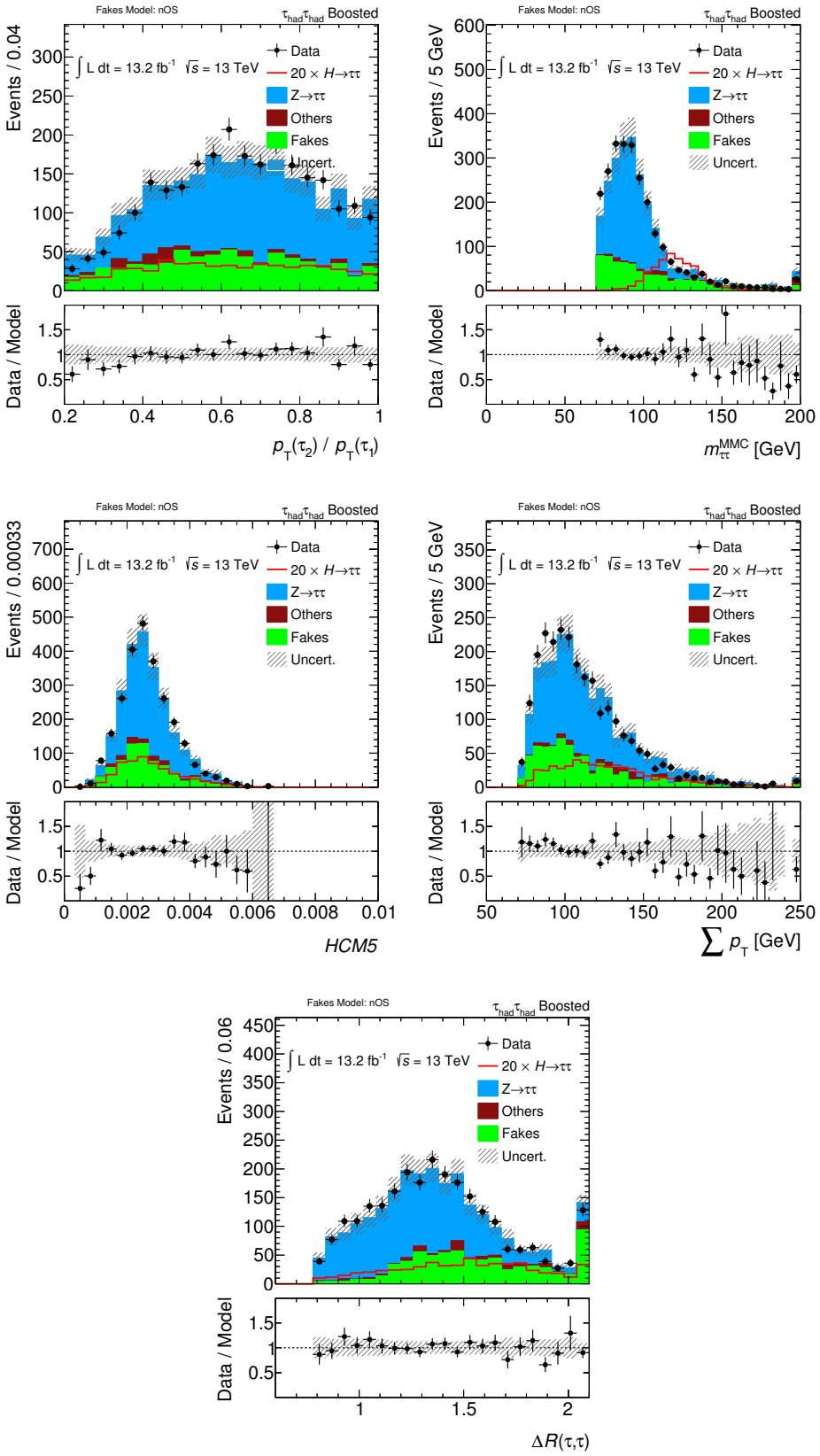

Figure 7.7: This figure shows the background modelling of the variables used to train the Boosted BDT. The variables are plotted in the boosted region with both statistical and systematic errors included in the uncertainty bands.

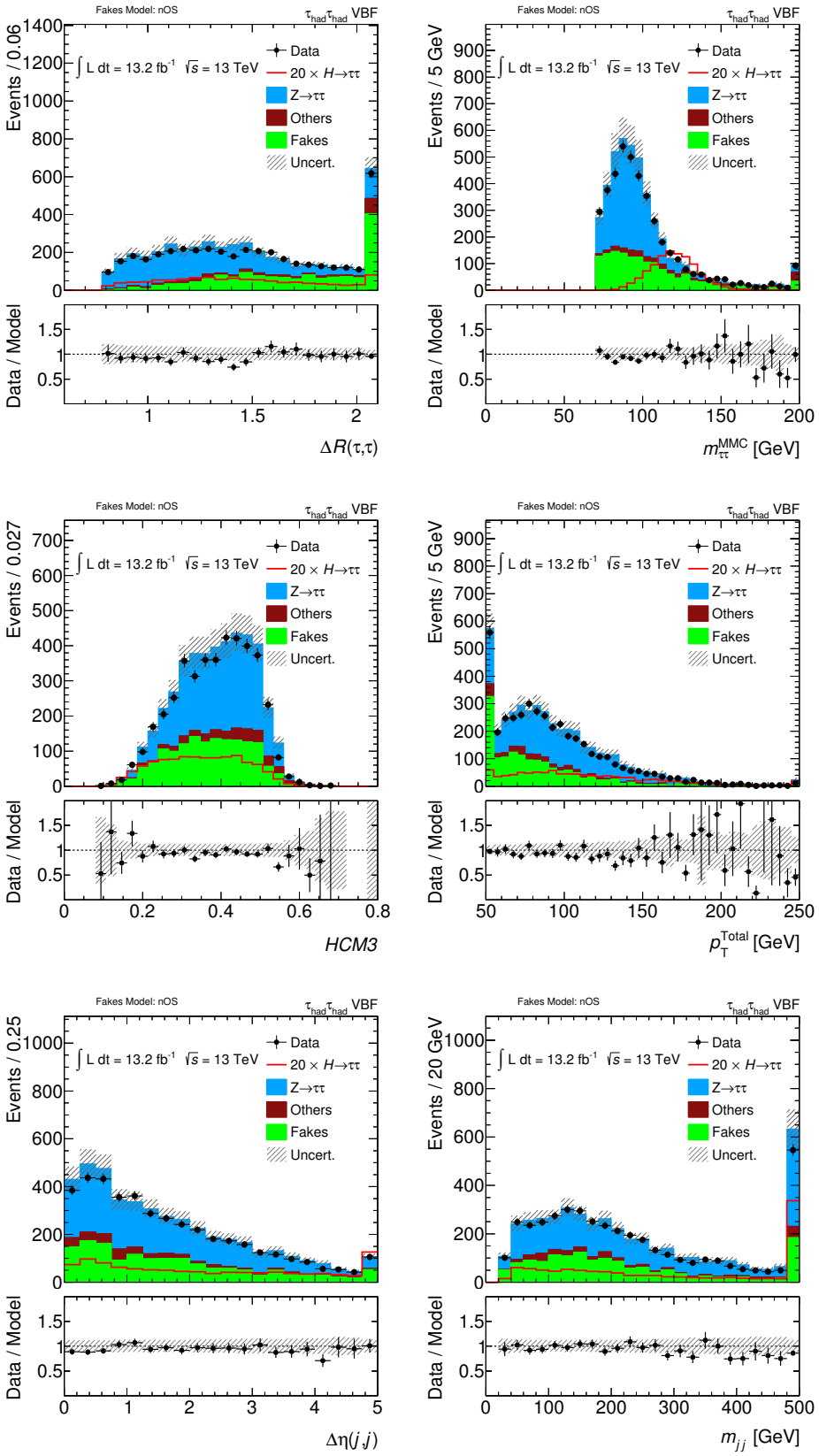

Figure 7.8: This figure shows the background modelling of the variables used to train the VBF BDT. The variables are plotted in the boosted region with both statistical and systematic errors included in the uncertainty bands.

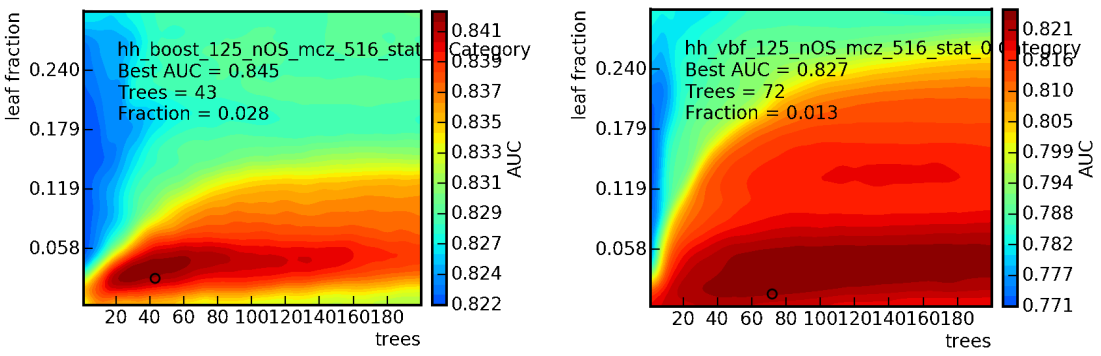

Figure 7.9: Parameters optimisation through a grid scan for the MVA trained for the VBF and Boosted signal regions. The parameters scanned over are the number of trees in the ensemble and the weighted fraction of events in the terminating leaf node.

7.11 Results

Using the statistical framework described in Section 7.10, a fit was performed on the BDT inputs. A best fit value was calculated along with the associated errors using `Minuit` and `MINOS`[128]. The overall results is shown in Table 7.5. In this fit, the normalisations and nuisance parameters were shared across the VBF and boosted categories. A small excess was observed which is still consistent with the Standard Model to within one standard deviation but represents an over fluctuation. This is consistent with what was seen in Run 1 where a similar over fluctuation in this channel was observed. The BDT distributions post fit are plotted in Figures 7.10 and 7.11 with a signal strength of 1.72 times the Standard Model expectation (best fit value).

Fit Results for $H \to \tau\tau \to \tau_{\mathrm{h}}\tau_{\mathrm{h}}$	
Best Fit μ	1.72 ± 0.90
Expected Significance	1.30σ
Observed Significance	2.12σ

Table 7.5: Best fit values from performing the likelihood fit to the BDT scores for the process $H \to \tau\tau \to \tau_{\mathrm{h}}\tau_{\mathrm{h}}$.

The non-negligible nuisance parameters considered in this analysis and their best fit values and ranges are shown in Figure 7.12. All values are consistent within one standard deviation of the nominal values provided by the combined performance groups. The only nuisance parameter for which an over-constraint is observed is the analysis specific background shape for fakes. This is not unexpected as the variation for this systematic has no expected range as the normalisation isn't fixed for each alternative distribution. Likelihood scans of all the nuisance parameters were performed and all show a clear minimum with a Gaussian like shape as desired.

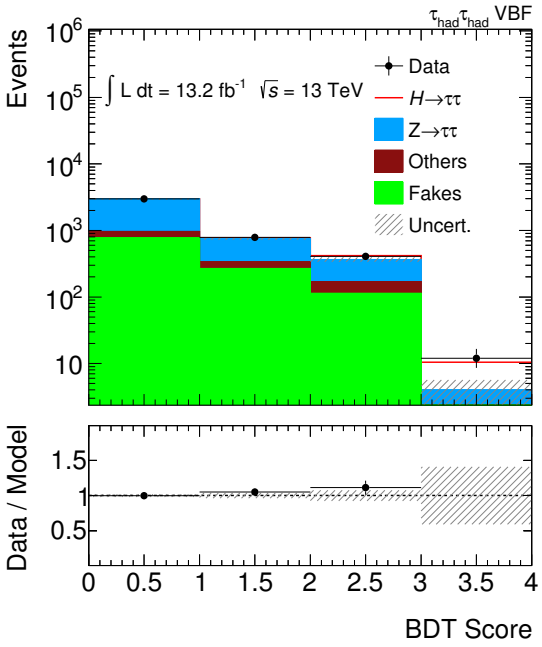

Figure 7.10: The post fit distributions for the VBF category are shown with a logarithmic scale on the y-axis. The rightmost bin corresponds to the most sensitive bin in the analysis.

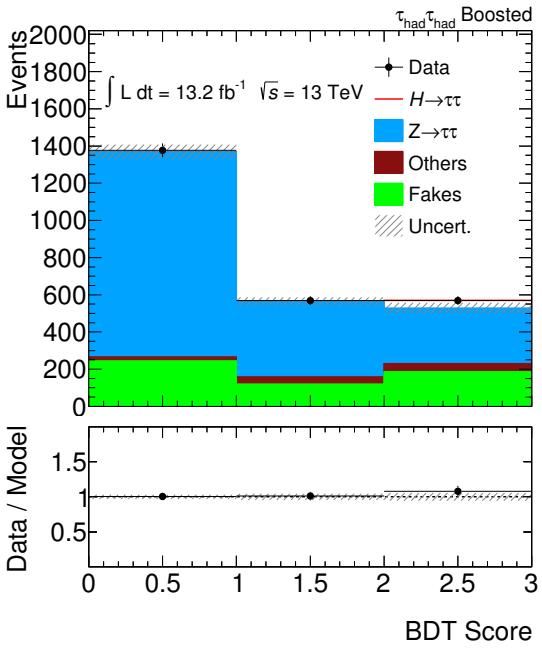

Figure 7.11: The post fit distribution for the boosted category is shown. The rightmost bin corresponds to the most sensitive bin in this category.

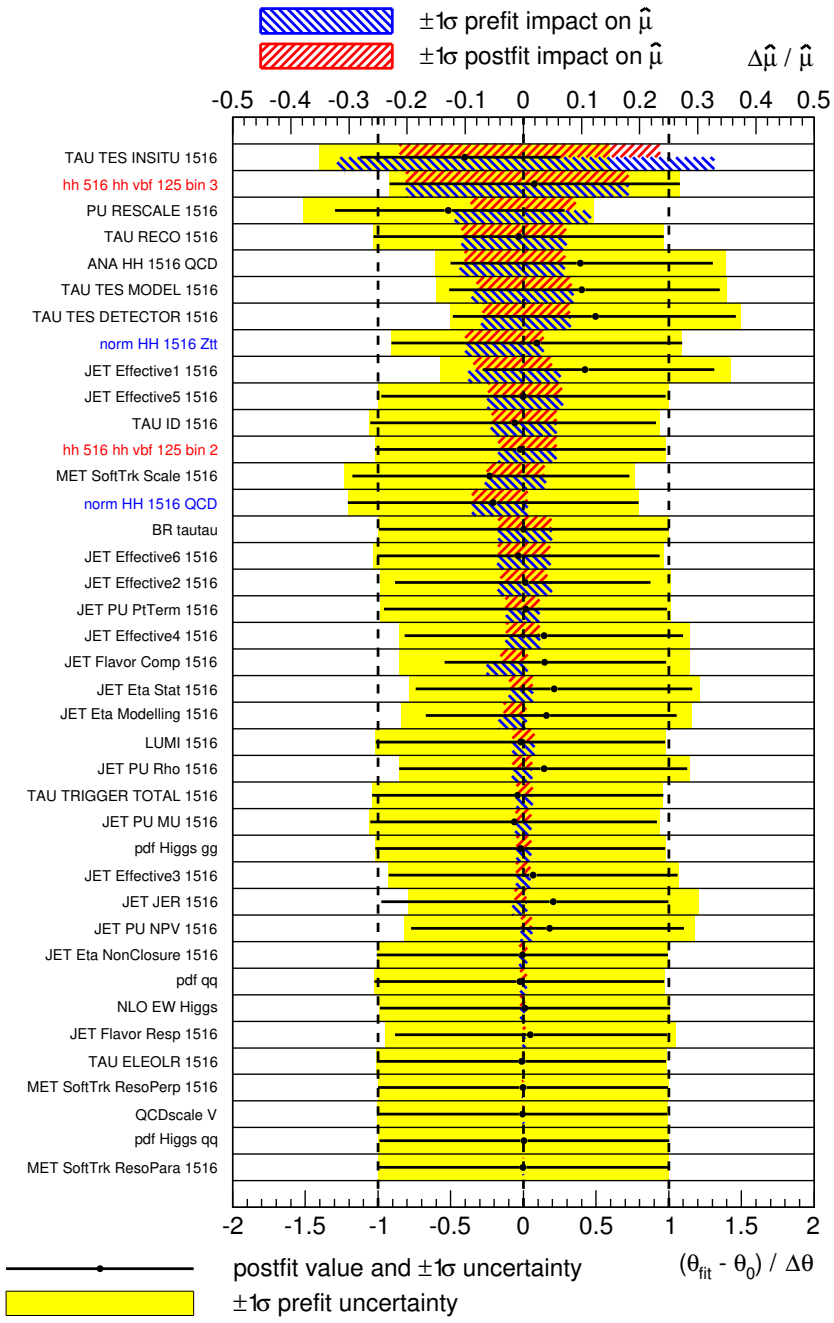

Figure 7.12: The set of non-negligible nuisance parameters and their nominal and best fit values are shown. The hashed region in red (blue) corresponds to the post fit (pre fit) impact on the signal strength (μ). The nuisance parameters (black points with error bars) are plotted as the deviation from the central pre-fit value divided by the size of one standard deviation. The text is shown in black for systematics, blue for normalisation factors and red for statistical uncertainties.

7.12 Combined Measurements of Higgs-Tau Yukawa Coupling

As yet, no results have been released by ATLAS using data from Run 2 for the Higgs boson to di-fermion decay. Results were released using data collected during Run 1. In the Run 1 analysis, described in Reference [4], an excess consistent with the Standard Model was observed with 4.5 σ across all tau lepton decay channels ($\tau_{\text{lep}}\tau_{\text{lep}}$, $\tau_{\text{lep}}\tau_{\text{had}}$ and $\tau_{\text{had}}\tau_{\text{had}}$). The best fit value of the signal strength (μ) was found to be 1.4 times the Standard Model prediction. This was however still consistent with a signal strength of one too within one standard deviation. These results are summarised in Figure 7.14.

The comparison with the $H \to \tau\tau \to \tau_{\text{h}}\tau_{\text{h}}$ is also meaningful. The equivalent postfit distributions are shown in Figure 7.13. In Run 1, the observed significance was 1.99 σ. By comparison, Run 2 data gives a significance of 2.12 σ. Both analyses saw an excess with Run 1 channel measuring a signal strength of 2.0 times the Standard Model and the Run 2 channel measuring a signal strength of 1.72 times the Standard Model. Comparable fits performed on the boosted and vbf categories in Run 1 are shown in Figure 7.13.

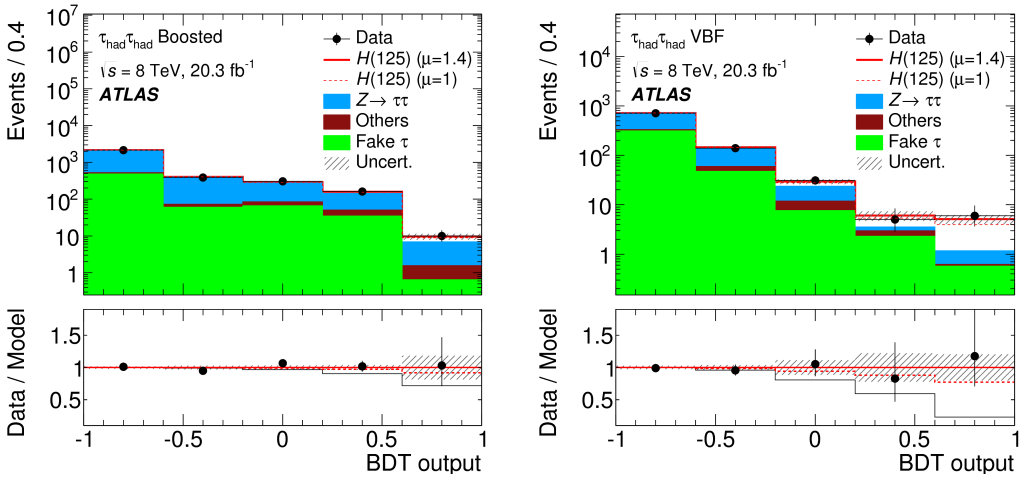

Figure 7.13: This figure shows the BDT distributions used in the Run 1 $H \to \tau_h\tau_h$ analysis plotted with using the best fit value for the signal strength, $\mu = 1.40$,

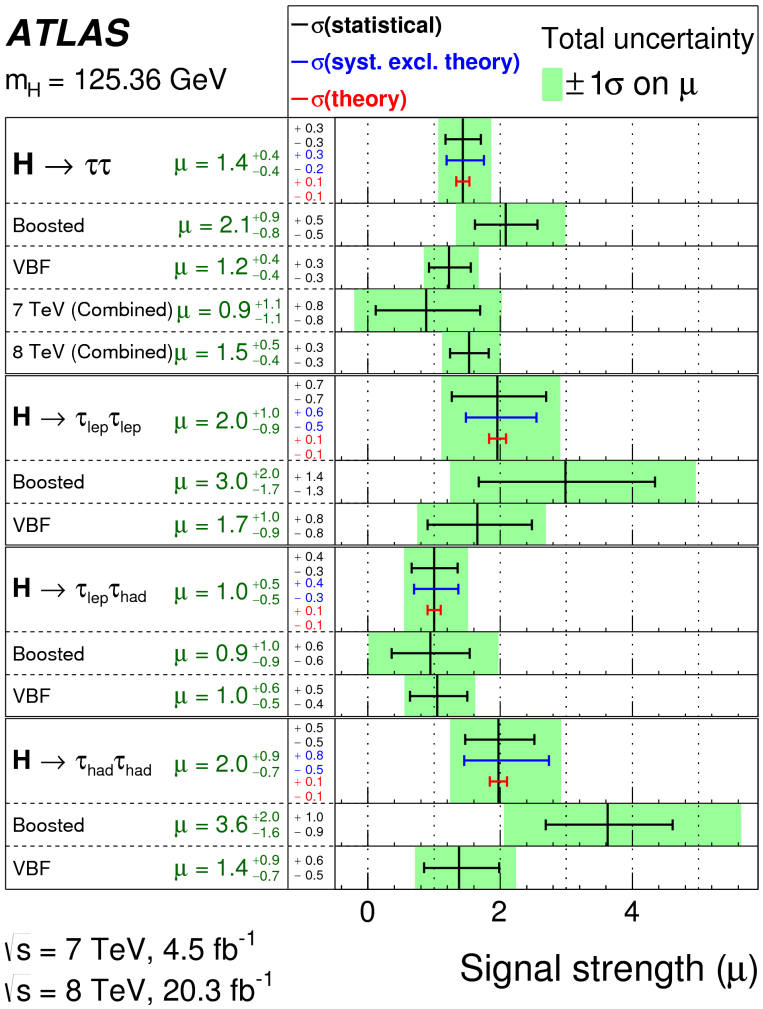

Figure 7.14: This figure shows the ATLAS results using just run 1 data across all tau-lepton decay modes.

Chapter 8

Limits on the Higgs-Muon Yukawa Coupling

A property of the SM is that the third generation of matter is separated by a large mass gap from the second and first generation. As a result, their branching ratio to the Higgs boson becomes small and many of these modes become less accessible experimentally.

The di-muon Higgs boson decay is the only process that can be studied at the LHC which can experimentally probe the Higgs boson's coupling to non-third generation fermions. The muon has a lower mass than the charm quark but compensates for this by having a very clean and well understood background and signal. The di-muon decay provides excellent resolution for the mass of the Higgs boson. Current limits on the Higgs boson's decay width are approximately 20 MeV[29] meaning that the Higgs boson mass measurement is only limited by the resolution of the detector which is, by comparison, approximately 3 GeV in the most sensitive portion of the detector. Opportunities also exist, when combined with the Higgs-Tau Yukawa coupling, to place strong constraints on flavour physics and lepton universality[129].

8.1 Analysis Strategy

The final state targeted by this analysis are two oppositely charged muons and low amounts of missing energy. The main background to this process is $Z \to \mu\mu$. Projecting this onto the di-muon invariant mass spectrum, $m_{\mu\mu}$, the Z background forms a broad peak centred around the mass of the Z-boson. The remaining backgrounds are expected to be continuously falling. By contrast, the signal is expected to be localised around

the mass of the Higgs boson. The remaining backgrounds consist of top and di-boson processes. These backgrounds are expected and found to be continuously decreasing in $m_{\mu\mu}$ and to be much smaller than the Z background but non-negligible relative to the signal.

The backgrounds for this analysis are much simpler than those of the $\tau_{\mathrm{h}}\tau_{\mathrm{h}}$ analysis because mis-reconstructed particles form a negligible component of the backgrounds. The backgrounds also have a well understood shape in $m_{\mu\mu}$ which can be modelled analytically. This allows the backgrounds to be modelled using analytic functions which are fitted to data[130]. The danger of this approach is that the background functions must be fitted to the signal region. To prevent any potential bias that may arise from this, a 'spurious signal' systematic is calculated by comparing the signal strength measured when fitting to background only simulated events. The value of the signal strength ought to be zero when fitted to background-only simulated data so any deviation from this is used to quantify the bias from a given choice of background and signal functions.

8.2 Data Samples

The data sample used for this analysis was collected from $\sqrt{s} = 8$ TeV proton-proton collisions collected during 2012. This corresponds to an integrated luminosity of 20.3 fb^{-1}. The data was collected using a combination of the following muon triggers:

- `EF_mu_24i_tight`
- `EF_mu36_tight`
- `EF_mu18_tight_mu8_EFFS`,

described in Chapter 4. The dataset was restricted to periods in which the ATLAS detector was fully operational.

8.3 Simulated Samples

All simulated samples are re-weighted using data-driven methods to match the pile-up, efficiency and performance in the ATLAS detector. The interaction of each sample with

the detector is modelled by GEANT4[63]. The muon momentum is also further smeared[131] to account for the lower muon resolution observed in the ATLAS detector relative to that which was expected from simulation.

8.3.1 Signal Samples

The simulated signal samples are generated separately for a Higgs boson mass with a mass between 100-150 GeV in 5 GeV increments. The samples are restricted to processes in which the Higgs boson decays to two oppositely charged muons. The branching fraction as a function of Higgs boson mass is calculated using the HDECAY[132] program.

The ggF and VBF samples are calculated with POWHEG[105] at NLO with the showering modelled by PYTHIA[64]. The CT10 PDF tune[75] is used with the ATLAS underlying event tune[82]. For ggF, the transverse momentum distribution is retuned to agree with the predictions from HqT[133]. The VH samples are generated by PYTHIA8[65] with CTEQ6[134] as the PDF and AU2[82] as the tune.

8.3.2 Background Samples

Although the backgrounds are estimated using data-driven techniques, simulated background samples were still generated and used for validation studies. The list of generators, showering software, PDFs and tunes are listed for each major sample in Table 8.2.

8.3.3 Generator Level Samples

The majority of computing time to generate samples is devoted to modelling the particle-detector interactions. The need for very high statistic samples for spurious signal studies has led to samples being generated which consist of generator level information smeared to match the observed muon momentum distribution.

Cut	Value
Calorimeter Isolation	EtConeCor30/p_T < 0.12 for 15 GeV < p_T < 20 GeV
Calorimeter Isolation	EtConeCor30/p_T < 0.18 for 20 GeV < p_T < 25 GeV
Calorimeter Isolation	EtConeCor30/p_T < 0.30 for p_T > 25 GeV
Track Isolation	PtCone40/p_T < 0.06 for 15 GeV < p_T < 20 GeV
Track Isolation	PtCone30/p_T < 0.08 for 15 GeV < p_T < 20 GeV
Track Isolation	PtCone30/p_T < 0.12 for p_T > 20 GeV
d_0 Significance	< 3.0
$\|z_0 \sin\theta\|$	< 1.0 mm

Table 8.1: Requirements on the muon isolation and impact parameters.

8.4 Object Definitions

8.4.1 Muons

Muons are reconstructed using the STACO combined muon algorithm. To suppress non-prompt leptons and fake leptons, a series of requirements were on the calorimeter and track isolation of the muons. In addition, track impact parameters are also placed on the muons relative to the main interaction point. These are summarised in Table 8.1. Furthermore, any muons within $\Delta R < 0.05$ of a jet are vetoed.

8.4.2 Jets

The jets are reconstructed from topo-clusters using the anti-k_t algorithm with a distance parameter of 0.4. A jet vertex fraction requirement of |JVT| > 0.5 was also placed on jets with $p_T < 50$ GeV and $|\eta| < 2.4$.

8.4.3 B-Tagged Jets

To reduce the contribution from top backgrounds, it is useful to define and veto events containing jets originating from b quarks. To be b-tagged, a jet must pass the above jet criteria as well as occurring within the range $|\eta| < 2.5$. The ATLAS b-tagging algorithm uses a neural network based algorithm which operates on the output of the trackers and calorimeters to distinguish b-quark initiated jets from regular jets. B-tagged jets are characterised by a displaced secondary vertex (corresponding to a long lived intermediate B-meson) and a distinctive shower shape in the electromagnetic calorimeters. A score of

80% in the MV1 algorithm is required to be b-tagged.

8.4.4 Missing Transverse Energy

To reduce the contribution from top and di-boson background, it is useful to reconstruct the MET in the event. The MET is calculated from the reconstructed energy deposits in the calorimeters and the muon spectrometers. Further corrections are added to reduce the contribution from low energy particles present in the ID and muons present in the inner detector but not associated to MS tracks due to limited detector coverage. As in Section 7.5.4, the definition of MET used in this analysis consists of an object level MET with a separate term for calorimeter cells not associated with any reconstructed objects. The methods differ in the way in which soft terms, jets and tracks are incorporated. The full definitions of the MET used is available in Reference [135].

8.5 Event Selections

The event selections are shown in Table 8.3. The signal regions are divided into two resolution categories and divided by the reconstructed Higgs boson p_T or whether it is compatible with the VBF topology. The $m_{\mu\mu}$ distribution is shown after the preselection requirements in Figure 8.1.

8.6 Background Composition and Modelling

The analytical background model is a probability distribution function (PDF) of the di-muon invariant mass, $m_{\mu\mu}$. It is composed of four components:

- Breit-Wigner function to describe the resonant component of $Z/\gamma^* \rightarrow \mu\mu$ background.
- A Gaussian function which is convolved with the Breit-Wigner to correct for muon resolution.
- A x^{-3} function to describe the continuous portion of the $Z/\gamma^* background$.
- An exponential function to describe the effects of the di-boson and top processes.

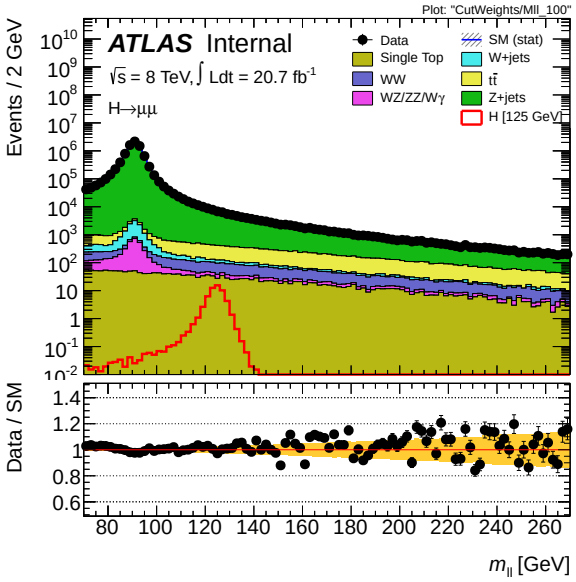

Figure 8.1: The di-muon invariant mass distribution. The lower part of each plot shows the ratio between the data and the background expectation from MC, with the yellow band indicating the only statistical uncertainty in the normalisation of the various components. The signal is shown for $m_H = 125$ GeV.

The combined background PDF can then be described by the following formula:

$$f_b\left(m_{\mu\mu}\right) = f \cdot \left(\mathrm{BW} * \mathrm{GS}\right)\left(m_{\mu\mu}\right) + (1-f) \cdot \mathrm{PDF}\left(\exp^{\mathrm{B}\cdot m_{\mu\mu}}\right), \tag{8.1}$$

where the BW refers to the non-relativistic form of the Breit-Wigner function

$$\mathrm{BW}\left(m_{\mu\mu}\right) = \mathrm{PDF}\left(\frac{1}{\left(m_{\mu\mu} - M_Z\right)^2 + \left(\frac{\Lambda_Z}{2}\right)^2}\right). \tag{8.2}$$

The values of M_Z and Λ_Z are fixed at their experimentally measured values of 91.2 GeV and 2.49 GeV respectively, while the detector resolution (σ_{GS}) is estimated from simulation separately in each of the $p_{T,ll}$ categories. The remaining parameters (B, f) are determined by performing a fit to data. The best fit values of these parameters using simulated events are shown in Figure 8.6 and 8.7 along with the overall goodness-of-fit and pull plots. These pull plots shown no systematic bias and any deviation is consistent with the statistical errors.

The background modelling used in the VBF signal region usses a simplified version of 8.1. This modification was motivated by the observation that the parameter f was not well

Table 8.2: Summary of background samples used in the $H \to \mu\mu$ analysis.

Sample	Generator
DY$\to \mu\mu$	Powheg[74]+Pythia8[65]
$q\bar{q} \to W^+W^-$	Powheg+Pythia8
$gg \to W^+W^-$	gg2WW[136]
$q\bar{q} \to W^{+/-}Z$	Powheg+Pythia8
$q\bar{q} \to W^{+/-}\gamma^*$	MadGraph[99]
$q\bar{q} \to W^{+/-}\gamma$	Alpgen[83]
$q\bar{q} \to ZZ$	Powheg+Pythia[64]
$gg \to ZZ$	gg2ZZ[137]
$q\bar{q} \to W^{+/-}$	Alpgen
$q\bar{q}/gg \to t\bar{t}$	MC@NLO[85]
Single top (t channel)	AcerMC[86]
Single top (s channel)	MC@NLO
W+t	MC@NLO
ggF	Powheg+Pythia
VBF	Powheg+Pythia
WH/ZH	Pythia

constrained in the fit. The background model that was adopted was

$$f_b\left(m_H\right) = \mathrm{BW}\left(m_H\right) \cdot \exp^{\mathrm{B}\cdot m_H}, \tag{8.3}$$

where the normalisation factor has been excluded. Note that the fit variable has been changed to m_H to reflect the fact that the invariant mass now includes the two tagged jets.

The choice of background model in each category has ultimately been chosen based on which minimises the spurious signal systematic described in Section 8.8.

8.7 Modelling of Signal

The expected distribution of signal events is expected to be a Gaussian function centred about the mass of the Higgs boson. The presence of final state radiation, which is not reconstructed in this analysis, causes the signal to be skewed towards the low mass region. To compensate for this asymmetry, the Gaussian function (GS) is summed with a crystal ball function (CB). The following PDF is used to describe the signal:

$$f_b\left(m_{\mu\mu}\right) = f_{\mathrm{CB}} \cdot \mathrm{CB}\left(m_{\mu\mu}, m_{\mathrm{CB}}, \sigma_{\mathrm{CB}}, \alpha, n\right) + \left(1 - f_{\mathrm{CB}}\right) \cdot \mathrm{GS}\left(m_{\mu\mu}, m_{\mathrm{GS}}, \sigma_{\mathrm{GS}}\right). \tag{8.4}$$

Cut	Description
Triggers	EF_mu24i_tight or EF_mu36_tight or EF_mu18_tight_mu8_EFFS
Preselection	2 isolated STACO combined muons with trigger matching, vertex impact parameter cuts
Selection	Oppositely charged muons leading muon $p_T > 25$ GeV subleading muon $p_T > 15$ GeV di-muon invariant mass 110 GeV $< m_{\mu\mu} <$ 160 GeV
b-tag veto (only VBF)	$E_T^{\text{miss}} < 80$ GeV no b-tagged jet MV1 80%
VBF	at least 2 jets p_T^{Jet} >25 (30) GeV for $\lvert\eta^{Jet}\rvert < (\geq)2.4$, m_{jj} >500 GeV, $\lvert\Delta\eta_{jj}\rvert$ >3, $\eta_j^1 * \eta_j^2 < 0$
$p_T^{\mu\mu}$ > categorization	(1) $p_T^{\mu\mu}$ <15 GeV (2) 15 GeV< $p_T^{\mu\mu}$ <50 GeV (3) $p_T^{\mu\mu}$ >50 GeV
μ resolution category	(1) $\lvert\eta_{\mu 1}\rvert$ <1 AND $\lvert\eta_{\mu 2}\rvert$ <1 (2) $\lvert\eta_{\mu 1}\rvert$ >=1 OR $\lvert\eta_{\mu 1}\rvert$ >=1

Table 8.3: Summary of the selection requirements in the $H \to \mu\mu$ analysis.

The mean of the Gaussian and the crystal ball function, $m_{\text{CB,GS}}$, are set to the Higgs boson mass in the simulation sample. The rate at which the power law tail decays, n, is set at 2. The remaining parameters, α and σ, are set using a fit. The width of both the crystal ball function and Gaussian, $\sigma_{\text{CB,GS}}$ are allowed to float but are fixed to be equal. The fit to the simulated Higgs boson di-muon mass spectrum are shown in Figure 8.2. These plots show all deviation from that predicted by simulation is within statistical errors.

The simulated samples are available in increments of 5 GeV. The sensitivity of this channel to the mass of the Higgs boson makes smaller mass increments in the signal samples desirable. To achieve this, the parameters of the signal PDF are interpolated using an order four polynomial as shown in Figure 8.2. A similar interpolation is performed on the expected number of signal events as a function of mass as shown in Figure 8.3.

8.8 Spurious Signal Systematics

The measurement of the spurious signal systematic forms the main systematic on the background model. The spurious signal method involves first finding a signal free control

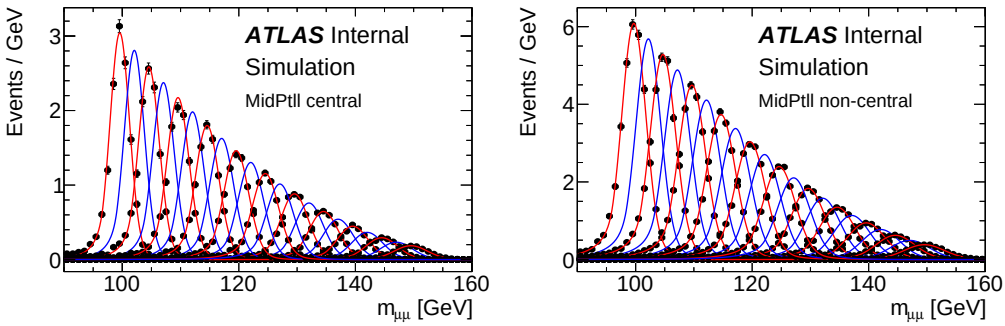

Figure 8.2: Invariant mass distribution of the simulated signal samples (solid circles) superimposed with their corresponding signal model (red) and the interpolated signal model (blue) for the medium $p_{T,ll}$ category.

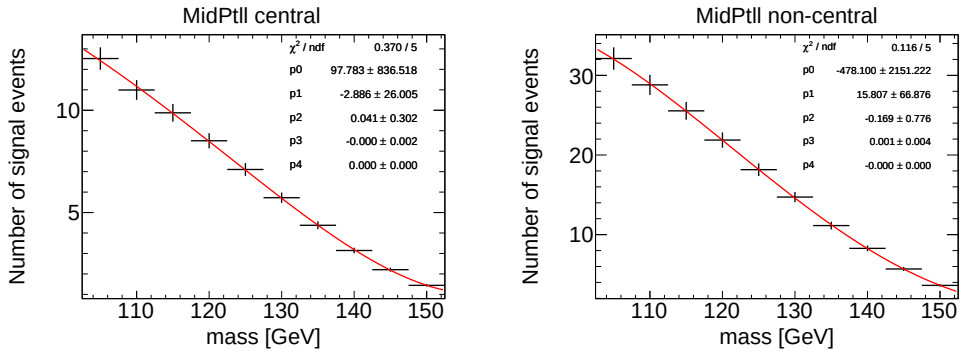

Figure 8.3: A number of expected Higgs events plotted as a function of the Higgs mass for this medium $p_{T,ll}$ category in the barrel (left) and non-barrel region (right).

sample. The analytic function of interest is

$$\mathrm{F} = \mathrm{F}_{\mathrm{bkg}} + \mathrm{F}_{\mathrm{sig}} \times \mu \tag{8.5}$$

with μ freely floating, is fitted to the control sample. The control sample, by construction, is free of any signal events and any non-zero value of μ is deemed to be spurious and an artifact of the background estimation method. The resulting value of μ as a function of the fit parameter is used as a systematic. The root mean square (RMS) deviation from the expected number of background-only events is incorporated in the likelihood function described in Section 8.10

The spurious signal systematic has been determined using fits to the background samples. The background samples have generated events corresponding to forty times the number of events expected in data. Despite the much higher statistics, the spurious signal systematics were found to be within statistical errors and it was not possible to decide, on this basis,

whether spurious signals are indeed present. To improve statistics, generator level samples were used with muon smearing. It is possible to generate much higher statistics with generator level samples because the ATLAS detector does not need to be simulated. It is not possible use generator level systematics in the VBF category due to the presence of reconstructed jets.

The results from performing the spurious signal systematics on smeared generator level samples are shown in Figure 8.4. The most significant spurious signal was found in the low $p_{T,ll}$ region.

8.9 Systematics

In contrast to the Higgs-Tau coupling measurement, this measurement uses only data and analytic functions in the final fit. As such, the background systematics need not include the reconstruction and simulation uncertainties that are normally applied to simulation. The set of experimental systematics used are discussed in Chapter 4.

The theoretical uncertainties consist of variations in the luminosity, branching ratio, QCD parton distribution functions, variations in the strong force and theoretical uncertainties from higher order loop uncertainties in the production diagrams. Added to this are the systematic variations in the number of final state jets and multi-parton interactions. These systematics are incorporated using the recommendations in References [138]. In addition, the effect of reweighting the Higgs boson p_T for ggF production is also included as described in Reference [139, 140].

The experimental systematics and detector effects mainly influence the expected number of signal events. Systematics variations in the muon identification, muon isolation, muon reconstruction, jet reconstruction, jet energy scale, jet energy scale and jet flavour composition. Summing these errors in quadrature, they have been found to contribute less than a one percent variation in the expected number of signal events. The effect of the experimental systematics on the signal sample (with $m_H = 125$ GeV) are shown in Figure 8.5.

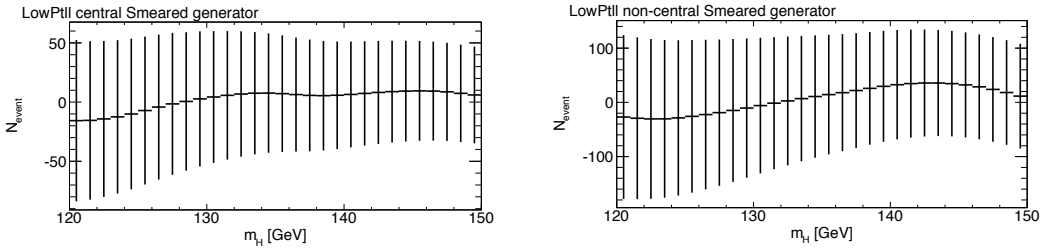

(a)

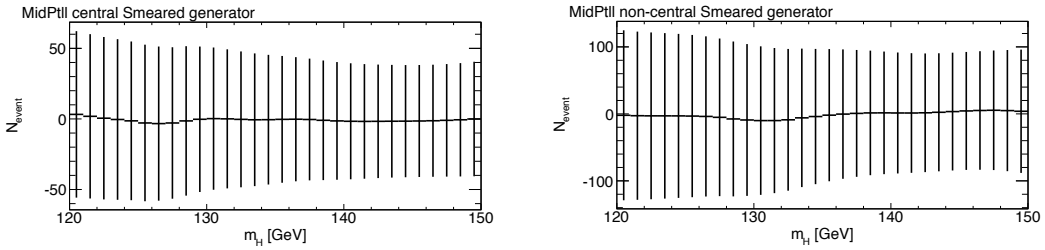

(b)

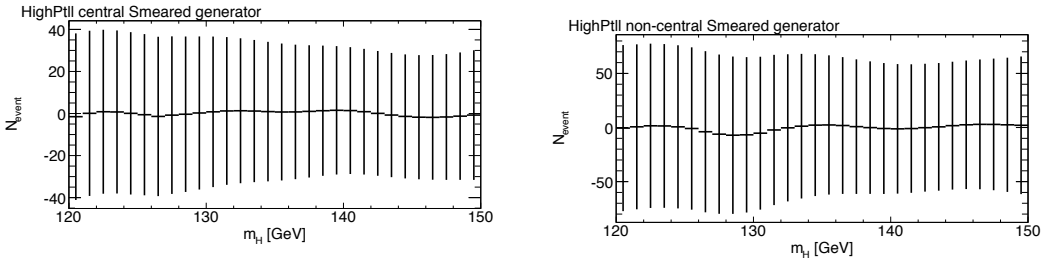

(c)

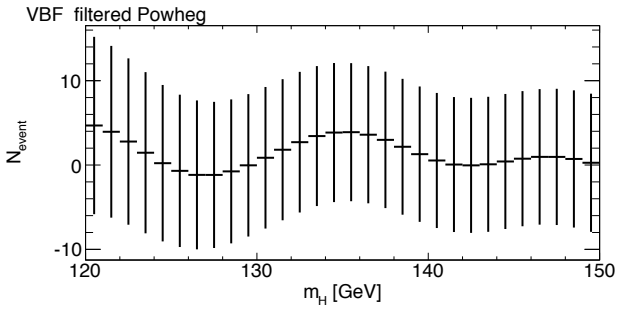

(d)

Figure 8.4: The number of spurious signal events in each category using smeared generator level samples for (a) low, (b) mid and (c) high $p_{T,ll}$ category. The VBF figure is shown in (d) but the spurious signal check can only be done using lower statistic fully simulated samples.

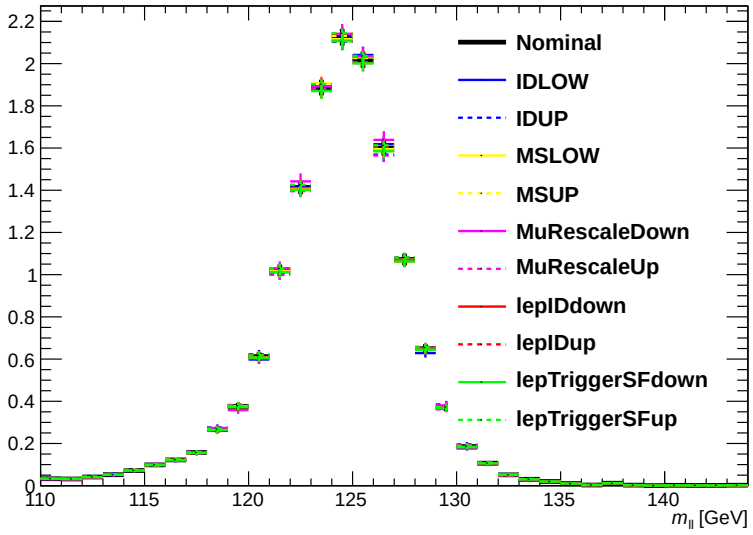

Figure 8.5: The variation about the nominal of the experimental systematics for the signal sample with $m_H = 125$ GeV. The variations due to muon identification (lepID), muon spectrometer (MS), inner detector (ID) and muon trigger (lepTrigger) are shown.

8.10 Statistical Methods

The statistical methods used in this measurement are identical to the methods used in the Higgs-Tau coupling measurement. However, this decay mode of the Higgs boson is not sensitive enough to produce an estimate of the Higgs-muon coupling. Instead an upper limit is placed on this coupling. These limits are calculated using the statistical method in Section 7.10 and Reference [141]. The spurious signal systematic does slightly modify the likelihood function used in this analysis with the change:

$$\mu \cdot s \rightarrow \mu \cdot s + s_{\text{spurious}} \tag{8.6}$$

in equation 7.3 of Section 7.10. The value of s_{spurious} is the number of spurious signal events.

8.11 Results

Figures 8.6 and 8.7 show the background-only fits in each of the eight background categories. The combined limits from this are then shown in 8.8. At $m_H = 125$ GeV, the

observed limit was 7.1 times the Standard Model. This is compatible with the expected limit of 7.15 times the Standard Model.

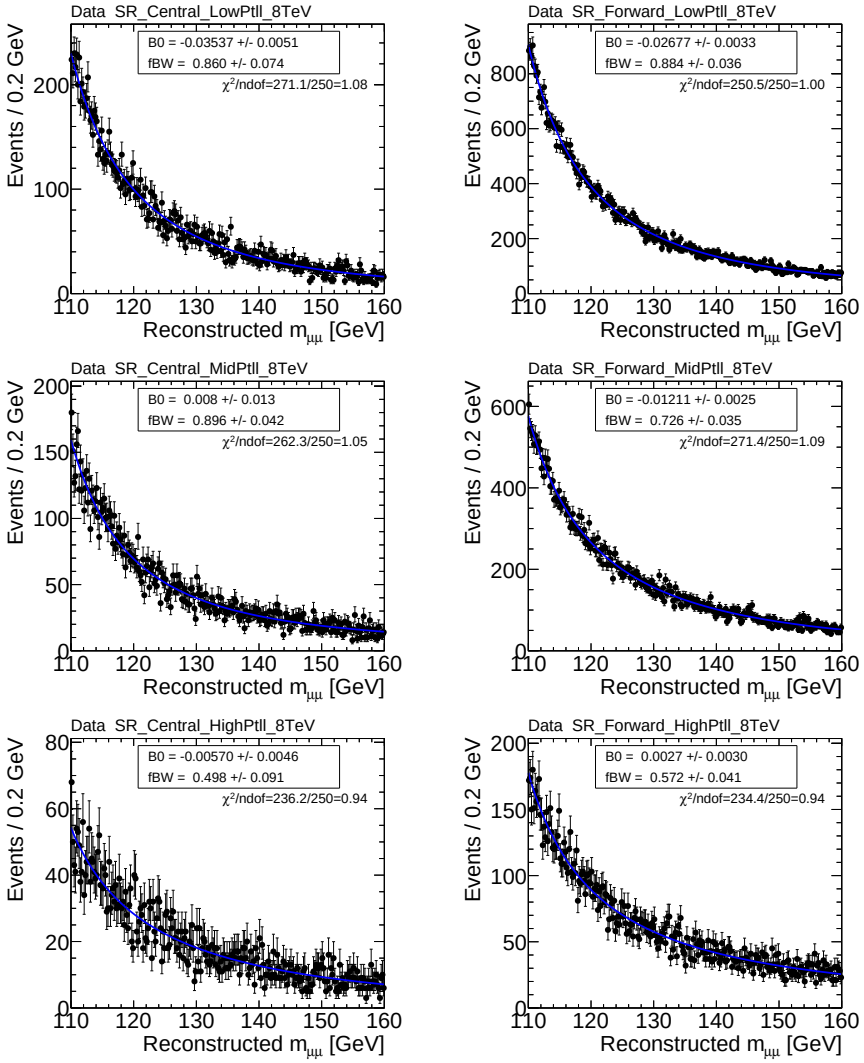

Figure 8.6: Di-muon invariant mass distribution for 8 TeV data with fitting function for the central (left) and the non-central (right) regions. The lowest transverse momentum categories are shown at the top of the figure with the highest on the bottom.

8.12 Future Sensitivity

With 20.3 fb^{-1} of data, the ATLAS detector was not expected, nor was it able, to produce a sensitive measurement of a Standard Model like Higgs boson in this channel. The potential still remains for a measurement of this process given more data and higher energy. To estimate the future sensitivity of this model, two scenarios are considered. Both

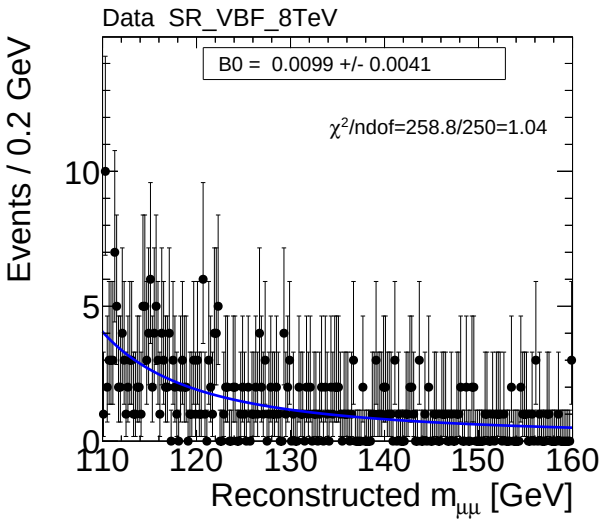

Figure 8.7: Di-muon invariant mass distribution with 8 TeV data for the VBF analysis category usef for publication.

scenarios assumed a centre-of-mass energy of 14 TeV for the protons. The first scenario assumes 300 fb^{-1} of data consistent with the planned data expected to be accumulated by the LHC through its productive life. The second scenario considers the 3000 fb^{-1} expected if a High-Luminosity LHC is operated. Both scenarios are expected to have different luminosities relative to Run 1 but the di-muon final state is expected to be robust under the increased pile-up expected from both of these scenarios.

To estimate the sensitivity, the analysis is re-run using the 2012 simulation with the various background and signal processes re-weighted to their expected cross-sections. These results are shown below in Figure 8.9. In both cases the Standard Model Higgs boson can be excluded with 95% confidence in the event that the Higgs boson does not decay to muons.

8.13 Regarding the Higgs-Electron Yukawa Coupling

Given the future sensitivity estimates of the Higgs-muon coupling, it seems unlikely that a measurement of the Higgs-electron coupling could be made. Given that the Higgs boson coupling to leptons scales linearly with mass in the Standard Model, the decay rate of a Higgs boson to electrons can be expected to be approximately one percent of the rate to muons. Complicating this, the backgrounds are expected to have a similar composition

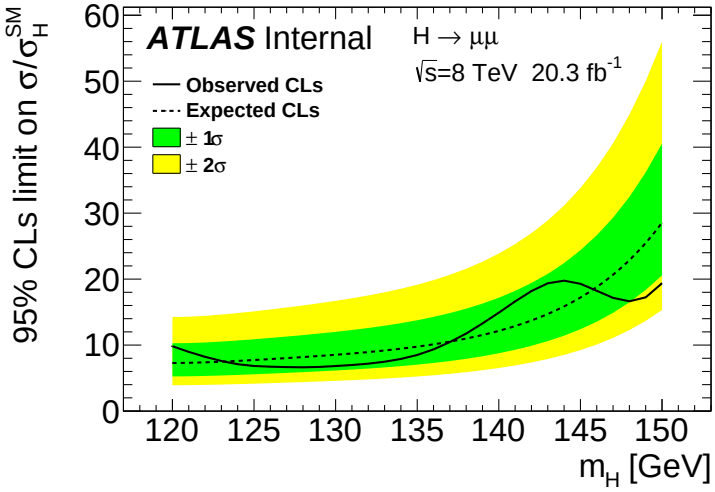

Figure 8.8: Observed and expected confidence limits at 95% using 8 TeV.

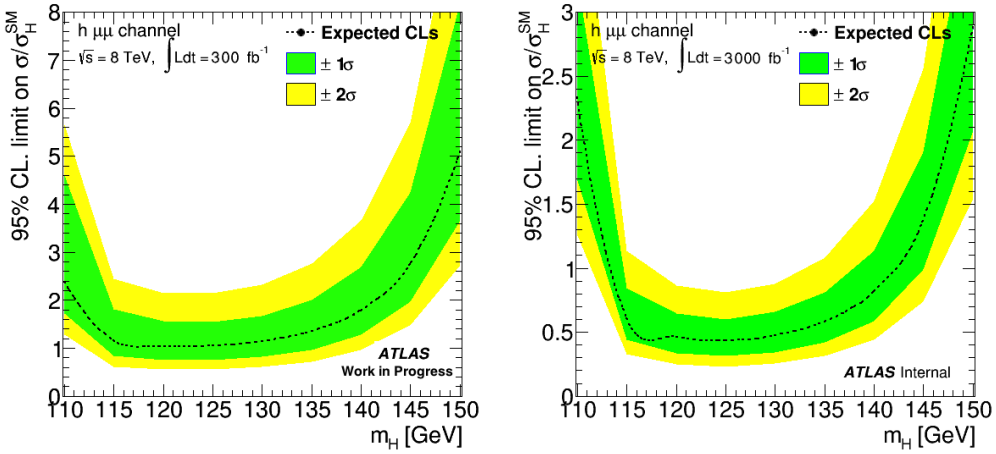

Figure 8.9: Expected confidence limits at 95% at 14 TeV using 300 fb^{-1} (left) and 3000 fb^{-1} (right).

to the muon channel due to lepton universality but with a higher rate of fakes from pions and other QCD processes. Finally, the electron has worse resolution than the muon in nearly all regions of the ATLAS detector and also suffers from larger systematics. The combination of all these factors make a Higgs-electron measurement unlikely even in the more optimistic scenario of a High Luminosity LHC producing 3000 fb^{-1} of data.

Chapter 9

Conclusion

The main focus of the physics program at the ATLAS experiment are precision measurements of the Higgs boson. At the current estimated mass of the Higgs boson, a wide range of measurements are possible. In this thesis, the current status of Higgs-Lepton Yukawa coupling measurements with the ATLAS detector have been presented. The two decays for which a measurement of the Standard Model couplings are possible, the di-tau and di-muon decay, have been extensively studied and recorded. Several techniques have been proposed and used to increase the sensitivity of this measurement including the modified Fox Wolfram moments.

In the di-tau channel, a 2.0 σ signal has been observed in the all hadronic decay channel using the latest 13 TeV data. This can coupled with the earlier 7 and 8 TeV measurements of all tau decay channels which observed a 1.8 σ excess in the all hardonic di-tau decay channel.

Similarly the Higgs-muon Yukawa coupling measurement has been performed but the sensitivity isn't sufficient at this time to be sensitivite to a Standard Model Higgs. Instead, limits were placed with a 95% confidence on the Higgs-muon Yukawa of 7.1 times the Standard Model. Given the expected data from the High Luminosity LHC, the channel becomes sufficient to exclude the Standard Model Higgs-muon Couplings. A similar observation of the Higgs-electron coupling is unlikely given all future LHC operating plans.

Bibliography

[1] ATLAS Collaboration. "Observation of a new particle in the search for the Standard Model Higgs boson with the ATLAS detector at the LHC". In: *Phys. Lett. B* 716 (2012), p. 1. DOI: 10.1016/j.physletb.2012.08.020. arXiv: 1207.7214 [hep-ex].

[2] Serguei Chatrchyan et al. "Observation of a new boson at a mass of 125 GeV with the CMS experiment at the LHC". In: *Phys. Lett.* B716 (2012), pp. 30–61. DOI: 10.1016/j.physletb.2012.08.021. arXiv: 1207.7235 [hep-ex].

[3] ATLAS and CMS Collaborations. "Combined Measurement of the Higgs Boson Mass in pp Collisions at $\sqrt{s} = 7$ and 8 TeV with the ATLAS and CMS Experiments". In: *Phys. Rev. Lett.* 114 (2015), p. 191803. DOI: 10.1103/PhysRevLett.114.191803. arXiv: 1503.07589 [hep-ex].

[4] ATLAS Collaboration. "Evidence for the Higgs-boson Yukawa coupling to tau leptons with the ATLAS detector". In: *JHEP* 04 (2015), p. 117. DOI: 10.1007/JHEP04(2015)117. arXiv: 1501.04943 [hep-ex].

[5] Gerard 't Hooft and M. J. G. Veltman. "Regularization and Renormalization of Gauge Fields". In: *Nucl. Phys.* B44 (1972), pp. 189–213. DOI: 10.1016/0550-3213(72)90279-9.

[6] Stephen P. Martin. "A Supersymmetry primer". In: (1997). [Adv. Ser. Direct. High Energy Phys.18,1(1998)]. DOI: 10.1142/9789812839657_0001,10.1142/9789814307505_0001. arXiv: hep-ph/9709356 [hep-ph].

[7] T. P. Cheng and L. F. Li. *GAUGE THEORY OF ELEMENTARY PARTICLE PHYSICS*. 1984.

[8] F. Englert and R. Brout. "Broken symmetry and the mass of gauge vector mesons". In: *Phys. Rev. Lett.* 13 (1964), pp. 321–323. DOI: 10.1103/PhysRevLett.13.321.

[9] Peter W. Higgs. "Broken symmetries and the masses of gauge bosons". In: *Phys. Rev. Lett.* 13 (1964), pp. 508–509. DOI: 10.1103/PhysRevLett.13.508.

[10] John R. Ellis, Mary K. Gaillard, and Dimitri V. Nanopoulos. "A Phenomenological Profile of the Higgs Boson". In: *Nucl. Phys.* B106 (1976), p. 292. DOI: 10.1016/0550-3213(76)90382-5.

[11] H.M. Georgi et al. "Higgs bosons from two gluon annihilation in proton proton collisions". In: *Phys. Rev. Lett.* 40 (1978), pp. 692–694. DOI: 10.1103/PhysRevLett.40.692.

[12] M. Spira et al. "Higgs boson production at the LHC". In: *Nucl. Phys.* B453 (1995), pp. 17–82. DOI: 10.1016/0550-3213(95)00379-7. arXiv: hep-ph/9504378 [hep-ph].

[13] LHC Higgs Cross Section Working Group et al. "Handbook of LHC Higgs Cross Sections: 3. Higgs Properties". In: *CERN-2013-004* (CERN, Geneva, 2013). DOI: 10.5170/CERN-2013-004. arXiv: 1307.1347 [hep-ph].

[14] S. Dittmaier et al. "Handbook of LHC Higgs Cross Sections". In: (2011). DOI: 10.5170/CERN-2011-002. arXiv: 1101.0593 [hep-ph].

[15] C. Patrignani et al. "Review of Particle Physics". In: *Chin. Phys.* C40.10 (2016), p. 100001. DOI: 10.1088/1674-1137/40/10/100001.

[16] Thomas Hambye and Kurt Riesselmann. "SM Higgs mass bounds from theory". In: *e+ e- linear colliders: Physics and detector studies. Proceedings, Workshops, ECFA/DESY, Frascati, Italy, February 5-6, 1996, London, UK, July 4-6, 1996, Munich, Germany, September 16-18, 1996 and Hamburg, Germany, November 20-22, 1996. Pt.E.* 1997. arXiv: hep-ph/9708416 [hep-ph]. URL: http://alice.cern.ch/format/showfull?sysnb=0255880.

[17] Guido Altarelli and G. Isidori. "Lower limit on the Higgs mass in the standard model: An Update". In: *Phys. Lett.* B337 (1994), pp. 141–144. DOI: 10.1016/0370-2693(94)91458-3.

[18] J. A. Casas, J. R. Espinosa, and M. Quiros. "Improved Higgs mass stability bound in the standard model and implications for supersymmetry". In: *Phys. Lett.* B342 (1995), pp. 171–179. DOI: 10.1016/0370-2693(94)01404-Z. arXiv: hep-ph/9409458 [hep-ph].

[19] J. A. Casas, J. R. Espinosa, and M. Quiros. "Standard model stability bounds for new physics within LHC reach". In: *Phys. Lett.* B382 (1996), pp. 374–382. DOI: 10.1016/0370-2693(96)00682-X. arXiv: hep-ph/9603227 [hep-ph].

[20] ATLAS Collaboration. "A Particle Consistent with the Higgs Boson Observed with the ATLAS Detector at the Large Hadron Collider". In: *Science* 338 (2012), p. 1576. DOI: 10.1126/science.1232005.

[21] "Search for the standard model Higgs boson at LEP". In: (2001). [PoSHEP2001,128(2001)]. arXiv: hep-ex/0107029 [hep-ex].

[22] CDF and D0 Collaborations, T. Aaltonen et al. "Combination of Tevatron Searches for the Standard Model Higgs Boson in the W^+W^- Decay Mode". In: *Phys. Rev. Lett.* 104 (2010), p. 061802. DOI: 10.1103/PhysRevLett.104.061802. arXiv: 1001.4162.

[23] G. L. Bayatian et al. "CMS technical design report, volume II: Physics performance". In: *J. Phys.* G34.6 (2007), pp. 995–1579. DOI: 10.1088/0954-3899/34/6/S01.

[24] G. L. Bayatian et al. "CMS physics: Technical design report". In: (2006).

[25] A. Airapetian et al. "ATLAS: Detector and physics performance technical design report. Volume 2". In: (1999).

[26] A. Airapetian et al. "ATLAS: Detector and physics performance technical design report. Volume 1". In: (1999).

[27] ATLAS and CMS Collaborations. "Measurements of the Higgs boson production and decay rates and constraints on its couplings from a combined ATLAS and CMS analysis of the LHC pp collision data at $\sqrt{s} = 7$ and 8 TeV". In: *JHEP* 08 (2016), p. 045. DOI: 10.1007/JHEP08(2016)045. arXiv: 1606.02266 [hep-ex].

[28] ATLAS Collaboration. "Study of the spin and parity of the Higgs boson in diboson decays with the ATLAS detector". In: *Eur. Phys. J. C* 75 (2015), p. 476. DOI: 10.1140/epjc/s10052-015-3685-1. arXiv: 1506.05669 [hep-ex].

[29] *Constraints on the Higgs boson width from off-shell production and decay to ZZ to llll and llvv*. Tech. rep. CMS-PAS-HIG-14-002. Geneva: CERN, 2014. URL: https://cds.cern.ch/record/1670066.

[30] ATLAS Collaboration. "Constraints on the off-shell Higgs boson signal strength in the high-mass ZZ and WW final states with the ATLAS detector". In: *Eur. Phys. J. C* 75 (2015), p. 335. DOI: 10.1140/epjc/s10052-015-3542-2. arXiv: 1503.01060 [hep-ex].

[31] ATLAS Collaboration. "The ATLAS Experiment at the CERN Large Hadron Collider". In: *JINST* 3 (2008), S08003. DOI: 10.1088/1748-0221/3/08/S08003.

[32] Lyndon Evans and Philip Bryant. "LHC machine". In: *Journal of Instrumentation* 3.08 (2008), S08001.

[33] Atlas Collaboration et al. "ATLAS detector and physics performance technical design report". In: *CERN/LHCC* 99.14 (1999), pp. 99–15.

[34] J Incandela and F Gianotti. "Latest update in the search for the Higgs boson". In: *public seminar at CERN. Video: http://cds. cern. ch/record/1459565*. 2012.

[35] Michael Benedikt. *LHC Design Report: The LHC Injector Chain*. CERN, 2004.

[36] ATLAS Collaboration. "Improved luminosity determination in pp collisions at $\sqrt{s} = 7$ TeV using the ATLAS detector at the LHC". In: *Eur. Phys. J. C* 73 (2013), p. 2518. DOI: 10.1140/epjc/s10052-013-2518-3. arXiv: 1302.4393 [hep-ex].

[37] ATLAS Collaboration. "Luminosity determination in pp collisions at $\sqrt{s} = 8$ TeV using the ATLAS detector at the LHC". In: (2016). arXiv: 1608.03953 [hep-ex].

[38] S. Chatrchyan et al. "The CMS Experiment at the CERN LHC". In: *JINST* 3 (2008), S08004. DOI: 10.1088/1748-0221/3/08/S08004.

[39] A. Augusto Alves Jr. et al. "The LHCb Detector at the LHC". In: *JINST* 3 (2008), S08005. DOI: 10.1088/1748-0221/3/08/S08005.

[40] K. Aamodt et al. "The ALICE experiment at the CERN LHC". In: *JINST* 3 (2008), S08002. DOI: 10.1088/1748-0221/3/08/S08002.

[41] ATLAS Collaboration et al. "ATLAS luminosity public results". In: *ATLAS Luminosity website* (2016).

[42] E. N Dawe. *tikz-Track*. https://github.com/ndawe/tikz-track. 2014.

[43] *ATLAS magnet system: Technical Design Report, 1*. Technical Design Report ATLAS. Geneva: CERN, 1997. URL: https://cds.cern.ch/record/338080.

[44] M. Abolins et al. “The ATLAS Data Acquisition and High Level Trigger system”. In: *JINST* 11.06 (2016), P06008. DOI: 10.1088/1748-0221/11/06/P06008.

[45] Tilman Plehn. “Lectures on LHC Physics”. In: *Lect. Notes Phys.* 844 (2012), pp. 1–193. DOI: 10.1007/978-3-642-24040-9. arXiv: 0910.4182 [hep-ph].

[46] Walter Lampl et al. *Calorimeter Clustering Algorithms: Description and Performance*. ATL-LARG-PUB-2008-002. 2008. URL: https://cds.cern.ch/record/1099735.

[47] ATLAS Collaboration. “Electron efficiency measurements with the ATLAS detector using the 2012 LHC proton-proton collision data”. In: ATLAS-CONF-2014-032 (2014). URL: https://cds.cern.ch/record/1706245.

[48] ATLAS Collaboration. *Expected photon performance in the ATLAS experiment*. ATL-PHYS-PUB-2011-007. 2011. URL: https://cds.cern.ch/record/1345329.

[49] ATLAS Collaboration. “Electron and photon energy calibration with the ATLAS detector using LHC Run 1 data”. In: *Eur. Phys. J. C* 74 (2014), p. 3071. DOI: 10.1140/epjc/s10052-014-3071-4. arXiv: 1407.5063 [hep-ex].

[50] ATLAS Collaboration. “Measurement of the muon reconstruction performance of the ATLAS detector using 2011 and 2012 LHC proton–proton collision data”. In: *Eur. Phys. J. C* 74 (2014), p. 3130. DOI: 10.1140/epjc/s10052-014-3130-x. arXiv: 1407.3935 [hep-ex].

[51] Matteo Cacciari, Gavin P. Salam, and Gregory Soyez. “FastJet User Manual”. In: *Eur. Phys. J. C* 72 (2012), p. 1896. DOI: 10.1140/epjc/s10052-012-1896-2. arXiv: 1111.6097 [hep-ph].

[52] M. Cacciari, G. P. Salam and G. Soyez. “The anti-k_t jet clustering algorithm”. In: *JHEP* 04 (2008), p. 063. DOI: 10.1088/1126-6708/2008/04/063. arXiv: 0802.1189 [hep-ph].

[53] ATLAS Collaboration. “Topological cell clustering in the ATLAS calorimeters and its performance in LHC Run 1”. In: (2016). arXiv: 1603.02934 [hep-ex].

[54] ATLAS Collaboration. *Properties of jets and inputs to jet reconstruction and calibration with the ATLAS detector using proton–proton collisions at* $\sqrt{s} = 13$ *TeV*. ATL-PHYS-PUB-2015-036. 2015. URL: https://cds.cern.ch/record/2044564.

[55] ATLAS Collaboration. "Jet energy measurement and its systematic uncertainty in proton–proton collisions at $\sqrt{s} = 7$ TeV with the ATLAS detector". In: *Eur. Phys. J. C* 75 (2015), p. 17. DOI: 10.1140/epjc/s10052-014-3190-y. arXiv: 1406.0076 [hep-ex].

[56] ATLAS Collaboration. *Jet Calibration and Systematic Uncertainties for Jets Reconstructed in the ATLAS Detector at* $\sqrt{s} = 13$ *TeV*. ATL-PHYS-PUB-2015-015. 2015. URL: https://cds.cern.ch/record/2037613.

[57] ATLAS Collaboration. *Jet global sequential corrections with the ATLAS detector in proton–proton collisions at* $\sqrt{s} = 8$ *TeV*. ATLAS-CONF-2015-002. 2015. URL: https://cds.cern.ch/record/2001682.

[58] ATLAS Collaboration. "Performance of b-Jet Identification in the ATLAS Experiment". In: *JINST* 11 (2016), P04008. DOI: 10.1088/1748-0221/11/04/P04008. arXiv: 1512.01094 [hep-ex].

[59] ATLAS Collaboration. "Performance of algorithms that reconstruct missing transverse momentum in $\sqrt{s} = 8$ TeV proton–proton collisions in the ATLAS detector". In: (2016). arXiv: 1609.09324 [hep-ex].

[60] ATLAS Collaboration. "Performance of missing transverse momentum reconstruction in proton–proton collisions at $\sqrt{s} = 7$ TeV with ATLAS". In: *Eur. Phys. J. C* 72 (2012), p. 1844. DOI: 10.1140/epjc/s10052-011-1844-6. arXiv: 1108.5602 [hep-ex].

[61] *Expected performance of missing transverse momentum reconstruction for the ATLAS detector at* $\sqrt{s} = 13$ *TeV*. Tech. rep. ATL-PHYS-PUB-2015-023. Geneva: CERN, July 2015. URL: https://cds.cern.ch/record/2037700.

[62] A. Ribon et al. "Status of Geant4 hadronic physics for the simulation of LHC experiments at the start of the LHC physics program". In: (2010). URL: https://lcgapp.cern.ch/project/docs/noteStatusHadronic2010.pdf.

[63] S. Agostinelli et al. "GEANT4: A simulation toolkit". In: *Nucl. Instrum. Meth. A* 506 (2003), p. 250. DOI: 10.1016/S0168-9002(03)01368-8.

[64] T. Sjostrand, S. Mrenna and P. Skands. "PYTHIA 6.4 physics and manual". In: *JHEP* 05 (2006), p. 026. DOI: 10.1088/1126-6708/2006/05/026. arXiv: hep-ph/0603175 [hep-ph].

[65] T. Sjostrand, S. Mrenna and P. Skands. "A Brief Introduction to PYTHIA 8.1". In: *Comput. Phys. Commun.* 178 (2008), pp. 852–867. DOI: 10.1016/j.cpc.2008.01.036. arXiv: 0710.3820 [hep-ph].

[66] Georges Aad et al. "Performance of the ATLAS muon trigger in pp collisions at $\sqrt{s} = 8$ TeV". In: *Eur. Phys. J.* C75 (2015), p. 120. DOI: 10.1140/epjc/s10052-015-3325-9. arXiv: 1408.3179 [hep-ex].

[67] ATLAS Collaboration. "Measurement of the muon reconstruction performance of the ATLAS detector using 2011 and 2012 LHC proton-proton collision data". In: (2014). arXiv: 1407.3935 [hep-ex].

[68] ATLAS Collaboration et al. "ATLAS Tau Reconstruction public results". In: *ATLAS Tau Reconstruction website* (2016).

[69] ATLAS Collaboration. "Identification and energy calibration of hadronically decaying tau leptons with the ATLAS experiment in *pp* collisions at $\sqrt{s} = 8$ TeV". In: *Eur. Phys. J. C* 75 (2015), p. 303. DOI: 10.1140/epjc/s10052-015-3500-z. arXiv: 1412.7086 [hep-ex].

[70] ATLAS Collaboration. "Reconstruction of hadronic decay products of tau leptons with the ATLAS experiment". In: *Eur. Phys. J. C* 76 (2016), p. 295. DOI: 10.1140/epjc/s10052-016-4110-0. arXiv: 1512.05955 [hep-ex].

[71] G Nunes Hanninger and L A Spiller. *Tau Identification variables*. Tech. rep. ATL-COM-PHYS-2014-153. Geneva: CERN, Feb. 2014. URL: https://cds.cern.ch/record/1665381.

[72] The ATLAS collaboration. "The ATLAS Tau Trigger in Run 2". In: (2017).

[73] E. Simioni et al. "Upgrade of the ATLAS Level-1 Trigger with event topology information". In: *J. Phys. Conf. Ser.* 664.8 (2015), p. 082052. DOI: 10.1088/1742-6596/664/8/082052.

[74] Simone Alioli et al. "NLO Higgs boson production via gluon fusion matched with shower in POWHEG". In: *JHEP* 04 (2009), p. 002. DOI: 10.1088/1126-6708/2009/04/002. arXiv: 0812.0578 [hep-ph].

[75] Hung-Liang Lai et al. "New parton distributions for collider physics". In: (2010). arXiv: 1007.2241 [hep-ph].

[76] "Measurement of the transverse momentum distribution of Z/gamma* bosons in proton-proton collisions at roots = 7 TeV with the ATLAS detector : Update with 4.7 fb-1 of the previous measurement at this energy." In: (2013). URL: https://cds.cern.ch/record/1513133.

[77] J. Pumplin et al. "New generation of parton distributions with uncertainties from global QCD analysis". In: *JHEP* 07 (2002), p. 012. DOI: 10.1088/1126-6708/2002/07/012. arXiv: hep-ph/0201195 [hep-ph].

[78] E. Barberio, B. V. Eijk and Z. Was. "PHOTOS - a universal Monte Carlo for QED radiative corrections in decays". In: *Comput. Phys. Commun.* 66 (1991), pp. 115–128. DOI: 10.1016/0010-4655(91)90012-A.

[79] David J. Lange. "The EvtGen particle decay simulation package". In: *Nuclear Instruments and Methods in Physics Research Section A: Accelerators, Spectrometers, Detectors and Associated Equipment* 462.1 (2001). BEAUTY2000, Proceedings of the 7th Int. Conf. on B-Physics at Hadron Machines, pp. 152 –155. ISSN: 0168-9002. DOI: http://dx.doi.org/10.1016/S0168-9002(01)00089-4. URL: http://www.sciencedirect.com/science/article/pii/S0168900201000894.

[80] S. Jadach, J. H. Kuhn and Z. Was. "TAUOLA - a library of Monte Carlo programs to simulate decays of polarized τ leptons". In: *Comput. Phys. Commun.* 64 (1990), pp. 275–299. DOI: 10.1016/0010-4655(91)90038-M.

[81] E Barberio et al. *Measurement of the hadronic tau identification efficiency at* $\sqrt{s} = 8$ *TeV with the ATLAS detector at the LHC*. Tech. rep. ATL-COM-PHYS-2014-1167. Geneva: CERN, Sept. 2014. URL: https://cds.cern.ch/record/1755768.

[82] ATLAS Collaboration. *Summary of ATLAS Pythia 8 tunes*. Tech. rep. ATL-PHYS-PUB-2012-003. Geneva: CERN, Aug. 2012.

[83] M. L. Mangano, M. Moretti, F. Piccinini, R. Pittau and A. D. Polosa. "ALPGEN, a generator for hard multiparton processes in hadronic collisions". In: *JHEP* 07 (2003), p. 001. DOI: 10.1088/1126-6708/2003/07/001. arXiv: hep-ph/0206293 [hep-ph].

[84] G. Corcella et al. "HERWIG 6.5: an event generator for hadron emission reactions with interfering gluons (including supersymmetric processes)". In: *JHEP* 01

(2001), p. 010. DOI: 10.1088/1126-6708/2001/01/010. arXiv: hep-ph/0011363 [hep-ph].

[85] J. Alwall et al. "The automated computation of tree-level and next-to-leading order differential cross sections, and their matching to parton shower simulations". In: *JHEP* 1407 (2014), p. 079. DOI: 10.1007/JHEP07(2014)079. arXiv: 1405.0301 [hep-ph].

[86] B. P. Kersevan and E. Richter-Was. "The Monte Carlo event generator AcerMC version 2.0 with interfaces to PYTHIA 6.2 and HERWIG 6.5". In: (2004). arXiv: hep-ph/0405247 [hep-ph].

[87] A et al. Andreazza. *Contributions to the paper: "Identification and energy calibration of hadronically decaying tau leptons with the ATLAS experiment at* $\sqrt{s} = 8$ *TeV"*. Tech. rep. ATL-COM-PHYS-2014-953. Geneva: CERN, Aug. 2014. URL: https://cds.cern.ch/record/1747281.

[88] R. D. Field and Y. A. Kanev. "Using collider event topology in the search for the six jet decay of top quark - anti-quark pairs". In: (1997). arXiv: hep-ph/9801318 [hep-ph].

[89] Catherine Bernaciak et al. "Improving Higgs plus Jets analyses through Fox–Wolfram Moments". In: *Phys. Rev.* D89.5 (2014), p. 053006. DOI: 10.1103/PhysRevD.89.053006. arXiv: 1311.5891 [hep-ph].

[90] Catherine Bernaciak et al. "Fox-Wolfram Moments in Higgs Physics". In: *Phys. Rev.* D87 (2013), p. 073014. DOI: 10.1103/PhysRevD.87.073014. arXiv: 1212.4436 [hep-ph].

[91] Toru Iijima. "Study of rare B meson decays at BELLE". In: *B physics and CP violation. Proceedings, International Workshop, BCP4, Ise-Shima, Japan, February 19-23, 2001*. 2001, pp. 54–59. DOI: 10.1142/9789812811219_0011. arXiv: hep-ex/0105005 [hep-ex]. URL: http://alice.cern.ch/format/showfull?sysnb=2252790.

[92] Bernard Aubert et al. "Observation of the bottomonium ground state in the decay $\upsilon_{3S} \to \gamma eta_b$". In: *Phys. Rev. Lett.* 101 (2008). [Erratum: Phys. Rev. Lett.102,029901(2009)], p. 071801. DOI: 10.1103/PhysRevLett.101.071801. arXiv: 0807.1086 [hep-ex].

[93] A. J. Bevan et al. "The Physics of the B Factories". In: *Eur. Phys. J.* C74 (2014), p. 3026. DOI: 10.1140/epjc/s10052-014-3026-9. arXiv: 1406.6311 [hep-ex].

[94] Geoffrey C. Fox and Stephen Wolfram. "Observables for the Analysis of Event Shapes in e+ e- Annihilation and Other Processes". In: *Phys. Rev. Lett.* 41 (1978), p. 1581. DOI: 10.1103/PhysRevLett.41.1581.

[95] Geoffrey C. Fox and Stephen Wolfram. "Event Shapes in e+ e- Annihilation". In: *Nucl. Phys.* B149 (1979). [Erratum: Nucl. Phys.B157,543(1979)], p. 413. DOI: 10.1016/0550-3213(79)90120-2,10.1016/0550-3213(79)90003-8.

[96] Geoffrey C. Fox, Tsun-Yan Tse, and Stephen Wolfram. "Event Shapes in Deep Inelastic Lepton - Hadron Scattering". In: *Nucl. Phys.* B165 (1980), pp. 80–92. DOI: 10.1016/0550-3213(80)90307-7.

[97] K. M. Gorski et al. "Power spectrum of primordial inhomogeneity determined from the four year COBE DMR sky maps". In: *Astrophys. J.* 464 (1996), p. L11. DOI: 10.1086/310077. arXiv: astro-ph/9601063 [astro-ph].

[98] Ron Bracewell. "The fourier transform and iis applications". In: *New York* 5 (1965).

[99] J. Alwall et al. "The automated computation of tree-level and next-to-leading order differential cross sections, and their matching to parton shower simulations". In: *JHEP* 07 (2014), p. 079. DOI: 10.1007/JHEP07(2014)079. arXiv: 1405.0301 [hep-ph].

[100] J De Favereau et al. "DELPHES 3, A modular framework for fast simulation of a generic collider experiment". In: *arXiv preprint arXiv:1307.6346* (2013).

[101] Fabian Pedregosa et al. "Scikit-learn: Machine learning in Python". In: *Journal of Machine Learning Research* 12.Oct (2011), pp. 2825–2830.

[102] A. Elagin et al. "A New Mass Reconstruction Technique for Resonances Decaying to di-tau". In: *Nucl. Instrum. Meth.* A654 (2011), pp. 481–489. DOI: 10.1016/j.nima.2011.07.009. arXiv: 1012.4686 [hep-ex].

[103] "Data-Quality Requirements and Event Cleaning for Jets and Missing Transverse Energy Reconstruction with the ATLAS Detector in Proton-Proton Collisions at a Center-of-Mass Energy of $\sqrt{s} = 7$ TeV". In: ().

[104] P. Nason. "A New method for combining NLO QCD with shower Monte Carlo algorithms". In: *JHEP* 11 (2004), p. 040. DOI: 10.1088/1126-6708/2004/11/040. arXiv: hep-ph/0409146 [hep-ph].

[105] S. Frixione, P. Nason and C. Oleari. "Matching NLO QCD computations with parton shower simulations: the POWHEG method". In: *JHEP* 11 (2007), p. 070. DOI: 10.1088/1126-6708/2007/11/070. arXiv: 0709.2092 [hep-ph].

[106] Simone Alioli et al. "A general framework for implementing NLO calculations in shower Monte Carlo programs: the POWHEG BOX". In: *JHEP* 06 (2010), p. 043. DOI: 10.1007/JHEP06(2010)043. arXiv: 1002.2581 [hep-ph].

[107] "ATLAS Run 1 Pythia8 tunes". In: (2014). URL: https://cds.cern.ch/record/1966419.

[108] T. Gleisberg et al. "Event generation with SHERPA 1.1". In: *JHEP* 02 (2009), p. 007. DOI: 10.1088/1126-6708/2009/02/007. arXiv: 0811.4622 [hep-ph].

[109] NNPDF Collaboration. "Parton distributions for the LHC Run II". In: (2014). arXiv: 1410.8849 [hep-ph].

[110] J. M. Butterworth et al. "PDF4LHC recommendations for LHC Run II". In: (2015). arXiv: 1510.03865 [hep-ph].

[111] "Performance of the Reconstruction and Identification of Hadronic tau Decays in ATLAS with 2011 Data". In: ().

[112] ATLAS Collaboration. "Measurement of the mis-identification probability of tau leptons from hadronic jets and from electrons". In: ().

[113] *Pileup in 2012 data*. URL: https://twiki.cern.ch/twiki/bin/view/AtlasPublic/JetEtmissApproved2013Pileup1.

[114] ATLAS Collaboration. "Muon reconstruction efficiency in reprocessed 2010 LHC pp collision data recorded with the ATLAS detector". In: ().

[115] Yu-Ting Shen et al. *Electron isolation efficiency measurement, talk given at Egamma T&P meeting*. URL: {https://indico.cern.ch/event/476937/}{https://indico.cern.ch/event/476937}.

[116] ATLAS EGamma WG. *ATLAS EGamma Twiki*. URL: {https://twiki.cern.ch/twiki/bin/view/AtlasProtected/ElectronEfficiencyRun2}.

[117] "Reconstruction and Calibration of Missing Transverse Energy and Performance in Z and W events in ATLAS Proton-Proton Collisions at $\sqrt{s}$=7 TeV". In: ().

[118] ATLAS Collaboration. "Performance of Missing Transverse Momentum Reconstruction in ATLAS studied in Proton-Proton Collisions recorded in 2012 at 8 TeV". In: *ATLAS-CONF-2013-082* (2013).

[119] ATLAS Collaboration. "Performance of missing transverse momentum reconstruction in proton–proton collisions at 7 TeV with ATLAS". In: *Eur. Phys. J.* C 72 (2012), p. 1844. DOI: 10.1140/epjc/s10052-011-1844-6. arXiv: 1108.5602 [hep-ex].

[120] LHC Higgs Cross Section Working Group et al. "Handbook of LHC Higgs Cross Sections: 1. Inclusive Observables". In: (2011). arXiv: 1101.0593 [hep-ph].

[121] *Procedure for the LHC Higgs boson search combination in summer 2011*. Tech. rep. ATL-PHYS-PUB-2011-011. Geneva: CERN, Aug. 2011. URL: https://cds.cern.ch/record/1375842.

[122] K. A. Olive et al. "Review of Particle Physics". In: *Chin. Phys.* C38 (2014), p. 090001. DOI: 10.1088/1674-1137/38/9/090001.

[123] ATLAS Jet/EtMiss Combined Performance Group. *Jet Energy Resolution Provider*. URL: {https://twiki.cern.ch/twiki/bin/view/Main/JetEnergyResolutionProvider}.

[124] ATLAS Collaboration. "Jet energy resolution in proton-proton collisions at $\sqrt{s} = 7$ TeV recorded in 2010 with the ATLAS detector". In: *Eur. Phys. J.* C 73 (2013), p. 2306. DOI: 10.1140/epjc/s10052-013-2306-0. arXiv: 1210.6210 [hep-ex].

[125] ATLAS Collaboration. "Jet energy measurement and its systematic uncertainty in proton-proton collisions at $\sqrt{s} = 7$ TeV with the ATLAS detector". In: (2014). arXiv: 1406.0076 [hep-ex].

[126] F. Pedregosa et al. "Scikit-learn: Machine Learning in Python". In: *Journal of Machine Learning Research* 12 (2011), pp. 2825–2830.

[127] Yoav Freund and Robert E Schapire. "A desicion-theoretic generalization of on-line learning and an application to boosting". In: *European conference on computational learning theory*. Springer. 1995, pp. 23–37.

[128] F. James and M. Roos. "Minuit: A System for Function Minimization and Analysis of the Parameter Errors and Correlations". In: *Comput. Phys. Commun.* 10 (1975), pp. 343–367. DOI: 10.1016/0010-4655(75)90039-9.

[129] Avital Dery et al. "What if BR(h->mumu)/BR(h->tautau) does not equal m_μ^2/m_τ^2?". In: *JHEP* 05 (2013), p. 039. DOI: 10.1007/JHEP05(2013)039. arXiv: 1302.3229 [hep-ph].

[130] S. Ceci, M. Korolija, and B. Zauner. "Model independent extraction of the pole and Breit-Wigner resonance parameters". In: *Phys. Rev. Lett.* 111 (2013). [Erratum: Phys. Rev. Lett.111, no.15, 159902(2013)], p. 112004. DOI: 10.1103/PhysRevLett.111.112004,10.1103/PhysRevLett.111.159902. arXiv: 1302.3491 [hep-ph].

[131] ATLAS Collaboration. *ATLAS Muon Momentum Resolution in the First Pass Reconstruction of the 2010 pp Collision Data at $\sqrt{s} = 7$ TeV*. ATLAS-CONF-2011-046. 2011. URL: https://cds.cern.ch/record/1338575.

[132] A. Djouadi, J. Kalinowski, and M. Spira. "HDECAY: A Program for Higgs boson decays in the Standard Model and its supersymmetric extension". In: *Comput. Phys. Commun.* 108 (1998), pp. 56–74. DOI: 10.1016/S0010-4655(97)00123-9. arXiv: hep-ph/9704448 [hep-ph].

[133] Daniel de Florian et al. "Transverse-momentum resummation: Higgs boson production at the Tevatron and the LHC". In: *JHEP* 11 (2011), p. 064. DOI: 10.1007/JHEP11(2011)064. arXiv: 1109.2109 [hep-ph].

[134] P. M. Nadolsky et al. "Implications of CTEQ global analysis for collider observables". In: *Phys. Rev. D* D78 (2008), p. 013004. DOI: 10.1103/PhysRevD.78.013004. arXiv: 0802.0007 [hep-ph].

[135] F Bernlochner et al. *Search for a Standard Model Higgs boson in Higgs boson decays to di-muons with the ATLAS detector*. Tech. rep. ATL-COM-PHYS-2014-198. Geneva: CERN, Mar. 2014. URL: https://cds.cern.ch/record/1667860.

[136] T. Binoth et al. "Gluon-induced W-boson pair production at the LHC". In: *JHEP* 12 (2006), p. 046. DOI: 10.1088/1126-6708/2006/12/046. arXiv: hep-ph/0611170 [hep-ph].

[137] T. Binoth, N. Kauer, and P. Mertsch. "Gluon-induced QCD corrections to pp —> ZZ —> l anti-l l-prime anti-l-prime". In: *Proceedings, 16th International Workshop on Deep Inelastic Scattering and Related Subjects (DIS 2008): London, UK, April 7-11, 2008*. 2008, p. 142. DOI: 10.3360/dis.2008.142. arXiv: 0807.0024 [hep-ph]. URL: http://inspirehep.net/record/789541/files/arXiv:0807.0024.pdf.

[138] LHC Higgs Cross Section Working Group. "Higgs pT treatment in gluon-gluon fusion". In: (), URL: {https://twiki.cern.ch/twiki/bin/view/LHCPhysics/GGF#Higgs_pT_treatment}.

[139] D. de Florian et al. "Higgs boson production at the LHC: transverse momentum resummation effects in the $H \to 2\gamma, H \to WW \to \ell\nu\ell\nu$ and $H \to ZZ \to 4\ell$ decay modes". In: *JHEP* 06 (2012), p. 132. DOI: 10.1007/JHEP06(2012)132. arXiv: 1203.6321 [hep-ph].

[140] Massimiliano Grazzini and Hayk Sargsyan. "Heavy-quark mass effects in Higgs boson production at the LHC". In: *JHEP* 09 (2013), p. 129. DOI: 10.1007/JHEP09(2013)129. arXiv: 1306.4581 [hep-ph].

[141] ATLAS Collaboration. *Procedure for the LHC Higgs boson search combination in summer 2011*. ATL-PHYS-PUB-2011-011. 2011. URL: https://cds.cern.ch/record/1375842.